Master's thesis

NTNU
Norwegian University of Science and Technology
Faculty of Engineering
Department of Marine Technology

Jan Ove Kvamen

Mooring Systems For Floating Wind Turbine Farms In Deep Water

Master's thesis in Marine Technology
Supervisor: Erin Bachynski
June 2020

NTNU
Kunnskap for en bedre verden

Jan Ove Kvamen

Mooring Systems For Floating Wind Turbine Farms In Deep Water

Master's thesis in Marine Technology
Supervisor: Erin Bachynski
June 2020

Norwegian University of Science and Technology
Faculty of Engineering
Department of Marine Technology

NTNU
Norwegian University of
Science and Technology

Scope

NTNU Trondheim
Norwegian University of Science and Technology
Department of Marine Technology – Group of Marine Structures

PRE-PROJECT THESIS IN MARINE TECHNOLOGY

FALL 2019

FOR

STUD.TECHN. Jan Ove Kvamen

Mooring systems for floating wind turbine farms in deep water
Forankringssystemer for flytende vindparker på dypt vann

Background:
The offshore wind industry is moving toward deeper water, farther from land, where floating wind turbines (FWTs) become more economical than bottom-fixed turbines. The costs of FWTs still far exceed their bottom-fixed counterparts, and researchers are actively searching for opportunities for cost reduction. In deep water, the mooring system can be particularly expensive, and novel solutions are needed. Different materials, shared moorings, and innovative layouts have potential for cost reductions.

An individual and a park-level mooring system should be designed for the OO Star floater for the California coast. The dynamics of the system in both operational and extreme conditions should be studied.

Assignment:
The following tasks should be addressed in the thesis work:

1. Literature review regarding floating offshore wind turbine concepts, mooring system design, and wind farm wakes.

2. Preliminary design of a mooring system for the OO Star 10 MW floating wind turbine in deep water. Calculation of eigenperiods and mean offsets for different wind speeds.

3. Model reduction: replace the full turbine with a simplified turbine (mass, excitation, and damper). Compare the responses of the simplified and full models in several representative wind and wave conditions.

4. Based on the reduced model, a park-level mooring system should be proposed and a model should be generated in SIMA to study the dynamics of this system in a few operational and extreme conditions.

5. Report and conclude on the investigation.

The work scope could be larger than anticipated. Subject to approval from the supervisor, topics may be deleted from the list above or reduced in extent.

In the project, the candidate shall present his personal contribution to the resolution of problem within the scope of the project work.

Theories and conclusions should be based on mathematical derivations and/or logic reasoning identifying the various steps in the deduction.

The candidate should utilize the existing possibilities for obtaining relevant literature.

The project report should be organized in a rational manner to give a clear exposition of results, assessments, and conclusions. The text should be brief and to the point, with a clear language. Telegraphic language should be avoided.

The project report shall contain the following elements: A text defining the scope, preface, list of contents, main body of the project report, conclusions with recommendations for further work, list of symbols and acronyms, reference and (optional) appendices. All figures, tables and equations shall be numerated.

The supervisor may require that the candidate, in an early stage of the work, present a written plan for the completion of the work. The plan should include a budget for the use of computer and laboratory resources that will be charged to the department. Overruns shall be reported to the supervisor.

The original contribution of the candidate and material taken from other sources shall be clearly defined. Work from other sources shall be properly referenced using an acknowledged referencing system.

Erin Bachynski
Supervisor

Deadline: 06.06.2020

Preface

This thesis is written as a final requirement for obtaining a Master of Science at the *Department of Marine Technology* at the *Norwegian University of Science and Technology (NTNU)*.

The supervisor at NTNU has been Professor Erin Bachynski, and I would like to thank her for sharing her knowledge and the general support she has provided during this project. Additionally, I would like to thank Professor Kjell Larsen for his input regarding mooring system design.

The topic of this project was decided in partnership with the Norwegian energy company *Equinor*, and I would like to thank the company and my external supervisor Gudmund Per Olsen for their insight and general contribution.

Summary

The worldwide energy demand is rapidly increasing. Simultaneously, global warming and increasing temperatures threaten the environment. Therefore, renewable energy sources must be developed. Offshore wind energy is a growing technology and can be part of the solution to this problem. Floating offshore wind turbines can be used to access areas with great potential, as they can operate at large water depths. By optimizing the mooring system, the total cost of a floating offshore wind turbine can be reduced.

Before designing new mooring systems, a literature review was done to acquire information about the behavior of floating offshore wind turbines and their mooring system, in addition to other mooring systems at deep water. The theory regarding wind turbine and anchor design was also studied. Simulations of an existing model called *OO-Star Wind Floater* was performed in *SIMA*. This model was designed at 130 m water depth with the wind turbine *DTU 10 MW Reference Turbine*. The environmental forces in the simulations were based on conditions in an interesting area outside the coast of California.

Due to computational limitations, the results from these simulations were used to make a simplified model of the wind turbine. The rotor blades were substituted with wind coefficients, in addition to other minor adjustments, to reduce the simulation time. The comparison between the initial and the simplified model showed similar results. Therefore, the simplified model was used when testing the designed mooring systems at 700 m water depth. Two mooring systems of a single wind turbine, in addition to a mooring system with a shared mooring line between two turbines, were suggested. These systems were simulated in different operational and extreme conditions, and the results were compared and discussed.

When designing mooring systems of a wind turbine in deep water, long mooring lines are necessary. However, the total cost was estimated to be reduced compared to a chain mooring system at 130 m water depth because polyester was used as the mooring line material. All designed mooring systems passed the test simulated in extreme conditions based on standards from *DNV GL*. The results showed that the horizontal offsets of the wind turbines and the tension in the mooring lines were within their respective restrictions.

The simulation of the system with a shared mooring line resulted in the largest horizontal offsets and mooring line tension. The coupled motion of the system made it challenging to design the dimensions of this shared line. This is one of the recommended improvements if further study of this project is to be performed.

Samandrag

Verdas energibehov aukar stadig, samtidig som global oppvarming og stigande temperaturar truar klima og miljø. Fornybare energikjelder må derfor utviklast. Havvind er ein veksande teknologi som kan bidra til å løyse denne utfordringa. Flytande vindturbinar kan bli brukt til å få tilgang til områder med store energipotensiale, då dei kan operere på djupt vatn. Optimalisering av forankringssystemet kan redusere den totale kostnaden til ein flytande vindturbin.

I forkant av forankringsdesign vart det gjort litteratursøk for å innhente informasjon kring oppførselen til ein flytande vindturbin med tilhøyrande forankringssystem, i tillegg til andre forankringssystem på djupt vatn. Vidare blei bakgrunnsteori for design av vindturbinar og forankring studert. Simuleringar av ein eksisterande modell, kalla *OO-Star Wind Floater*, blei gjennomført i dataprogrammet *SIMA*. Denne modellen var på 130 m havdjup og nytta vindturbinen *DTU 10 MW Reference Trubine*. Naturkreftene i simuleringane var basert på kondisjonar frå eit interessant område utanfor kysten av California.

På grunn av begrensa datakapasitet blei resultata frå desse simuleringane brukt til å lage ein forenkla modell av vindturbinen. Rotorblada blei bytta ut med vindkoeffisientar og andre mindre justeringar blei gjort for å redusere simuleringstida. Då samanlikninga av den opphavlege og den forenkla modellen gav tilsvarande resultat, kunne den forenkla modellen bli brukt når dei nye forankringssystema på 700 m havdjup skulle testast. To forankringssystem til éin vindturbin, i tillegg til eit forankringssystem med ei delt forankringsline mellom to turbinar, blei foreslått. Desse systema blei simulert i ulike operasjonelle og ekstreme kondisjonar og resultata blei samanlikna og diskutert.

Ein av utfordringane ved forankring av vindturbinar på djupt vatn var nødvendigheita av lange ankerliner. Likevel blei den estimerte totale kostnaden av desse systema redusert samanlikna med eit kjettingsystem på 130 m havdjup fordi polyester blei nytta som linemateriale. Samtlege designa forankringssystem bestod testane gjennomført i ekstreme kondisjonar, basert på standardar frå *DNV GL*. Resultata viste at både dei horisontale bevegelsane til vindturbinane, og spenningane i ankerlinene var innanfor sine respektive restriksjonane.

Resultata frå simuleringane av forankringssystemet med ei delt line mellom to turbinar gav dei største utslaga på horisontal bevegelse og linespenning. På grunn av utfordringar med kopla bevegelsar var det vanskeleg å finne gode dimensjonar på den delte lina. Dette er ein av fleire anbefalte forbetringar som bør undersøkast nærmare ved vidare studie av dette prosjektet.

Table of Contents

Nomenclature

Abbreviations

BEM	Blade Element Momentum
EU	European Union
EUR	Euros
$FOWT$	Floating Offshore Wind Turbine
GM	Metacentric Height
MBS	Minimum Breaking Strength
NOK	Norwegian krone

Symbols and Units - Greek

γ_{dyn}	Load factor for dynamic tension
γ_{mean}	Load factor for mean tension
μ	Dynamic viscosity
ν	Kinetic viscosity
ω	Angular velocity
ω_p	Peak frequency
Φ	Velocity potential
ρ	Density

Symbols and Units - Latin

A	Area
C	Damping
C_{wind}	Quadratic wind coefficient
D	Drag

E	Energy
F	Force
f	Frequency
g	Gravitational acceleration
H_s	Significant wave height
k_E	Elastic stiffness
k_G	Geometric stiffness
L	Lift
l	Length
M	Moment
m	Mass
P	Power
p	Pressure
S_C	Characteristic capacity
T	Tension
t	Time
T_d	Design tension
T_p	Wave period
U_{10}	Mean wind speed 10 m above mean water level
U_{mean}	Mean wind speed
V	Velocity
x	Displacement
z	Height

List of figures

List of tables

1 Introduction

1.1 Background

Offshore wind is a rapidly growing market and a part of the solution to the increasing energy demand the word is facing. Renewable energy is expanding, and offshore wind is an established energy resource. In Europe, 502 new offshore wind turbines were connected to the grid across ten wind farms in 2019. This brought 3623 MW of net additional capacity to the total installed offshore wind capacity of 22 072 MW, divided by 5047 wind turbines (Europe, 2020). This development is predicted to continue, and the *International Renewable Energy Agency (IRENA)* has predicted that by the year of 2045, the operating capacity can reach 400 GW, as can be seen in Figure 1.

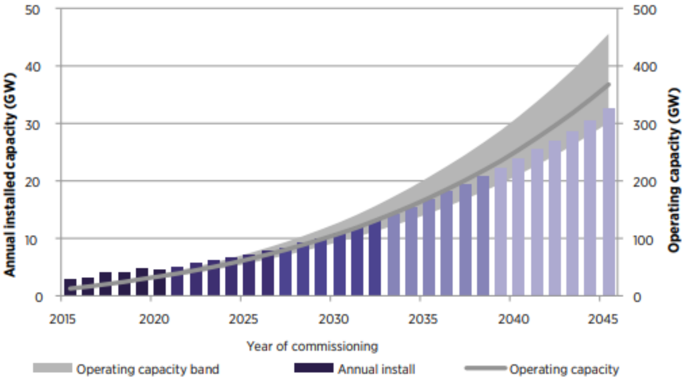

Figure 1: Annual installed and operating capacity of offshore wind globally, 2016-2045 (IRENA, 2016).

The average rated capacity of the wind turbines installed in 2019 was 1 MW larger than in 2018 and equal to 7.8 MW. The average distance to shore and water depth were 59 km and 33 m, respectively, compared to 33 km and 27.1 m in 2018 (Europe, 2020). The development of the rated capacity, distance to shore and water depth of yearly installed wind turbines over the latest decades can be seen in figures 2, 3, and 4, respectively.

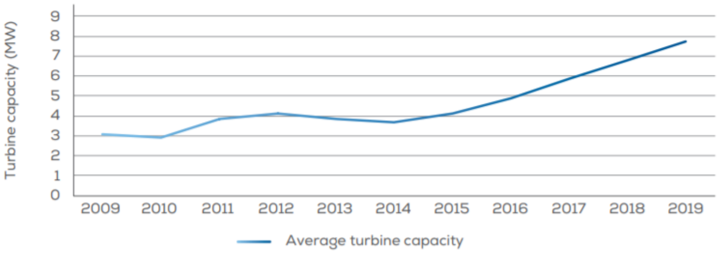

Figure 2: Average size of commercial offshore wind farm projects completed each year (MW) (Europe, 2020).

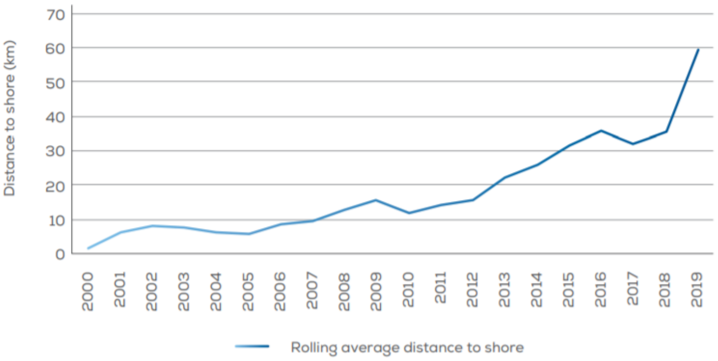

Figure 3: Rolling average water depth of online offshore wind farms (Europe, 2020).

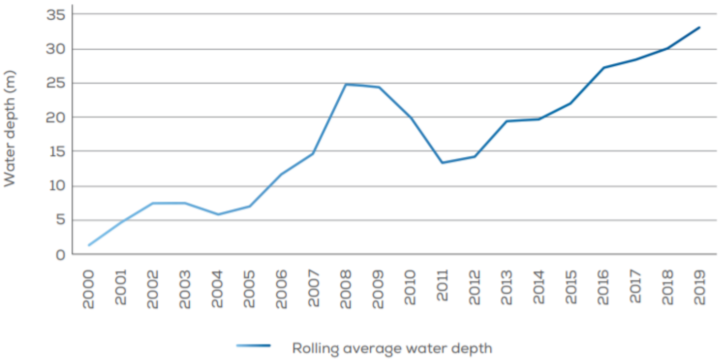

Figure 4: Rolling average distance to shore of online offshore wind farms (Europe, 2020).

The distribution of substructure types for offshore wind turbines can be seen in Figure 5, and clearly shows that bottom fixed concepts are leading. However, as the figures above indicates, offshore wind turbines are moving further offshore, towards deeper water, and floating concepts will likely be more attractive in the future. Floating wind turbines are convenient at water depth larger than 60 m, as bottom fixed ones become too expensive (IRENA, 2016).

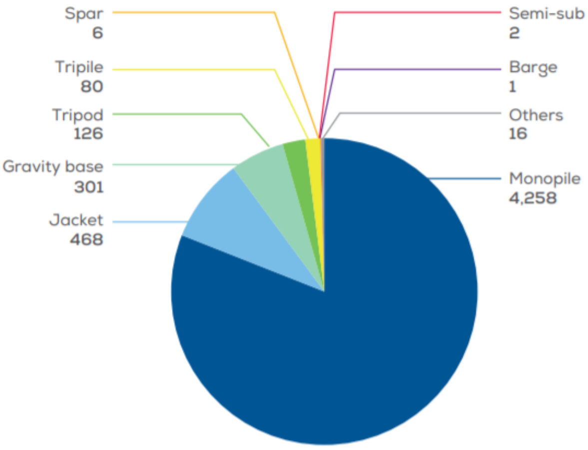

Figure 5: Share of substructure types for grid-connected wind turbines at the end of 2019 (Europe, 2020).

One of many companies with increasing interest within offshore wind is the Norwegian energy company *Equinor*, and this project is performed in collaboration with them. *Equinor* is the largest operator in Norway and specializes in the fields of oil, gas, wind, and solar energy. They have developed an offshore wind technology named *Hywind*, and currently, one floating offshore wind farm has been realized, titled *Hywind Scotland*. Another floating offshore wind project under development by the company is named *Hywind Tampen*. These projects are explained below according to details from the company web page (Equinor, 2020).

1.1.1 Hywind Scotland

Hywind Scotland was the world's first floating offshore wind farm, and located 25 km east of Peterhead in Scotland. There are five floating wind turbines with a combined capacity of 30 MW and an average capacity factor of 56%. The wind turbines are placed on monopile substructures at water depth ranging between 95 m-120 m, and the wind turbines have a total height of 253 m.

1.1.2 Hywind Tampen

Hywind Tampen is an ongoing project which will be completed in 2022, as the first floating offshore wind farm on the Norwegian shelf. The wind farm will be located 140 km from shore, between the oil platforms *Snorre* and *Gullfaks* at water depths from 260 m to 300 m. Eleven wind turbines will be installed with a total capacity of 88 MW, enough to cover approximately 35% of the platforms' yearly power demand.

1.2 Research Motivation

The worldwide energy demand is rapidly increasing, simultaneously, global warming and the increasing temperature is a great challenge the world is facing. Therefore, green renewable energy sources must be developed. As a consequence, the EU has agreed to a 32% renewable energy target by 2030 (Europe, 2020). Offshore wind energy is one of the most promising and reliable established renewable energy sources. However, as a relatively new technology, the overall performance could be improved and the total cost could be reduced to increase future interest and value.

As floating wind turbines move towards deeper water, further offshore, while also increasing in size and number, the mooring system becomes more critical. Shared mooring of floating wind turbines could reduce the total length of the mooring lines, as well as the number of mooring lines and anchors, resulting in a lower installation cost.

1.2.1 Floating offshore wind park at the coast of California

Equinor have explored the possibility of installing an offshore wind farm off the coast of California, where the environmental conditions are looking promising. The wind conditions have been praised as among the best in the world. Some exciting environmental values, including wind speeds and wave conditions, have been summarised in the article Musial et al. (2016). The conclusion was that there is a technical resource potential of 112 GW over the entire California coastline. Additionally, 96% of the offshore wind resources are in waters deeper than 60 m. This indicates that floating wind technology will most likely be the realistic option off the coast of California and most of the Pacific Coast.

1.3 Objective and Approach

This project's objectives were to study floating offshore wind turbines and mooring systems related to offshore installations. Furthermore, mooring systems of floating wind turbines in deep water were going to be designed. Additionally, the project should provide competence in the computer software *SIMA*, through simulations of wind turbines exposed to reasonable external loads defined based on environmental data from the area of interest. Two key questions defined this project:

1: What are the challenges and possible solutions for mooring a single turbine in deep water?

2: How does a shared mooring line change the behavior of the wind turbines?

The approach to achieve the objectives, and try to answer the questions above, was to initially do a literature study concerning offshore wind turbines and mooring systems, as well as studying theory to gain comprehension within this field. The restrictions and criteria when designing a mooring system were also studied. After that, the relevant area was studied by examining measurement data from a weather station located off the coast of California. Dominating wind speeds, as well as significant wave heights and wave periods, were inspected and created the basis for deciding the input parameters in the simulations. Simulations of an existing *SIMA*-model were performed to highlight the behavior of different turbine characteristics. Based on the obtained results, modifications and simplifications of the initial model were performed, and mooring systems of both a single wind turbine and a park-level system at 700 m water depth were designed. The mooring systems were simulated in extreme conditions according to design rules, and the results were studied according to different restrictions and criteria. Decay tests were simulated to discover natural periods, and turbulent wind tests were performed to study wind turbines' behavior in different operational conditions. The effects on the wind turbines, the platforms, and the mooring lines were analyzed and created the basis for the discussion and conclusion of this project.

1.4 Literature review

Through his role in *Equinor*, which have been a partner in this project, Professor Kjell Larsen has provided detailed mooring system information of the floating wind farms *Hywind Scotland* and *Hywind Tampen*, as well as the deep water gas platform *Aasta Hansteen*.

The floating offshore wind farm *Hywind Scotland* has wind turbines connected to three chain mooring lines. The mooring line length is 609.2 m, including a 50 m bridle at the turbine end. The pre-tension in the mooring lines is 900 kN, and the diameter of the chain is 132 mm in the bridle-part and 147 mm in the remaining mooring line. The mooring system can be seen in Figure 6.

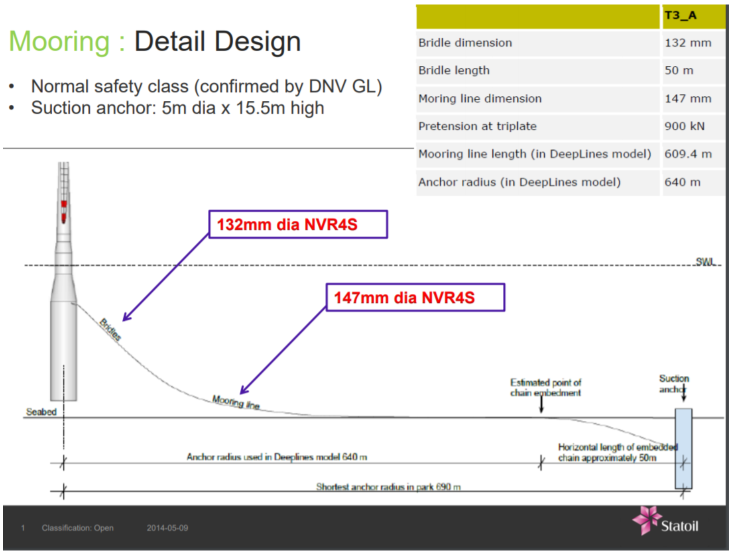

Mooring : Detail Design

- Normal safety class (confirmed by DNV GL)
- Suction anchor: 5m dia x 15.5m high

	T3_A
Bridle dimension	132 mm
Bridle length	50 m
Moring line dimension	147 mm
Pretension at triplate	900 kN
Mooring line length (in DeepLines model)	609.4 m
Anchor radius (in DeepLines model)	640 m

1 Classification: Open 2014-05-09

Statoil

Figure 6: Mooring system of *Hywind Scotland* (Larsen, 2020).

A proposed mooring system of the future floating wind farm *Hywind Tampen*, seen in Figure 7, was also handed out by Professor Kjell Larsen. This example shows mooring lines with a combination of chain and polyester connected to a shared suction anchor approximately 1000 m from the wind turbines.

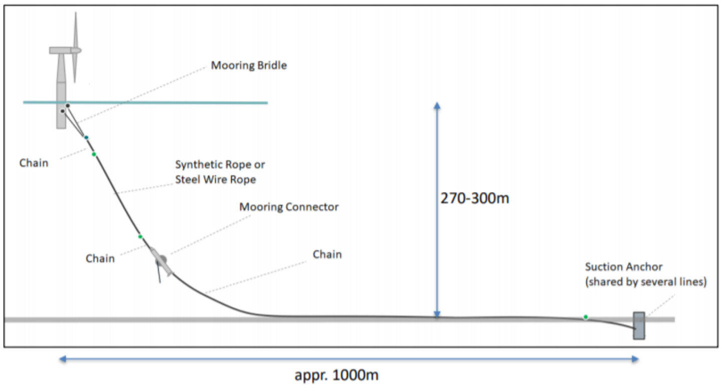

Figure 7: Proposed mooring system of *Hywind Tampen* (Larsen, 2020).

A construction that has already been completed with deep water mooring is the gas platform *Aasta Hansteen*. The platform is located at a water depth of 1300 m, and its mooring system can be seen in Figure 8. The seventeen mooring lines are made of polyester and chain with diameter 254 mm and 160 mm, respectively. The length of the segments is 120 m chain, followed by 2400 m of polyester, and finally 135 m of chain, resulting in a total mooring line length of 2655 m.

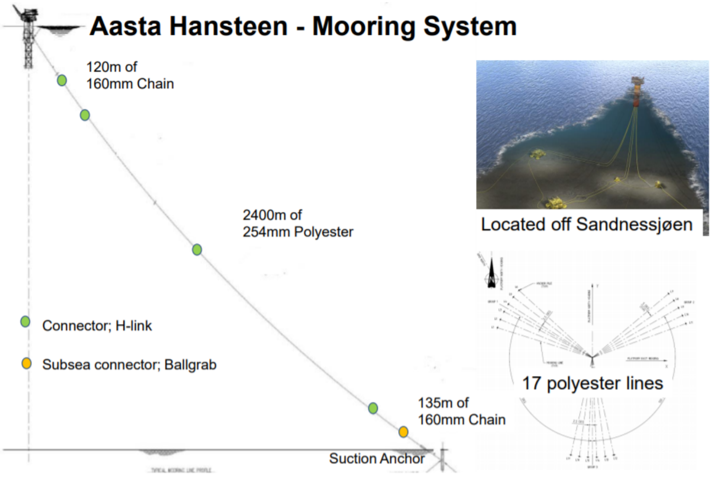

Figure 8: Mooring system of *Aasta Hansteen* (Larsen, 2020).

Two highly relevant articles concerning shared mooring of a floating wind turbine farm were studied. The articles are written by Matthew Hall and Patrick Connolly from the University of Prince Edward Island in Charlottetown in Canada.

The first article is called *Coupled Dynamics Modelling Of A Floating Wind Farm With Shared Mooring Lines* (Hall and Connolly, 2018). The article demonstrates a square-shaped, shared-mooring, floating wind farm with four wind turbines and concludes that: "*Results show reasonable behaviour of the platform motions, with surge displacements under wind and wave loading that reflect the complex restoring properties of a shared mooring arrangement. Varying phase relationships in the platforms' motions arising from their spatial offsets in the sea state show that shared mooring lines will see different excitation at each end. Fluctuations in the mooring line tensions bear out this fact, and also show the importance of line dynamics in these shared mooring arrangements. In particular, the shared mooring lines show a greater tendency for resonance due to the absence of seabed contact*".

In the other article, *Comparison of pilot-scale floating offshore wind farms* *with shared moorings* (Connolly and Hall, 2019), several shared mooring farm arrangements for floating offshore wind turbines were proposed and investigated. As part of the conclusion it was stated that: "*The results show that by choosing appropriate mooring line properties, platform displacements and mooring line tensions can be kept low, and significant cost savings over individually-moored farms are possible at water depths exceeding 400 m*".

Previous master's students at *NTNU* have studied similar objectives as the ones considered in this project. A thesis from 2019 proposed mooring systems of a spar substructure wind farm at 600 m water depth in the Norwegian North Sea (Chan Chow, 2019). This thesis proposed a simplified *SIMA*-model of the *DTU* 10 MW *Reference Wind Turbine* with results showing: *"The simplified model produced higher average surge offsets than the full model, but no more than 5% difference for the operational load cases"*. Shared anchor mooring arrangements were proposed and compared to dimensions of the Hywind Scotland mooring system.

2 Theory

This theory section will describe some of the main forces and responses on a floating offshore wind turbine. Some spectra for stochastic wind and waves will be presented, followed by a multiple degree of freedom system to demonstrate coupled motion. Mooring line systems and mooring line material will be described, before design regulations and criteria for a mooring system of a floating offshore wind turbine will complete this section.

2.1 Wind turbine forces and responses

A floating offshore wind turbine is a complex system exposed to many different loads. The main excitation forces are aerodynamic, hydrodynamic, and structural dynamic forces. These forces and their responses on a floating offshore wind tribune will be described in the following sections.

2.1.1 Aerodynamics

The following theory of aerodynamics will follow the derivations and explanations in Hansen (2015).

Wind turbines are exposed to a force, called the thrust force, from the approaching wind. To determine this thrust force, one-dimensional momentum theory and an ideal rotor were used, and the following assumptions were made:

- Homogeneous, incompressible, steady-state fluid flow.
- No frictional drag.
- No flow through stream tube boundary.
- Infinite blades, uniform thrust over the disk.
- Non-rotating wake.
- Pressure equal to ambient pressure far from disk.

These assumptions lead to streamlines of the wind shown in Figure 9, with the corresponding velocity and pressure distribution.

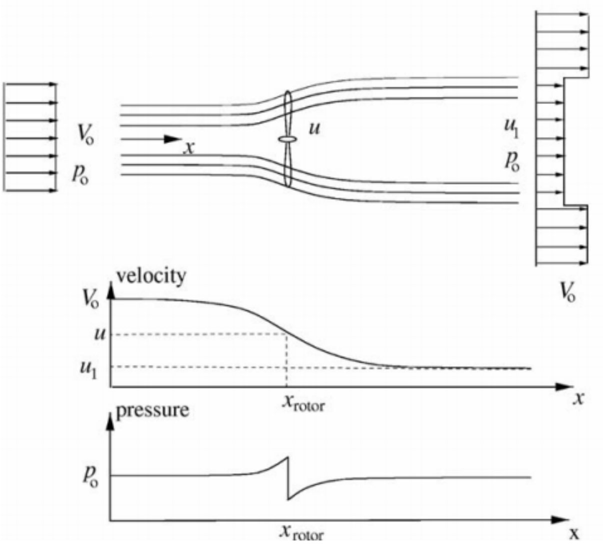

Figure 9: Streamlines past rotor, velocity and pressure up- and downstream of the rotor (Hansen, 2015)

The lower pressure at the far side of the rotor results in a thrust force, T, on the wind. This force slows down the wind speed in order to extract kinetic energy. The thrust force and the pressure drop are calculated from Bernoulli equation, and result in Equations 1 and 2.

$$T = \Delta p A_D. \tag{1}$$

$$\Delta p = \frac{1}{2}\rho(V_0^2 - u_1^2). \tag{2}$$

The velocities, shown in Figure 10, and the loads, presented in Figure 11, on an airfoil can be studied by using two-dimensional aerodynamics.

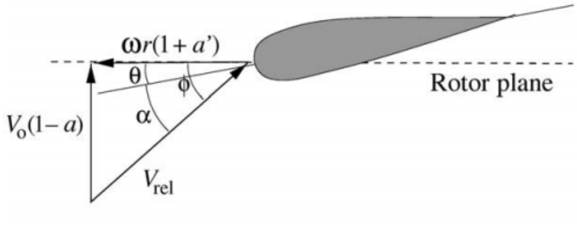

Figure 10: Velocities at the rotor plane (Hansen, 2015).

V_0 is the velocity of the incoming wind and ω is rotor speed, giving a velocity ωr

at the radius r. a is called the the axial induction factor and gives the ratio of wind velocity reduction, calculated from Equation 3.

$$a = \frac{V_0 - u_1}{V_0}, \tag{3}$$

where u_1 is the wind speed at the far side of the rotor shown in Figure 9.

a' is the rotational induction factor calculated from Equation 4.

$$a' = \frac{1 - 3a}{4a - 1}. \tag{4}$$

The relative velocity, V_{rel}, is the velocity the blades experience. The angle between the relative velocity and the rotor plane is called the flow angle and is denoted ϕ. This angle can be divided into two smaller angles, α, and θ. α is the angle between the relative velocity and the chord line, and θ is the angle between the chord line and the rotor plane. The chord line is the straight line from the trailing to the leading edge of the airfoil.

The loads created on an airfoil are the drag and lift force. The drag force, D, is due to viscous forces and pressure difference and acts parallel to the relative velocity. The viscous forces slow down the flow in the boundary layer. The lift force, L, is due to pressure difference from the unequal velocity around the airfoil and acts perpendicular to the relative velocity. The total force, R, can be decomposed to a normal force, p_N, and a tangential force, p_T. p_N contributes to the thrust force on the rotor, and p_T is the component that drives the blade around in the rotor plane. These forces can be calculated by Equation 5 and 6.

$$p_N = L\cos\phi + D\sin\phi. \tag{5}$$

$$p_T = L\sin\phi - D\cos\phi. \tag{6}$$

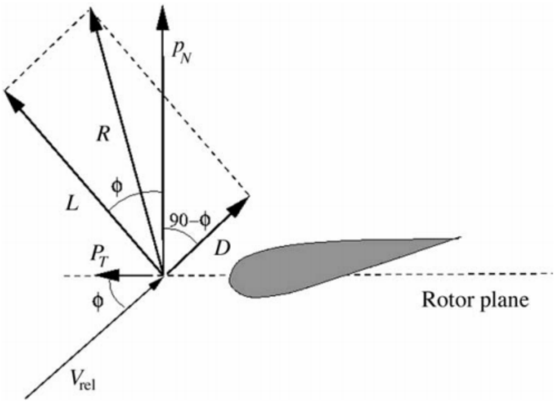

Figure 11: Loads at the rotor plane (Hansen, 2015).

Lift and drag coefficients, C_l and C_d are defined in Equation 7.

$$C_l = \frac{L}{\frac{1}{2}\rho V_\alpha^2 c} \quad \text{and} \quad C_d = \frac{D}{\frac{1}{2}\rho V_\alpha^2 c}, \tag{7}$$

where V_α is the wind velocity, ρ is the air density, c is the length of the aerofoil, and L and D are the lift and drag force, respectively.

Blade element momentum method

The blade element momentum (BEM) method is a way of calculating the steady loads and thrust force of a wind turbine with different pitch angles and rotational speed, exposed to different wind speeds. For this method to be valid, the following assumptions must be made (Hansen, 2015):

- No radial dependency – what happens at one element cannot be felt by the others.
- The force from the blades on the flow is constant in each annular element; this corresponds to a rotor with an infinite number of blades.

Generally the BEM method can be summarized in the 8 following steps:

Step 1: Initialize a and a', typically $a = a' = 0$

Step 2: Compute the flow angle, ϕ, using Equation 8.

$$\phi = \arctan\left(\frac{(1-a)V_0}{(1+a)\omega r}\right). \tag{8}$$

Step 3: Compute the local angle of attack, α, using Equation 9 where θ is the local pitch of the blade.

$$\alpha = \phi - \theta. \tag{9}$$

Step 4: Find $C_l(\alpha)$ and $C_d(\alpha)$ from table.

Step 5: Compute C_n and C_t from Equation 10.

$$C_n = C_l cos\phi + C_d sin\phi \quad \text{and} \quad C_t = C_l sin\phi + C_d cos\phi. \tag{10}$$

Step 6: Calculate a and a' from Equation 11.

$$a = \frac{1}{\frac{4sin^2\phi}{\sigma C_n} - 1} \quad \text{and} \quad a' = \frac{1}{\frac{4sin\phi cos\phi}{\sigma C_l} - 1}, \tag{11}$$

where σ is the solidity defined as the fraction of the annular area in the control volume which is covered by blades found from Equation 12.

$$\sigma(r) = \frac{c(r)B}{2\pi r}, \tag{12}$$

where B is the number of blades, $c(r)$ is the local chord and r is the radial position of the control volume.

Step 7: If a and a' have changed more than a certain tolerance go back to Step 2, else finish.

Step 8: Compute the local loads on the segment of the blades.

Prandtl's tip loss factor, F, is introduced to correct the assumption of an infinite number of blades and Glauert correction is used when a becomes large, and simple momentum theory breaks down since the wind velocity in the far wake would be negative. Dynamic correction factors like dynamic wake effect and dynamic stall could also be introduced.

Wake deficit

The wind field behind a wind turbine gets disturbed due to the aerodynamics on the blades. A wind turbine located behind another will be exposed to this disturbed wind and experience a different wind speed. This is called a wake deficit and is described in Jensen (1983). Equation 13 is presented as a method to calculate the wind speed experienced by the rear turbine, u_1. This is a simplification that assumes a linear wake and that the velocity behind the first rotor is $\frac{1}{3}V_0$ in accordance with classical theory.

$$u_1 = V_0 \left(1 - \frac{2}{3} \left(\frac{r_0}{r_0 + \alpha x} \right)^2 \right). \tag{13}$$

V_0 is the initial wind speed in front of the first turbine, r_0 is the rotor diameter, α is called the entrainment constant equal to 0.1 for usual wakes (Jensen, 1983), and x is the distance between the turbines, presented in Figure 12.

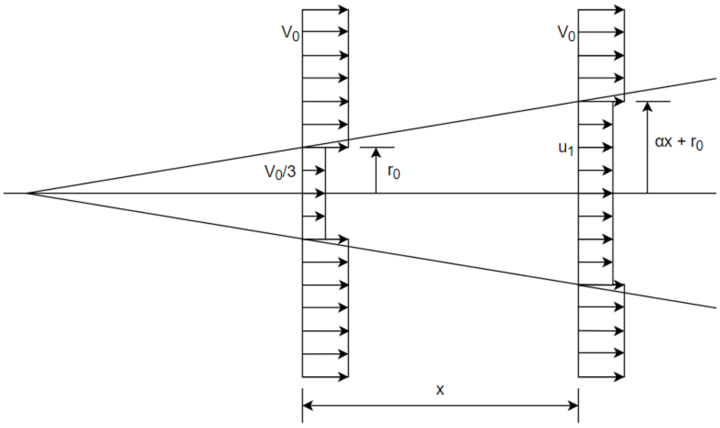

Figure 12: The Jensen wake model (Jensen, 1983).

2.1.2 Hydrodynamics

When studying a large volume structure exposed to waves from a hydrodynamic perspective, it is efficient to use linear potential flow theory. This can be used to solve a wave-structure interaction problem. However, this theory has some underlying simplifications that must be taken into consideration (Cruz and Atcheson, 2016).

- The free-surface and the body boundary conditions are linearised.
- Viscous effects like shear stresses and flow separation are not considered.
- The fluid is incompressible and the flow is irrotational, which leads to Equation 14 known as the Laplace equation.

  $$\nabla^2 \Phi = 0, \tag{14}$$

  where Φ is the velocity potential.
- The bottom is assumed to be flat and uniform.

- Under these assumptions all variables can be expressed as a complex amplitude times $e^{i\omega t}$.

These simplifications lead to Equation 15, which describes the velocity potential at any point of a wave in the fluid domain.

$$\Phi = Re(\phi e^{i\omega t}), \tag{15}$$

where ϕ is the complex velocity potential, Re denotes the real part, ω is the angular frequency of the incident wave, and t is the time.

Some boundary conditions will also be introduced, explained by Figure 13 from (Pettersen, 2007).

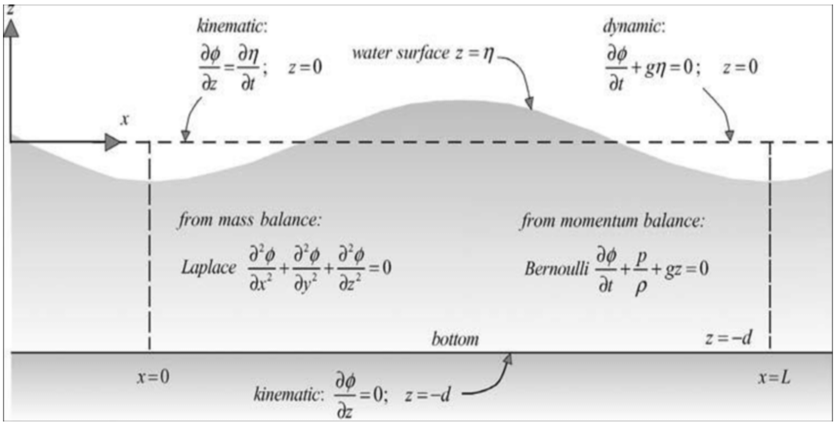

Figure 13: Boundary conditions of wave-structure interaction problem with linear potential flow theory (Pettersen, 2007).

A hydrodynamic interaction problem in regular waves is generally dealt with as two sub-problems, where A is called the diffraction problem, and B is referred to as the radiation problem (Faltinsen, 1998).

A: The forces and moments on the body when the structure is restrained from oscillating and there are incident regular waves. The hydrodynamic loads are called *wave excitation loads* and composed of so called Froude-Kriloff and diffraction forces and moments.

B: The forces and moments on the body when the structure is forced to oscillate with the wave excitation frequency in any rigid-body mode. There are no incident waves. The hydrodynamic loads are identified as *added mass*, *damping* and *restoring* terms.

Added mass and damping can be described as steady-state hydrodynamic forces and moments due to forced harmonic rigid body motions (sub-problem B). These forces and moments can be calculated by defining force components in the x-, y-, and z-direction as F_1, F_2 and F_3, respectively. The moment components along the same axis can be defined as F_4, F_5, F_6. Added mass and damping loads due to harmonic motion mode, η_j, can be written as Equation 16.

$$F_k = -A_{kj}\frac{d^2\eta_j}{dt^2} - B_{kj}\frac{d\eta_j}{dt}. \tag{16}$$

The restoring forces of a freely floating structure can be found from hydrostatic and mass considerations. The force and moment components can be written as Equation 17.

$$F_k = -C_{kj}\eta_j. \tag{17}$$

C is the restoring coefficient found from Equation 18.

$$\begin{aligned}
C_{33} =& \rho g A_{WP}, \\
C_{35} =& C_{53} = \iint_{A_{WP}} x ds, \\
C_{44} =& \rho g V \overline{GM}_T, \\
C_{55} =& \rho g V \overline{GM}_L,
\end{aligned} \tag{18}$$

where A_{WP} is the waterplane area, V is the displaced volume, $\overline{GM}_T$, and $\overline{GM}_L$ are the transverse and longitudinal metacentric height, respectively.

Wave loads on structures

Morison's Equation is used to calculate wave loads on fixed, slender offshore structures with circular cross-sections. The total force, F, is divided into two components, mass force, F_M, and drag force, F_D, as seen in Equation 19.

$$dF = dF_M + dF_D = \rho\frac{\pi D^2}{4}C_M a_x dz + \frac{1}{2}\rho C_D D u|u| dz, \tag{19}$$

where ρ is the water density and D is the diameter of the structure. C_M and C_D denotes the mass and drag coefficient, and a_x and u are the acceleration and the velocity of the water particles, respectively.

The hydrodynamic coefficients will be functions of Reynolds number, Re, Keulegan-Carpenter number, KC, and surface roughness. The Reynolds number and the Keulegan-Carpenter number can be calculated by Equation 20 and 21, respectively.

$$Re = \frac{\rho U D}{\mu} = \frac{U D}{\nu}. \tag{20}$$

$$KC = \frac{U T}{D}. \tag{21}$$

U represents the fluid velocity, D is the diameter of the structure, μ and ν are the dynamic and kinematic viscosity of the fluid, and T is the wave period.

Response of floating structures

The equation of motion can be used to calculate the response of a floating structure due to the wave loads. The equation of motion for an uncoupled one degree of freedom system can be calculated from Newton's second law and results in Equation 22.

$$(M + A)\ddot{x} + C\dot{x} + Kx = F(t). \tag{22}$$

M is the mass of the structure, A is the added mass, C is the damping coefficient, K is the restoring coefficient, and $F(t)$ is the excitation force. x, $\dot{x}$ and $\ddot{x}$ are the displacement, velocity, and acceleration of the structure, respectively.

The hydrodynamic excitation force is found from the diffraction problem, sub-problem A. In contrast, the added mass, the damping coefficient, and the restoring coefficient are found from sub-problem B described above.

2.1.3 Structural dynamics

The following section contains theory of different methods to calculate the dynamic behavior of a structure and follows derivations from Cruz and Atcheson (2016).

Linear rigid body dynamics

The dynamic structural model can be simplified and represented as a single rigid body. The motion of the structure can be represented as global motions in six degrees of freedom about a given inertia reference point, as can be seen in Figure 14. Together, these six motions represent the displacement x in Equation 22, presented in the section above, and the velocity and acceleration can be calculated. The forces on the entire body will be environmental forces from both waves, wind, and current. Due to the complexity of a wind turbine, the loads are considered in the time domain.

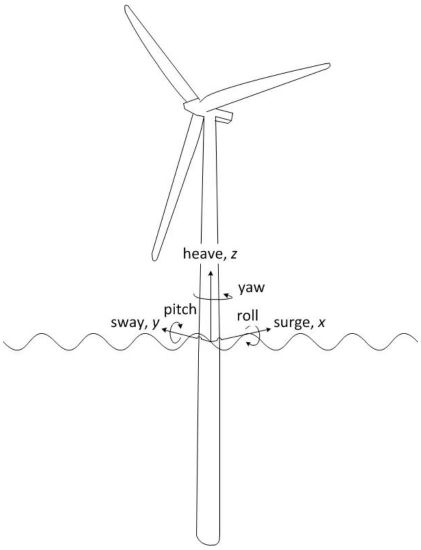

Figure 14: Axial system to describe motions of a floating structure.

Finite element methods

Finite element methods discretize the model into finite elements. The sum of the smaller elements represents the properties of the entire structure. The static and dynamic structural responses are the sum of the mass, damping, and stiffness in all degrees of freedom of the individual elements. The methods use shape functions to provides an approximation of quantities like stress and strain. Different element types such as beam and shell elements can be used, and the governing equation can be written as Equation 23 regardless of the element type, assuming element mass and damping matrices following from the discretisation and use the same shape function as the stiffness matrix.

$$M_g\ddot{\vec{D}} + C_g\dot{\vec{D}} + \vec{R}^{int} = \vec{R}^{ext}. \tag{23}$$

M_g is the mass and added mass and C_g is the damping of the structure, while R^{int} and R^{ext} are the internally and externally applied loads. $\dot{\vec{D}}$ and $\ddot{\vec{D}}$ are the velocity and acceleration vectors of the system.

For linear elastic materials, the internal forces can be written as Equation 24.

$$\vec{R}^{int} = K_g\vec{D}, \tag{24}$$

where K_g is the stiffness of the element and $\vec{D}$ is the system displacement vector.

Different types of nonlinearities can occur in practice. Therefore, the stiffness matrix will be a function of $\vec{D}$, and Equation 23 will be a system of time-continuous, second-order coupled differential equations.

Classical beam theory, or Euler-Bernoulli theory, is one example of a element type. This element provides the bending deformations of a long, slender beam due to transverse deformations when exposed to a load. Euler-Bernoulli is a particular case of the Timoshenko beam theory. Timoshenko beam elements are beneficial to use if the beam is thicker, as this theory also accounts for shear deformations.

2.2 Stochastic wind and waves

Wind and waves are stochastic in nature. Therefore, some stochastic theory was studied before running simulations of these environmental loads. This section will follow the derivations of Naess and Moan (2013).

Physical phenomena typically result in different behaviors from separate recordings under statistically identical conditions and are often characterized by irregularities. A stochastic process is mathematically defined as: *"The quantity X(t) is called a stochastic process if X(t) is a random variable for each value of t in an interval (a, b)"* (Naess and Moan, 2013).

2.2.1 Standardized spectra

Even though wave and wind processes are stochastic, it can be assumed that their long term evolution can be considered as, e.g., 3 hour stationary sequences for modeling purposes. Stationary implies that the statistical properties do not change with time, resulting in equal mean value and standard deviation for all points in time (Naess and Moan, 2013).

Wave spectra

When statistically modeling waves, it can be assumed that the wave field is stationary in time and homogeneous in space, for limited periods of time. The wave condition is, for specific intervals, assumed to be in steady-state. Some wave spectra are functions of a value called the significant wave height, H_s. The significant wave height is defined as the mean of the one third highest waves. Another important parameter when studying the waves from a statistical point of view is the wave period, T_p. The wave period is defined as the distance, measured in seconds, between two waves passing through a stationary point (Faltinsen, 1998).

A wave spectrum, $S^+(\omega)$, represents the wave energy of different frequencies, ω. One example of a wave spectrum type characterizing fully developed sea states is the *Pierson-Moskowitz* type, with its basic form presented in Equation 25.

$$S^+(\omega) = \frac{A}{\omega^5} \exp\left(-\frac{B}{\omega^4}\right), \tag{25}$$

where A and B are given by other parameters presented below.

- *Pierson-Moskowitz spectrum*: $A = \alpha g^2$, where $\alpha = 0.0081$, and $B = 1.25\omega_p^4$, where ω_p is the peak frequency at which $S(\omega)$ has a maximum.
- *Modified Pierson-Moskowitz spectrum*: $A = \frac{5}{16} H_s^2 \omega_p^4$, where H_s is the significant wave height, and $B = 1.25\omega_p^4$.
- *ISSC spectrum*: $A = 0.1107 H_s \bar{\omega}^4$ and $B = 0.4427\bar{\omega}^4$, where $\bar{\omega}$ is the average wave frequency.

Another spectrum type called the *JONSWAP spectrum* is a modification of the *Pierson-Moskowitz* type, and has the form presented in Equation 26.

$$S^+(\omega) = \frac{\tilde{\alpha} g^2}{\omega^5} \exp\left(-1.25\frac{\omega_P^4}{\omega^4}\right) \cdot \gamma^{a(\omega)}, \tag{26}$$

where γ is the peakedness parameter with the exponent $a(\omega)$ presented below, and $\tilde{\alpha}$ is related to a fetch parameter and the mean wind speed.

$$a(\omega) = \exp\left(-\frac{(\omega - \omega_p)^2}{2\tilde{\sigma}^2 \omega_p^2}\right), \tag{27}$$

and

$$\tilde{\sigma} = \begin{cases} \tilde{\sigma}_a = 0.07, & \text{for} \quad \omega \leq \omega_p \\ \tilde{\sigma}_b = 0.09, & \text{for} \quad \omega > \omega_p \end{cases} \tag{28}$$

For $\gamma = 1$, the JONSWAP spectrum reduces to the modified Pierson-Moskowitz spectrum as shown in Figure 15.

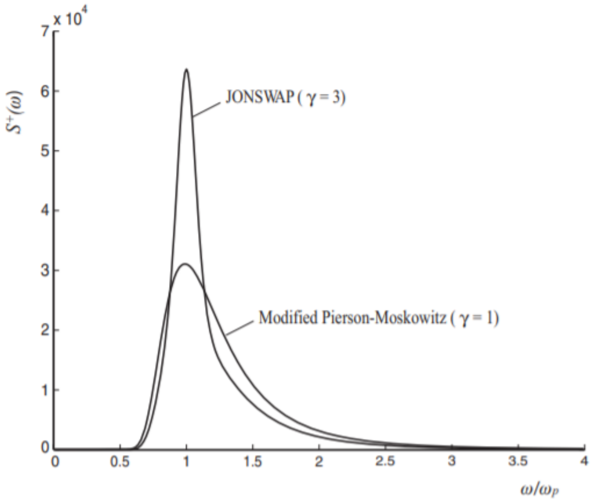

Figure 15: Plots of JONSWAP spectra with $\gamma = 1$ and 3.

Wind spectra

Turbulent wind can have a nearly constant average value over long periods of an hour or more, but it can be quite variable over shorter times. The turbulence is a result of wind gusts. Additionally, the wind may have slowly-varying, also called quasi-static, changes of the mean wind speed, resulting in relatively small frequencies.

A wind spectra is expressed as $\omega S_U^+(\omega)$ with respect to the standardized reference mean value at height 10 m, $\bar{U}_{10}$, and the most cited ones are (Naess and Moan, 2013):

- *Davenport spectrum*:
$$\frac{\omega S_U^+(\omega)}{\delta \bar{U}_{10}^2} = \frac{4\theta^2}{(1+\theta^2)^{4/3}}. \tag{29}$$
- *Harris spectrum*:
$$\frac{\omega S_U^+(\omega)}{\delta \bar{U}_{10}^2} = \frac{4\theta}{(2+\theta^2)^{5/6}}. \tag{30}$$
- *Kaimal spectrum*:
$$\frac{\omega S_U^+(\omega)}{\sigma_U^2} = \frac{6.8\theta}{(1+10.2\theta)^{5/3}}. \tag{31}$$

- *The American Petroleum Institute (API)*:

$$\frac{\omega S_U^+(\omega)}{\sigma_U(z)^2} = \frac{\omega/\omega_p}{(1+1.5\omega/\omega_p)^{5/3}}. \tag{32}$$

The dimensionless parameter, θ, is found from Equation 33, δ is the surface drag coefficient assumed equal to 0.001 for offshore locations, and σ_U is the variance of U(t) at $\bar{U}_{10}$ (Naess and Moan, 2013).

$$\theta = \frac{\omega L_u}{2\pi\bar{U}_{10}} = \frac{fL_u}{\bar{U}_{10}}, \quad 0 < \theta < \infty, \tag{33}$$

where L_u is an integral length scale equal to 1200 m in the Davenport spectrum, and 1800 m in the Harris spectrum.

A graphic presentation of the different wind spectra can be seen in Figure 16. The Kaimal spectrum, mostly used when studying wind turbines, is copied from Van der Male and Lourens (2015).

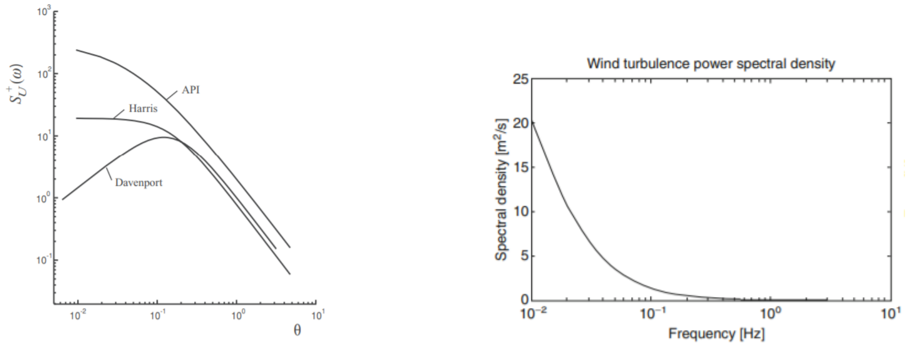

(a) Plots of wind spectra. $\theta = \omega L_u/2\pi\bar{U}_{10}$ for the Davenport and Harris spectra, $\theta = \omega/\omega_p$ for the API spectrum (Naess and Moan, 2013).

(b) Kaimal spectrum (Van der Male and Lourens, 2015).

Figure 16: Wind spectrum.

2.2.2 Short term statistics

The probability distribution of an event is often denoted as its short term distribution. This covers the probability of a single event to happen in a constant environmental state. Short term design considers the load effects established during a 100-year storm with a specified duration of 3 or 6 hours. This is used as the basis for dimensioning an offshore construction.

2.2.3 Long term statistics

When designing a construction at sea, it is also interesting to study how the sea state varies during the lifetime of the construction, this is called long term statistics and identifies how many storms and extremes the construction will experience. This is used when studying the fatigue and extreme response of a construction.

2.3 Coupled motion in multiple degree of freedom system

When considering a multiple degree of freedom system, it is convenient to express the equation of motion in matrix form. An example, shown in Figure 17, of a two degree of freedom system from Inman (2008) is shown to describe how this can be done.

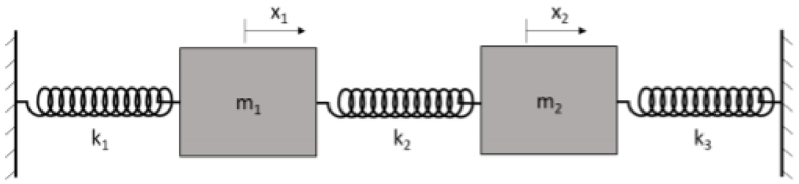

Figure 17: Example of system with two degrees of freedom (Inman, 2008).

The equation of motion can be established from a free body diagram shown in Figure 18.

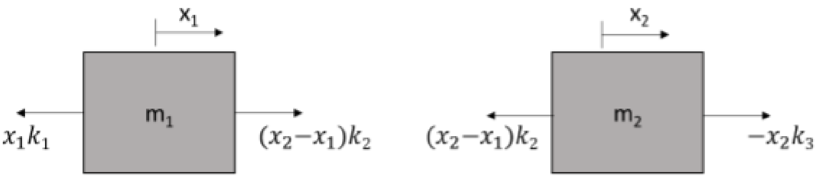

Figure 18: Free body diagrams of the masses in Figure 17 (Inman, 2008).

The equilibrium equations can be written as shown in Equation 34 and Equation 35.

$$m_1\ddot{x}_1 + (k_1 + k_2)x_1 - k_2x_2 = 0 \tag{34}$$

$$m_2\ddot{x}_2 - k_2x_1 + (k_2 + k_3)x_2 = 0 \tag{35}$$

The unknowns, **x**, their mass, **M**, damping, **C**, and stiffness, **K**, and the excitation forces, **F**, are listed in matrix form as shown in Equation 36, Equation 37, Equation 38, Equation 39, and Equation 40, respectively.

$$\mathbf{x} = \begin{bmatrix} x_1 \\ x_2 \end{bmatrix}. \tag{36}$$

$$\mathbf{M} = \begin{bmatrix} m_1 & 0 \\ 0 & m_2 \end{bmatrix}. \tag{37}$$

$$\mathbf{C} = \begin{bmatrix} 0 & 0 \\ 0 & 0 \end{bmatrix}. \tag{38}$$

$$\mathbf{K} = \begin{bmatrix} k_1 + k_2 & -k_2 \\ -k_2 & k_2 + k_3 \end{bmatrix}. \tag{39}$$

$$\mathbf{F} = \begin{bmatrix} 0 \\ 0 \end{bmatrix}. \tag{40}$$

From these matrices, the equation of motion of the two degree of freedom system can be written as Equation 41.

$$\mathbf{M}\ddot{\mathbf{x}} + \mathbf{C}\dot{\mathbf{x}} + \mathbf{K}\mathbf{x} = \mathbf{F}. \tag{41}$$

By considering this example as a free vibration, undamped, two degree of freedom system the following equation of motion will apply:

$$\mathbf{M}\ddot{\mathbf{x}} + \mathbf{K}\mathbf{x} = 0, \tag{42}$$

with the following assumed solution to **x**:

$$\mathbf{x} = \mathbb{R}\mathrm{e}\left\{\tilde{\mathbf{x}} e^{i\omega t}\right\}, \tag{43}$$

where $\tilde{\mathbf{x}}$ is a vector of unknown complex constants.

By combining the two equations above, the following equation of motion is obtained:

$$\left(-\omega^2\mathbf{M} + \mathbf{K}\right)\tilde{\mathbf{x}} e^{i\omega t} = 0. \tag{44}$$

The interesting solutions for **x** are the nonzero ones, which can be found by the *characteristic equation* formulated as Equation 45.

$$\det\left(-\omega^2 M + K\right) = 0, \tag{45}$$

where *det* is the determinant, and ω is the natural frequencies of the two systems: ω_1 and ω_2.

2.4 Mooring systems

The next part of this theory section regarding mooring systems and mooring line materials, will follow the explanations from Faltinsen (1998), Larsen (2020), Chakrabarti (2005) and Vryhof (2005).

A mooring system can provide stiffness in two different ways, geometrically, k_G, and elastically, k_E, as shown in Equation 46. Geometric stiffness can be provided by an inextensional mooring line, where a tension change leads to a change in the shape of the mooring line. An elastic mooring line, on the other hand, can provide elastic stiffness by stretching, and changing its length, when exposed to a higher tension.

$$\frac{1}{k_{tot}} = \frac{1}{k_G} + \frac{1}{k_E} \tag{46}$$

The geometric stiffness can be estimated from the horizontal tension, T_x, calculated by Equation 47.

$$T_x = \frac{wa}{y}, \tag{47}$$

where w is the weight of the mooring line, a is the momentum arm from the resulting vertical weight w to the fairlead, and y is the water depth.

The geometric stiffness can then be calculated as presented in Equation 48 with respect to the initial horizontal tension T_{x0}.

$$k_G = \frac{T_x - T_{x0}}{\Delta a}. \tag{48}$$

The elastic stiffness, k_E, can be estimated from the line length, l, and the axial stiffness of the mooring line, EA, as presented in Equation 49.

$$k_E = \frac{EA}{l}. \tag{49}$$

The static equilibrium of a segment in a catenary mooring line and the general mooring line characteristics can be seen in Figure 19.

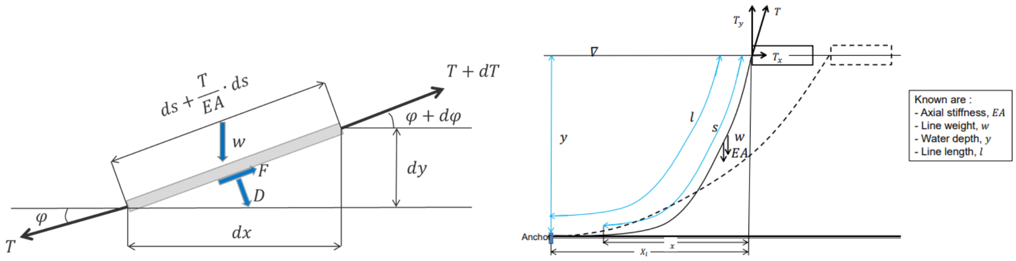

(a) Static equilibrium of mooring line segment.

(b) Mooring line characteristics.

Figure 19: Mooring line definition (Larsen, 2020).

The forces acting on an mooring line element can be calculated in the tangential and radial direction with Equation 50 and 51, respectively.

$$dT = \left[w \sin\varphi - F \left(1 + \frac{T}{EA} \right) \right] ds. \tag{50}$$

$$T d\varphi = \left[w \cos\varphi + D \left(1 + \frac{T}{EA} \right) \right] ds. \tag{51}$$

w denotes the weight of the mooring line, F and D are the mean hydrodynamic forces per unit length acting in the tangential and normal direction, respectively, EA is the axial stiffness of the mooring line, and T represents the line tension.

2.4.1 Catenary line

A catenary is a uniform, flexible, inextensional string. The restoring force is provided by the weight of the mooring line, and changed by lifting or lowering the line. This is the geometric stiffness, k_G. As shown in Figure 20, part of the mooring line lies on the seabed in a horizontal position. Therefore, the attached anchor system must withstand large horizontal forces but generally does not have to be designed to withstand vertical forces.

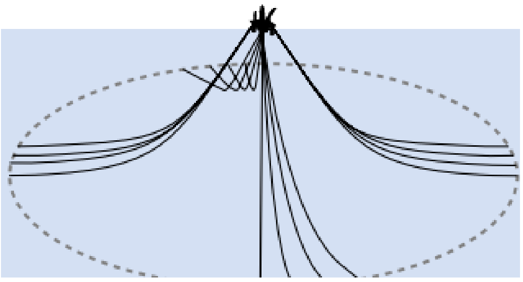

Figure 20: Catenary mooring line (Vryhof, 2005).

The horizontal distance, X, from the anchor to the connection point of a catenary mooring line can be calculated with Equation 53 (Faltinsen, 1998). This can be used for all lines within the limit explained by Equation 52, where T is the restoring force and EA the axial stiffness in the mooring line.

$$\frac{T}{EA} << 1. \tag{52}$$

$$X = l - y\left(1 + 2\frac{T_H}{wy}\right)^{\frac{1}{2}} + \frac{T_H}{w}\cosh^{-1}\left(1 + \frac{wy}{T_H}\right). \tag{53}$$

l represents the length, T_H the horizontal tension, and w the weight of the mooring line, and y represents the water depth.

2.4.2 Taut line

Taut lines are tightened under high constant tension as a straight line from the connection point to the anchor, as seen in Figure 21. Due to the relatively short length, taut lines have low net submerged weight. The restoring force comes from a stretch of the lines with elastic spring-like properties providing elastic stiffness, k_E. Taut lines are suitable for deep water and calmer wave environment with low tidal differences.

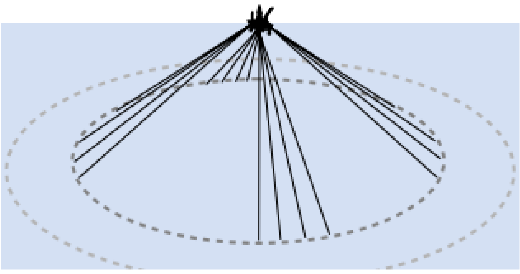

Figure 21: Taut line mooring line (Vryhof, 2005).

The characteristics of an elastic line, like the taut line, can be found from equation Equation 54 (Faltinsen, 1998).

$$x = \frac{T_x}{w}\sinh^{-1}\left(\frac{T_y}{T_x}\right) + \frac{T_x T_y}{wEA}, \tag{54}$$

where T_x and T_y represents the horizontal and vertical tension and can be found from:

$$T_x = EA\left[\sqrt{\left(\frac{T}{EA}+1\right)^2 - \frac{2wy}{EA}} - 1\right] \quad \text{and} \quad T_y = wl, \tag{55}$$

where EA is the axial stiffness in the mooring line material, T is the pre-tension, w is the weight of the mooring line, y is the water depth, and l is the lenght of the elastic line.

2.5 Mooring line materials

2.5.1 Chain

Steel bars rolled into links are connected to make a chain. The two main types of chains are studless and stud-link chain, shown to the left and right of Figure 22, respectively. Permanent mooring usually uses a studless chain as it reduces the weight per unit of strength and makes the line less prone to fatigue damage. Stud link chain prevents knotting and makes handling easier, but has a shorter fatigue life because of sensitivity to tightening. If constant tension is expected after installation, there will be a low risk of knotting (Chakrabarti, 2005).

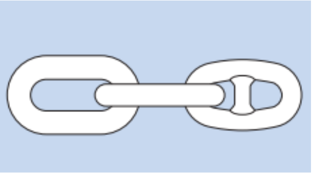

Figure 22: Chain (Vryhof, 2005).

2.5.2 Wire

There are three main types of wire: spiral strand, six strand rope, and multi-strand, seen in Figure 23, where six strand rope is most common in offshore mooring. The pitch of the winding determines the flexibility and axial stiffness of the strand. Wires have lighter, more elastic characteristic than a chain for the same breaking load, but are more expensive and more susceptible to corrosion (Chakrabarti, 2005).

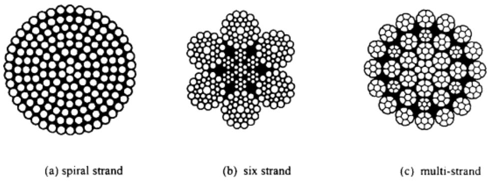

Figure 23: Wire (Vryhof, 2005).

2.5.3 Synthetic rope

A recently developed mooring line material is synthetic fiber rope. The light weight and high breaking strength of the synthetic rope make it useful for deep water mooring. The elasticity of the material prevents excessive dynamic tension by absorption. A combination of chain and synthetic rope or a point mass or floaters can be used to adjust the self-weight and shape of the mooring line (Chakrabarti, 2005).

2.6 Design regulations and criteria for the mooring system of a floating offshore wind turbine

When designing a mooring system for a floating offshore wind turbine, different design criteria from, e.g., *DNV GL* and *IEC*, must be considered. *DNV GL Group AS* is a risk and classification company which has developed specific criteria for such a system, which will be considered in this project. They have issued a standard for floating offshore wind turbines called *DNVGL-ST-0119 Floating wind turbine structures* (DNVGL-ST-0119, 2018), with regulations for structural design and mooring systems. For mooring systems, another standard called *DNVGL-OS-E301 Position mooring* (DNVGL-OS-E301, 2018), must also be used. One of the main criteria for designing a mooring system is that the mooring line's capacity must be large enough to withstand the forces. This can be tested by performing a so-called ultimate limit state test on the mooring lines. Equation 56 from DNVGL-ST-0119 (2018) states that the characteristic capacity, S_C, of the material in the mooring line must be larger than the design load, T_d.

$$S_C > T_d. \tag{56}$$

The characteristic capacity, S_C, can be calculated from Equation 57.

$$S_C = 0.95 * S_{mbs}, \tag{57}$$

where S_{mbs} is the breaking strength of the material in the mooring line and 0.95 represents a 5% safety factor due to uncertainties.

Equation 58 can be used to calculate the design load, T_d.

$$T_d = \gamma_{mean} * T_{c,mean} + \gamma_{dyn} * T_{c,dyn}. \tag{58}$$

γ_{mean} and γ_{dyn} are safety factors shown in Table 1 below, and $T_{c,mean}$ and $T_{c,dyn}$ are the characteristic mean and dynamic tension, respectively.

	γ_{mean}	γ_{dyn}
Normal safety factor	1.3	1.75
High safety factor	1.5	2.2

Table 1: Load factor requirements for design of mooring lines

Additionally, *Equinor* presented some design restrictions to the system. The maximum offset in one horizontal direction can never exceed 25% of the water depth, while in the other horizontal direction, the offset must not be larger than 15% of the water depth. This is due to the tolerance in the power cable connected to the wind turbines. These restrictions were implemented to the ultimate limit state test.

3 Method

3.1 Environmental statistics from the area of interest

To determine the environmental forces the model would be exposed to, statistics from the area of interest were studied. *Station 46059* on *National Data Buoy Center* (NDBC, 2020) was decided to be the most relevant observation site. This station is located 357 NM, which equals approximately 660 km, west of San Francisco, CA. The station can be seen in Figure 24 and is a 3-meter high discus buoy with a steel cage on top. The station measures different parameters, like pressure, temperature, and velocity, of both the air and the water. A table of historical meteorological data, created January 15^{th} 2010, was assumed to be representative of the relevant area. This table contained measurements from October 1994 to December 2008. The maximum, average, and minimum monthly wind speed, significant wave height, and wave period were used to determine the simulation parameters.

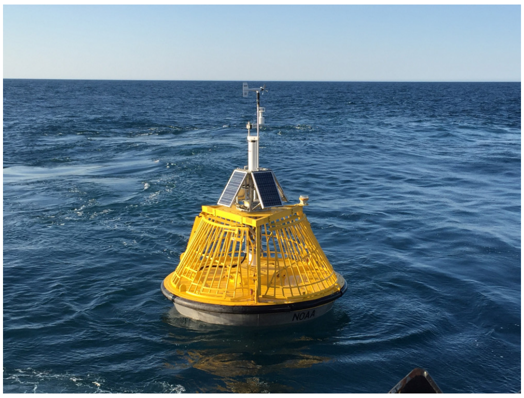

Figure 24: Station 46059 NDBC (2020).

The wind speed is measured 3.8 m above the sea surface at the station, and corrected to the standard height of 10 m in the online data. When these measurements were used in the simulations, they had to be adjusted by Equation 59 from (DNVGL-RP-C205, 2017) to find wind speed at the hub height, z, of the model.

$$U = \left(\frac{z}{10}\right)^{\alpha} U_{10}. \tag{59}$$

A power-law exponent, α, of 0.12 was used according to DNVGL-RP-C205 (2017) for open sea with waves.

3.2 OO-Star Wind Floater

The wind turbine floater used in this project was developed by *Dr.techn.Olav Olsen AS*, a Norwegian engineering company within structural and marine consulting. The model *OO-Star Wind Floater* is a star-shaped, semi-submersible floater concept, which can be seen in Figure 25. The model has a passive ballast system, and the foundation consists of a star-shaped pontoon supporting three buoyancy cylinders to optimize the stability (Landbø, 2013).

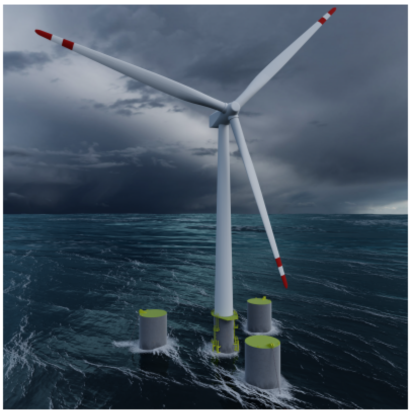

Figure 25: OO-Star Wind Floater developed by Dr.techn.Olav Olsen AS.

During the fall of 2020, *DR.techn.Olav Olsen AS* released a statement on their web site seen in Olsen (2020). The article announced that a full scale model of the *OO-Star Wind Floater* was going to be built. The statement says: *”The EU has pledged to fund EUR 25 million to a strong European consortium led by the world’s largest wind power producer Iberdrola to demonstrate the full scale OO-Star Wind Floater”* (Olsen, 2020). The floating semi-submersible wind turbine foundation concept with a 10 MW wind turbine is planned to be built on a test center. If realized, this will be the world’s largest floating wind turbine.

3.3 SIMA

The computer software used for simulation in this project is called *SIMA*, a simulation workbench for marine operations and mooring analysis developed by *SINTEF*. The workbench offers a complete solution for simulation and analysis of marine operations and floating systems (SINTEF, 2019).

The software can do a coupled analysis of floating structures through two subprograms named *RIFLEX* and *SIMO* to solve a problem (DNVGL, 2019). For a floating wind turbine, *RIFLEX* uses finite element methods on the mooring lines, the tower, and the blades, whereas *SIMO* solves the equation of motion with the mass and stiffness matrix provided by *RIFLEX*. A simulation outline for a coupled analysis in *RIFLEX* and *SIMO* is presented in Figure 26.

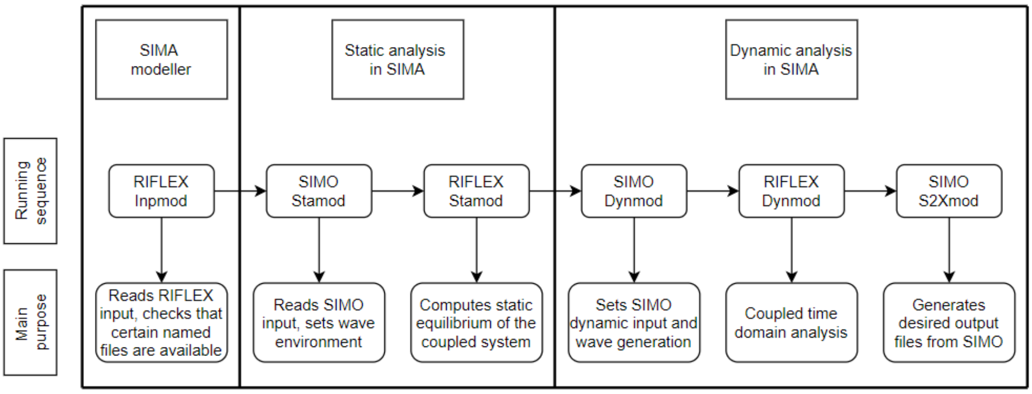

Figure 26: Simulation outline in SIMA (Bachynski, 2019).

The simulations in this project were performed with a *JONSWAP* wave specter, with different input values of the significant wave height, H_s, and wave period, T_p. The simulated turbulent wind files, with different mean wind speeds, were created in the computer program *TurbSim* using the *Kaimal* wind specter (Jonkman and Buhl Jr, 2006).

3.3.1 Initial model

A *SIMA*-model of the *OO-Star Wind Turbine Floater* was handed out and can be seen in Figure 27.

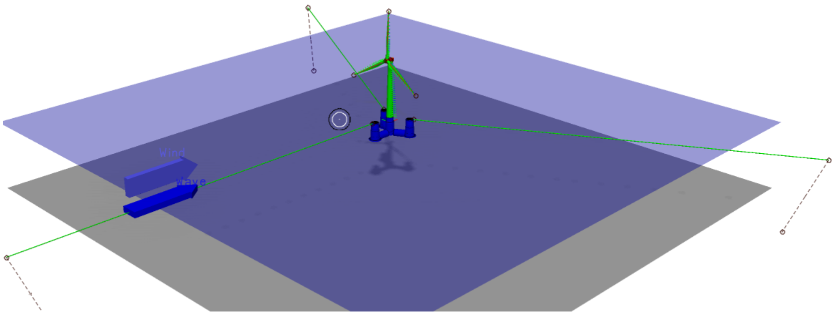

Figure 27: OO-Star Wind Turbine Floater in SIMA

The orientation of the semi-submersible, seen in Figure 28, shows a star-shaped floater with three pontoons and a cylinder in the center as a foundation to the wind turbine. A technical drawing from Müller et al. (2018) showing the main dimensions of the model can be seen in Figure 29.

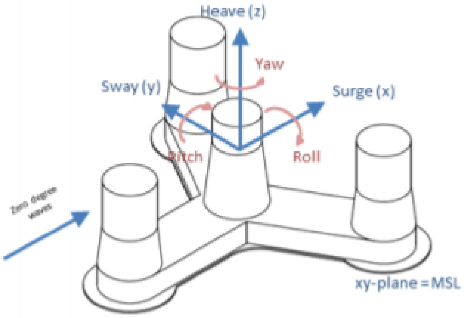

Figure 28: Müller et al. (2018)

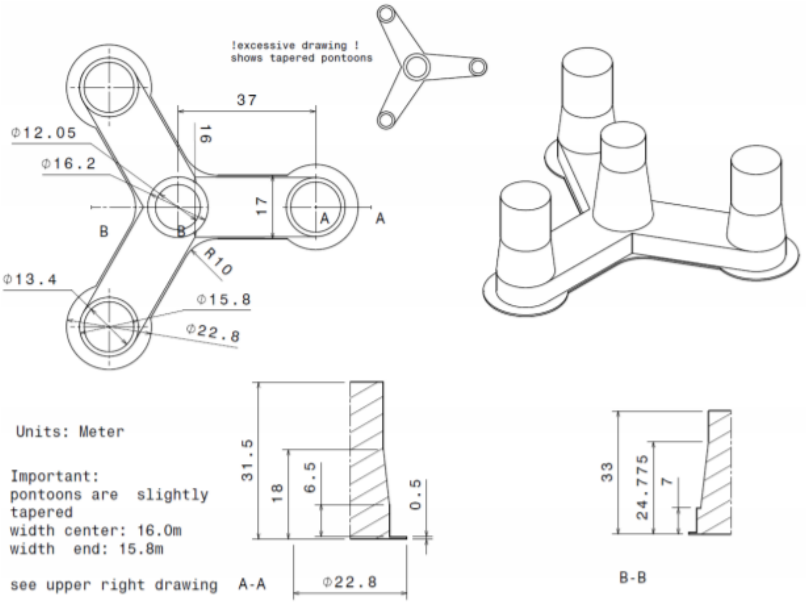

Figure 29: Müller et al. (2018)

The initial model was at a water depth of 130 m and had all chain mooring lines. The mounting of the mooring lines to the semi and a drawing of the mooring system can be seen in Figure 30. The pre-tension in the mooring lines was 1670 kN.

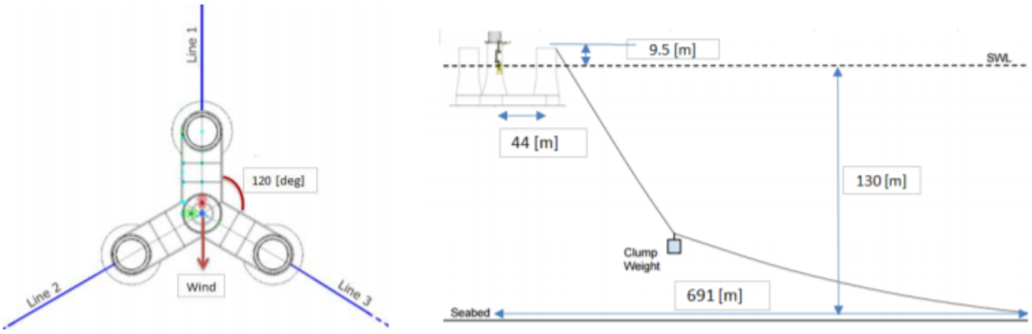

Figure 30: Initial mooring system at 130 m (Müller et al., 2018).

The input properties of the mooring lines in *SIMA* are listed in Table 2.

	Chain in mooring line
Diameter [m]	0.246
Mass in air [kg/m]	375.38
Length [m]	703
Axial stiffness [MN]	1506
Breaking strength [MN]	1000
Quadratic drag coefficient	2

Table 2: Mooring line properties on initial model.

The wind turbine used in the model was the *DTU 10 MW Reference Wind Turbine* developed by the *Technical University of Denmark - DTU*. The main properties of this wind turbine can be seen in Table 3 from Bak et al. (2013).

Rating	10 MW
Rotor orientation, configuration	Upwind, 3 blades
Control	Variable speed, collective pitch
Drivetrain	Medium speed, Multiple stage gearbox
Rotor, Hub diameter	178.3 m, 5.6 m
Hub height	119 m
Cut-in, Rated, Cut-out wind speed	4 m/s, 11.4 m/s, 25 m/s
Cut-in, Rated rotor speed	6 RPM, 9.6 RPM
Rated tip speed	90 m/s
Overhang, Shaft tilt, Pre-cone	7.07 m, 5°, 2.5°
Pre-bend	3.3 m
Rotor mass	229 tons (each blade $\sim$ 41 tons)
Nacelle mass	446 tons
Tower mass	605 tons

Table 3: Main properties of DTU 10 MW (Bak et al., 2013).

3.3.2 Modification and simplification of the model

The initial model was simplified before simulations were performed on the new mooring systems to reduce computational time. The simplifications and modifications of the model will be described in this section.

The water depth was changed from 130 m to 700 m, to modify the model to the area of interest.

As the material in the mooring lines was changed in size, length, and weight for the new mooring systems, the ballast weight of the semi-submersible had to be modified to float as intended. This was done by changing the ballast weight included in the structural mass of the semi from its initial value of 2.1709×10^7 kg. Due to relatively small changes in the mass, the inertia of the model was assumed to be unchanged.

The blades on the wind turbine were removed and replaced with quadratic wind coefficients on the nacelle. To account for the removal of the blades, their weight was added to the nacelle mass, which was changed from 446 tons to 569 tons. The thrust force created by the wind on the blades was substituted by a quadratic wind coefficient on the nacelle. This coefficient, C_{wind}, can be approximated by Equation 60.

$$C_{wind} = \frac{T}{U^2}, \tag{60}$$

where T is the thrust force and U is the wind speed.

The coefficients were calculated based on the results from a constant wind simulation on the initial model. The estimated coefficients used in the simulations can be seen in Table 17 in Section 4.3.1.

For the system including two turbines, more simplifications were made. These were done due to long simulation time, as well as limited computer capacity and storage. The element lengths of the polyester parts of the mooring lines were increased from 25 m to 50 m. The time step in SIMA was also increased from 0.01 s to 0.05 s. These simplifications resulted in a 27 494 s reduction of the simulation time, as shown in Table 4.

	Initial parameters	New parameters	Difference in %
Simulation time [s]	33091	5597	-83.1
Time step in SIMA [s]	0.01	0.05	+400
Polyester element length [m]	25	50	+100

Table 4: Comparison of parameters with long and short simulation time

A comparison was done between a 1 hour turbulent wind test with equal environmental inputs for the initial and the new parameters, and the results are shown and discussed in Section 4.3.2.

Another modification made to the system, including two wind turbines, was to account for the wake deficit in the rear turbine's quadratic wind coefficient. Equation 13 was used to calculate the wind speed experienced by the rear wind turbine, and the above mentioned constant wind test was used to estimate which thrust force this new wind speed would provide. The results of this estimation and the adjusted coefficients can be seen in Table 19 and are discussed in Section 4.3.3.

3.4 Mooring systems

Throughout the design process, the criteria described in Section 2.6 were followed to develop some suggested mooring systems. The initial design criteria and the materials used in these systems will be presented, followed by the two suggestions for a single wind turbine mooring system, and a park-level mooring system.

3.4.1 Initial design criteria

The mooring systems were designed to be comparable to the mooring system of *Hywind Scotland*, and the proposed mooring system of *Hywind Tampen*. Due to the stiffness in yaw provided by the star-shaped semi-submersible floater used in this project, a bridle was not considered necessary.

In the initial design process, the systems were exposed to a constant force of 1500 kN in surge direction, hence parallel with *Line 1*. The magnitude of the force was determined by a preliminary constant wind simulation on the initial model and represented the thrust force. The resulting offsets and mooring line tensions were studied and evaluated according to the following criteria before further simulations were performed:

- The maximum mooring line tension should be lower than 20% of the breaking strength of the selected mooring line material to increase the chance of passing the ultimate limit state test.
- The maximum horizontal offset in surge must not exceed 10% of the water depth of 700 m, to decrease the chance of exceeding the limitation of the power cable.
- The mooring lines should be as short as possible to minimize the total cost.
- The polyester part of the mooring line should not be in contact with the seabed to avoid complications.
- No slack line events in the mooring lines should be observed to reduce the risk of snap loads.

3.4.2 Materials

The mooring lines in the systems suggested in this project were designed as chain-polyester-chain configurations. The chain was selected from the product catalog of *Ramnäs Bruk AB*, and the polyester was selected from the product catalog of *Bridon-Bekaert The Ropes Group*. After consulting with Professor Kjell Larsen, it was decided to use R3S stud-less chain and superline polyester for permanent mooring, as the mooring line materials.

The axial stiffness of chain was calculated according to DNVGL-OS-E301 (2018) with Equation 62. The elastic modulus of chain was calculated in N/m^2 with Equation 61 from DNVGL-OS-E301 (2018).

$$E_{chain} = (5.40 - 0.004d)10^{10}, \tag{61}$$

where d is the diameter of the chain in *mm*.

$$EA_{chain} = E_{chain}\frac{\pi}{4}d^2, \tag{62}$$

where d is the diameter of the chain in *m*.

The axial stiffness of polyester was calculated with Equation 63. The factor of 20 was decided after consulting with Professor Kjell Larsen, as this was common industry practice in the design process. However, this estimated axial stiffness of polyester must be critically reviewed as it depends on the pre-tension of the mooring line and could be non-linear in reality.

$$EA_{polyester} = 20 \cdot MBS, \tag{63}$$

where MBS is the minimum breaking strength of the polyester.

The design process resulted in selecting chain and polyester sections with the properties listed in Table 5. These were implemented on the mooring line cross-sections in the *SIMA*-model. The difference of less than 3% in the breaking strength of the two materials makes the line consistent.

	Chain	Polyester
Diameter [m]	0.130	0.223
Mass in air [kg/m]	338	31.8
Axial stiffness [MN]	647.73	274.68
Breaking strength [MN]	14.139	13.734
Quadratic drag coefficient	2.4	1.6

Table 5: Chain and polyester properties

To estimate the cost of the mooring lines, Equation 64 from Xu (2020) was used. $Length$ is the length of the mooring line or segment in m, $Weight$ is the weight in air of the mooring line material in N/m, and $Price$ is the price of the material in NOK/N, resulting in the $Cost$ in NOK. The estimated price of the different materials, provided by *Equinor*, can be seen in Table 6.

$$Cost = Length * Weight * Price \tag{64}$$

	Chain	Polyester
Price [NOK/N]	2.5	7.0

Table 6: Chain and polyester properties

With the equation above, the cost of the mooring system of the initial model at 130 m water depth was estimated to 19.416 MNOK.

3.4.3 Single turbine mooring systems

With the materials described above, two mooring line systems were designed for a single wind turbine at 700 m water depth. The orientation of the mooring lines, *Line 1*, *Line 2* and *Line 3* as seen in Figure 30, was unchanged from the initial model. The mooring line characteristics are a result of applying a constant force, with varying value, on the model and measure the mean surge offset.

System 1

The first mooring system was designed as can be seen in Figure 31 with a total mooring line length of 1700 m. The mooring lines had 150 m chain in the top, 1300 m polyester in the middle, and 250 m of chain in the end. The mooring line characteristics of the system can be seen in Figure 33a, and shows the pre-tension of 815 kN. The total cost of the three mooring lines in this system was 18.464 MNOK, estimated with Equation 64.

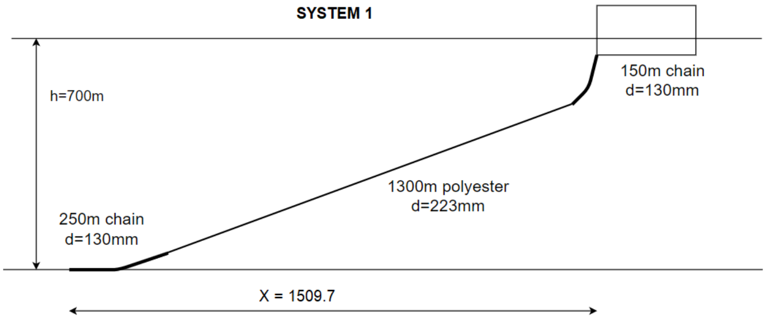

Figure 31: First mooring system suggestion for single wind turbine

System 2

Figure 32 shows the design of the second suggested mooring line system for a single wind turbine. This system had mooring lines with a total length of 2000 m, but as the figure shows, only a total chain length of 300 m, 150 m at each end. The pre-tension of this mooring line system was 1197 kN, and the total cost of this mooring system was estimated to 18.597 MNOK.

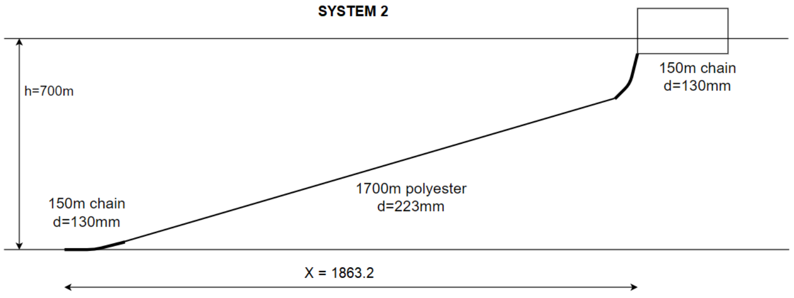

Figure 32: Second mooring system suggestion for single wind turbine

An overview and comparison of the dimensions in the two mooring systems are shown in Table 7. The semi mass is the changed structural mass of the substructure in *SIMA* to make it float, and X is referred to as the horizontal distance from the anchor to the connection point on the semi.

	System 1	System 2
Bottom chain [m]	250	150
Polyester [m]	1300	1700
Top chain [m]	150	150
Total length [m]	1700	2000
Semi mass [kg]	2.204×10^7	2.293×10^7
Pre-tension [kN]	815	1197
X-distance [m]	1509.7	1863.2

Table 7: Single mooring system

The mooring line characteristics of *System 1* and *System 2* are shown in Figure 33. The difference in pre-tension can be seen as the starting point of the mooring line tension, and shows the smaller pre-tension of 815 kN in *System 1* compared to 1197 kN in *System 2*. *System 1* had a total chain length of 400 m, compared to only 300 m in *System 2*. The polyester part was 1300 m in *System 1*, and 1700 m in *System 2*. The increased elastic stiffness, k_E, in *System 2* is the reason for the more linear slope, compared to *System 1* where the geometric stiffness, k_G, contributes more. The lower pre-tension and the larger contribution from the geometric stiffness in *System 1*, leads to the larger measured offset compared to the mooring line characteristic of *System 2*.

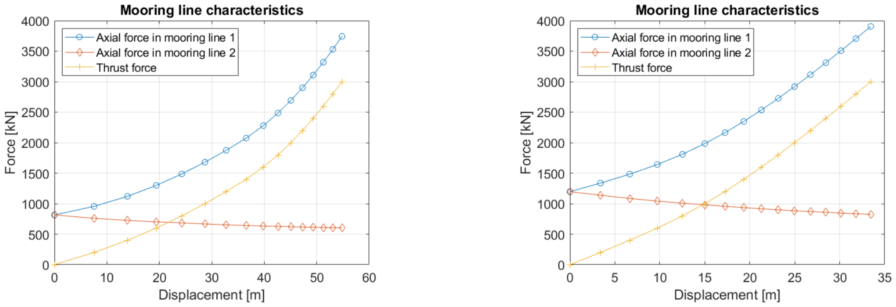

(a) Mooring line characteristics of mooring system 1

(b) Mooring line characteristics of mooring system 2

Figure 33: Mooring line characteristics of *System 1* (a) and *System 2* (b).

Another interesting observation when comparing the two systems is the estimated total cost. Even though the length of each mooring line was 300 m longer in *System 2* than in *System 1*, the total cost of *System 2* was less than 1% higher than *System 1*. This is due to the 100 m shorter chain length in *System 2* and exemplifies why polyester is interesting in deep water mooring with long mooring lines. It was also interesting to observe that the total costs of these mooring systems were estimated to be lower than on the initial system at 130 m with all chain mooring lines. However, the prices for chain and polyester are only estimates and may be different in reality.

3.4.4 Shared mooring system

After establishing two approved mooring system designs for a single wind turbine, a park-level mooring system was designed. This system was designed with two floating offshore wind turbines, each with two mooring lines connected to the seabed and their third and final mooring line connected as a shared one. The horizontal distance between the center of the two turbines was 1600 m, corresponding to approximately nine rotor diameters, which was determined after consulting with *Equinor*. Figure 34 shows this shared mooring line system from above and Figure 35 shows the system from the side.

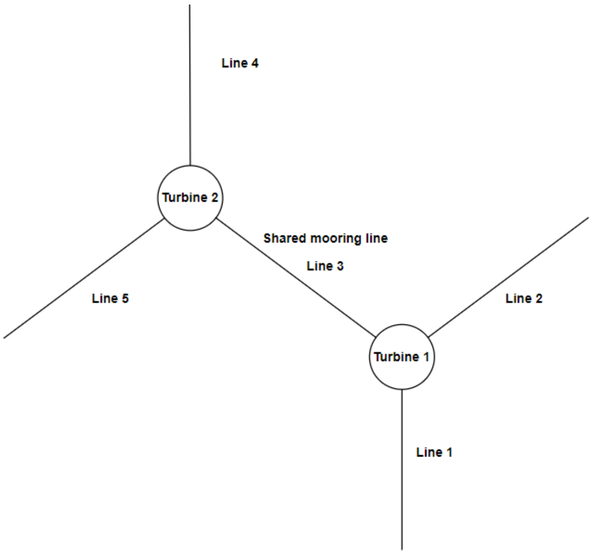

Figure 34: Shared mooring system from above.

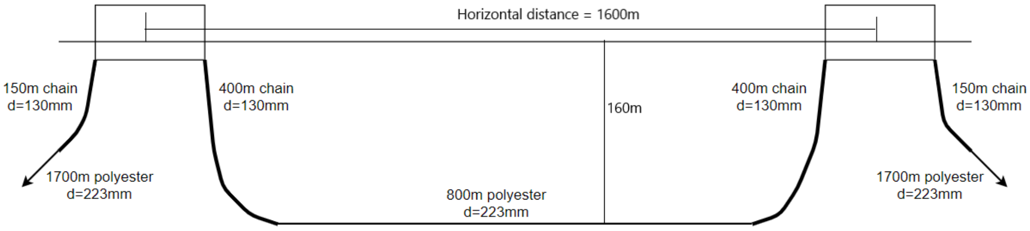

Figure 35: Shared mooring system from the side

The dimensions and properties of the bottom-connected and shared mooring lines in this system are described in Table 8. The structural mass of both semis was set to 2.296×10^7 kg to make them float.

	Bottom-connected mooring lines	Shared mooring line
Bottom chain [m]	150	400
Polyester [m]	1700	800
Top chain [m]	150	400
Total length [m]	1700	1600
Pre-tension [kN]	1819	1681
X-distance [m]	1875.6	-

Table 8: Shared mooring line system

The bottom-connected mooring lines were *Line 1*, *Line 2*, *Line 4*, and *Line 5* shown in the figures above. As can be seen they share the same dimensions as the ones described in *System 1* in Section 3.4.3. Their properties are also equal, except the fact that the pre-tension was changed to 1819 kN and the X-distance was changed to 1875.6 m. As can be seen in Figure 35, the shared mooring line had 400 m of chain in both ends and 800 m of polyester in the middle, resulting in a total length of 1600 m with pre-tension 1681 kN.

The total cost of this mooring line system was calculated to 33.175 MNOK, equaling 16.588 MNOK per turbine. Compared to the single mooring systems, this system reduces the total mooring line cost with approximately 2 MNOK, about 10%, per turbine. However, there will additionally be savings due to the reduced number of anchors. An estimation of this amount was not performed in this project.

The coupled dynamics of the shared mooring system made it challenging to design. A system with similar pre-tension in the bottom-connected lines and the shared mooring line was studied and was observed to be more stable. However, when exposed to environmental forces parallel to *Line 1*, the rear turbine, *Turbine 2*, pulled *Turbine 1* backward and sideways and resulted in large horizontal motions of this turbine and corresponding large tension in *Line 1*. The mooring system presented above, with larger pre-tension in the bottom-connected mooring lines than in the shared mooring line, resulted in a smaller horizontal motion of *Turbine 1* but increased horizontal motions of *Turbine 2*. The higher tension in *Line 5* than in the shared mooring line resulted in a more significant sideways motion of the rear turbine. Anyhow, on the foremost turbine, *Turbine 1*, *Line 2* countered the pulling force from the rear turbine, minimized the turbine's sideways motion, and resulted in a lower maximum tension in the exposed *Line 1*.

3.5 Simulations

3.5.1 Constant wind test

A constant wind test was simulated on the initial wind turbine model in an operational condition. This was done to discover the wind speeds impact on the wind turbine. The input parameters of the simulation can be seen in Table 9.

Simulation length	800 s
Simulation time step (Time step in SIMA)	0.005 s
Wave/body response time step (Time increment in SIMA)	0.1 s
Turbine condition	Operational
Wind input	Constant
Wave conditions	Hs = 0.001 m, Tp = 20 s

Table 9: Simulation parameters for the constant wind test.

Twelve constant wind speeds within the wind turbines operational limits were simulated to observe how the output properties changed for wind speeds under, at, and over the rated wind speed of 11.4 m/s. The simulated wind speeds are presented in Table 10.

Constant wind speed [m/s]											
4	6	8	10	11.4	12	14	16	18	20	22	24

Table 10: Constant wind speeds simulated.

The results from this constant wind test are presented in Section 4.2 and were used when replacing the blades with a quadratic wind coefficient as part of the simplification of the model.

3.5.2 ULS - worst case scenario

As part of the design process, the mooring systems had to be tested to verify that they satisfied the design criteria. A worst case scenario was created based on the environmental conditions in the area of interest and the thrust curve from the constant wind test. Six different wave and wind seeds were simulated for 1 hour, and the resulting axial mooring line tension was studied to ensure that the design tension, T_d, in the mooring lines did not exceed the characteristic capacity, S_C. The characteristic capacity was calculated with Equation 57 based on the selected mooring line materials described in Section 3.4.2, and resulted in $S_C = 13\,047\,\mathrm{kN}$. The minimum measured axial mooring line tension was also studied to make sure slack lines, which may cause snap loads, did not occur. The maximum horizontal offsets of the systems were also measured to make sure they did not exceed the limits of 15% and 25% of the water depth of 700 m, equal to 105 m and 175 m.

The fixed simulation parameters in *SIMA* can be found in Table 11, and the wave and wind seeds can be seen in Table 12.

On the single turbine mooring systems, the environmental forces, wave and wind, were simulated to approach the turbines parallel with *Line 1*. The reason for this was to provoke the largest tension in the mooring line.

On the park-level system, the environmental force was also firstly simulated to approach the model parallel to *Line 1*. However, on this mooring system, the environmental forces were additionally simulated with an angle to approach the model parallel to the shared mooring line, *Line 3*. This was done both with and without considering wake deficit and changing the quadratic wind coefficients on the rear wind turbine.

Simulation length	4000 s
Simulation time step (Time step in SIMA)	0.01 s*
Wave/body response time step (Time increment in SIMA)	0.1 s
Turbine condition	Operational
Wind input	Turbulent with $U_{mean} = 10\,\mathrm{m/s}$** Wind seeds given in Table 12
Wave conditions	$H_s = 14\,\mathrm{m}$, $T_p = 12\,\mathrm{s}$ Wave seeds given in Table 12

Table 11: Constant environmental parameters in ULS test.

*Time step of 0.05 s for the shared mooring system due to limited computer capacity.

**When wake deficit was accounted for, a mean wind speed of 12 m/s was also simulated as this resulted in a wind speed of approximately 10 m/s experienced by the rear wind turbine.

Wave seed	Wind seed
113	1
114	2
205	3
206	4
207	5
208	6

Table 12: Wave and wind seed for each run in ULS test.

3.5.3 Decay test

Decay tests in the six different rigid body motions were performed on the initial model. This was simulated in *SIMA* by applying a ramp force on the structure, increasing until a desirable value. A constant force was applied after the ramp to keep the model at an offset and calm the surrounding environment before releasing the force and initialize the decay. An example of a ramp and constant force can be seen in Figure 36.

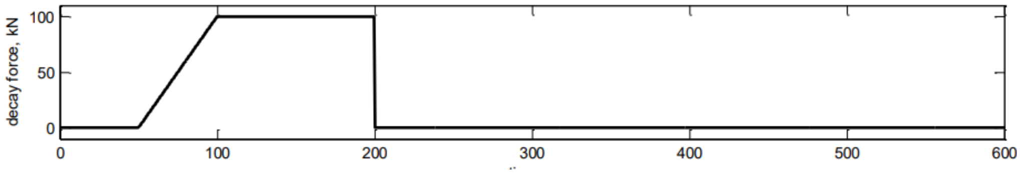

Figure 36: Example of decay force with ramp duration 50 s, starting from $t = 50$ s, and constant force duration 100 s.

The simulation parameters for the decay tests in the six rigid body motions are presented in Table 13. In the three rotations roll, pitch, and yaw, a moment rather than a force was applied. The reason for the differences in duration was to minimize the computational data, as the natural frequencies in heave, roll, and pitch are smaller and will decay faster.

Motion	Force/ Moment	Simulation length [s]	Point of application for decay force	Ramp duration [s]	Constant force duration [s]
Surge	1 000 kN	3 000	(0,0,-12)m	200	300
Sway	1 000 kN	3 000	(0,0,-12)m	200	300
Heave	10 000 kN	1 000	(0,0,-12)m	100	200
Roll	150 000 kNm	1 000	Round x-axis	100	200
Pitch	150 000 kNm	1 000	Round y-axis	100	200
Yaw	15 000 kNm	2 000	Round z-axis	100	200

Table 13: Simulation parameters for the decay tests.

The environmental parameters during the decay tests are presented in Table 14. These were constant during all the different decay tests and had to be different from zero to avoid computer software errors.

Simulation time step (Time step in SIMA)	0.01 s*
Wave/body response time step (Time increment in SIMA)	0.1 s
Turbine condition	Parked, blades feathered
Wind input	0.01 m/s constant wind
Wave conditions	Hs = 0.001 m, Tp = 20 s

Table 14: Environmental simulation parameters for the decay tests.

*Time step of 0.05 s for the shared mooring system due to limited computer capacity.

To calculate the natural periods, the time series of the wind turbine location was studied. The resulting coordinates of the wind turbine in the respective degree of freedom after initializing the decay were recreated, and the decay period of this recreated line was calculated.

The results from the initial model showed that the decay test in surge and sway were similar and resulted in an equal natural period. This was also the case for roll and pitch. Therefore, it was decided that decay tests only in surge, heave, pitch, and yaw were necessary for the designed mooring systems of a single wind turbine. Due to the lower pre-tension in the mooring lines of what was referred to as *System 1* in Section 3.4.3, a force of 100 kN rather than 1000 kN were applied with a duration of 400 s.

The decay test on the system with a shared mooring line was rather more complex. In heave, pitch, and yaw, the decay tests were performed as described above, with force applied on both turbines simultaneously. Due to the difference in pre-tension of the mooring lines, as shown in Table 8, the natural period in different horizontal directions had to be discovered. This was done by four different simulations described with Figure 37. *Test 1* was performed by applying the force parallel to *Line 1* and *Line 5* to detect the natural period in the motions parallel to this mooring line configuration. *Test 2* was performed by applying forces 90° to the ones in *Test 1*, to determine the natural period in this direction. *Test 3* was performed by applying a force on both turbines parallel to the shared mooring line, *Line 3*. This was done to find the natural period of the motion parallel to this mooring line configuration. In the final decay test, *Test 4*, the forces were applied 90° to the ones in *Test 3*.

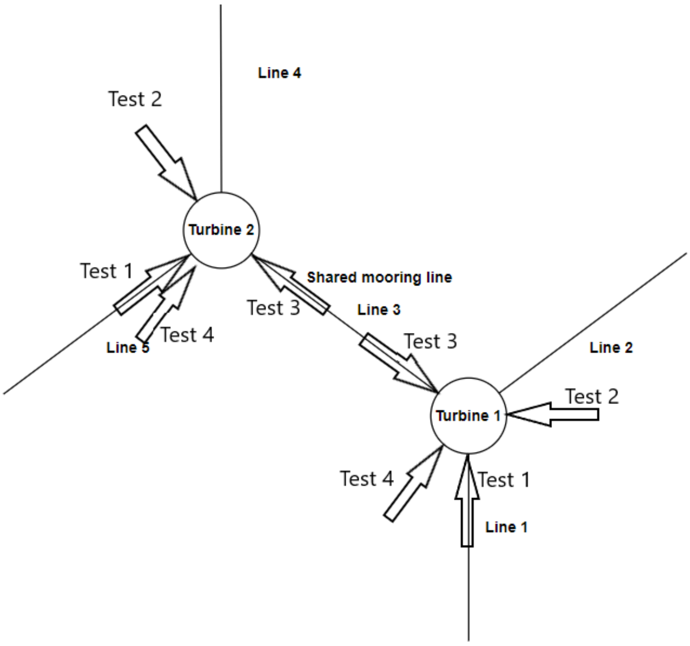

Figure 37: Decay test on shared mooring system.

3.5.4 Turbulent wind test

To study the behavior of the wind turbine when exposed to turbulent wind, as well as some relevant wave conditions, a response study was carried out. Some wind speeds under, at, and over the rated wind speed were simulated from a selection of handed out wind input files for the 10 MW turbine. These files were generated by the computer program *TurbSim* and used a *Kaimal* wind specter. From the results obtained in the metocean study, the significant wave heights and wave periods were selected to supplement the selected wind files. The waves were simulated with the 3-parameter *JONSWAP* specter in *SIMA*. The values of the different simulation parameters can be seen in Table 15.

As Figure 30 showed, the initial model was oriented so the environmental forces approached the wind turbine parallel to *Line 1*. This was also the case for the new designed mooring systems with a single wind turbine, and the first turbulent wind simulation on the park-level system. However, on the park-level system, the turbulent wind test was also performed with environmental forces attacking the wind turbines parallel to the shared mooring line, *Line 3* shown in Figure 34, approaching from between *Line 1* and *Line 2*. In this turbulent wind test, the wake deficit was accounted for in the quadratic wind coefficient on the rear turbine. The simulation was also performed without considering the wake deficit and changing the quadratic wind coefficient on the rear turbine as a comparison.

Each condition was simulated for 1 hour, and the fixed simulation parameters used in these tests can be seen in Table 16.

Condition number	T_p **[s]**	H_s **[m]**	U_{mean} **[m/s]**	**Turbulence intensity [%]**	**Wave seed**	**Wind seed**
1	4	1	4	30.1	101	1
2	4	1	4	30.1	102	2
3	5	1	6	23.6	103	1
4	5	1	6	23.6	104	2
5	6	2	8	20.3	105	1
6	6	2	8	20.3	106	2
7	8	3	10	18.3	107	1
8	8	3	10	18.3	108	2
9	8	4	12	17	109	1
10	8	4	12	17	110	2
11	12	5	14	16.1	111	1
12	12	5	14	16.1	112	2
13	15	9	18	14.9	113	1
14	15	9	18	14.9	114	2
15	15	12	20	14.4	115	1
16	15	12	20	14.4	116	2

Table 15: Environmental simulation parameters for each run in the turbulent wind test.

Simulation length	4000 s
Simulation time step (Time step in SIMA)	0.005 s
Wave/body response time step (Time increment in SIMA)	0.1 s
Turbine condition	Operational
Wind input	Turbulent, given in Table 15
Wave conditions	Given in Table 15

Table 16: General simulation parameters for the turbulent wind test.

The resulting turbine translations and rotations were studied, as well as the tension in the different mooring lines. A frequency study of the tension in the mooring lines was performed to see which frequencies, and corresponding periods, affected the dynamic change in the tension. As this frequency study was time-consuming, it was only performed with the results from conditions 7 and 15, from Table 15, of the different systems.

4 Results and discussion

4.1 Environmental statistics from the area of interest

4.1.1 Wind speed

From the environmental data at the observation site, the maximum, average, and minimum monthly measured wind speed, adjusted to the hub height of 119 m, are presented in Figure 38. The upper graph shows the results from the maximum measured wind speed and varies from 34.61 m/s in January to 19.68 m/s in August.

The middle graph presents the average monthly wind measurements in Figure 38. The results show that the mean measured wind speed is almost constant throughout the entire year. The total mean is calculated to 10.5 m/s.

The minimum measured wind speed is presented as the lower, graph on Figure 38.

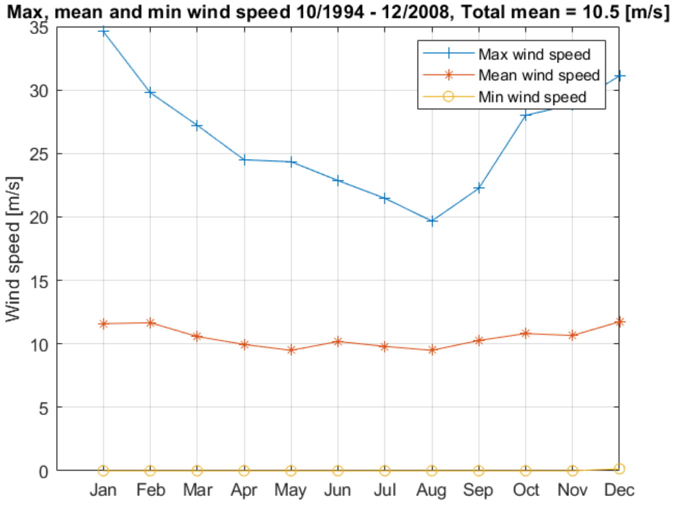

Figure 38: Wind speed measured at *Station 46059*, adjusted to hub height 119 m.

There were done some alterations with the wind speed measurements to correct for the change in height from where the measurements were done to the turbine hub height. This leads to a mean wind speed right in the rated wind speed area, but the alterations may have led to incorrect results. The results show that the maximum measured wind speed was above the cut-out wind speed of 25 m/s in six of the months.

The zero-measurements presented in the lower graph should be critically considered as this may be due to flaws in the measurement equipment.

4.1.2 Significant wave height

Figure 39 shows the maximum, average and minimum significant wave height measured at *Station 46059*. The maximum measured significant wave height is presented as the upper graph. The measurements shows large differences from 14.1 m in January to 4.3 m in August.

The mean measured significant wave height is presented as the middle graph and was highest in December, equal to 3.7 m, and at its lowest at 1.8 m in August. The total measured mean significant wave height is 2.7 m.

The minimum measured significant wave height has small variations but never exceeds 1 m. The lower graph on Figure 39 shows that the minimum is zero in March, September, October, and November. The highest measured minimum is 0.9 m in January and December.

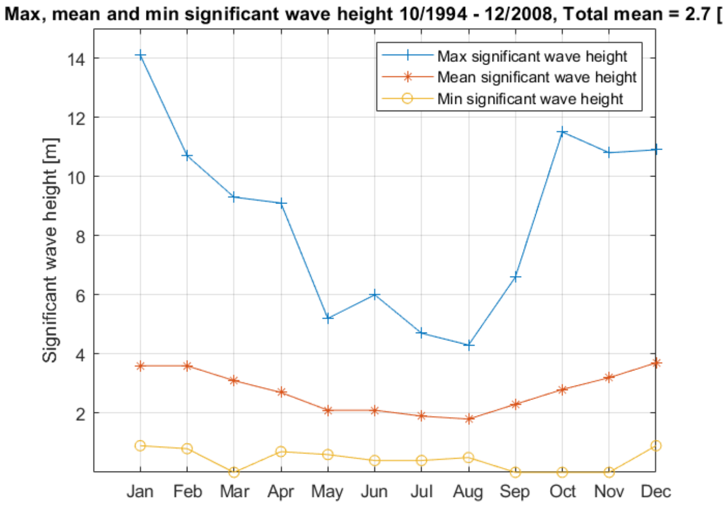

Figure 39: Significant wave height measured at *Station 46059*.

The zero-measurements should be critically considered as these results may be due to equipment flaws rather than actual measurements of zero significant wave height. The total mean significant wave height of 2.7 m is promising as this is relatively small and should make the mooring systems easier to design. However, wave heights up to 14 m are observed.

4.1.3 Wave period

The measured wave period at *Station 46059* is presented in Figure 40. The maximum measured wave period is shown as the upper graph and varies from 15.6 s in March to 11.1 s in June. The maximum measured wave period has another peak in November equal to 14.9 s.

The mean measured wave period is highest in December and equal to 8.2 s, and lowest in July and August, equal to 6.1 s. This can be seen as the middle graph of Figure 40, and the total measured wave period was 7.2 s.

The lower graph in Figure 40 represents the minimum measured wave period at *Station 46059*. The results show the highest value in December equal to 4.8 s, and a minimum in May equal to 3.7 s.

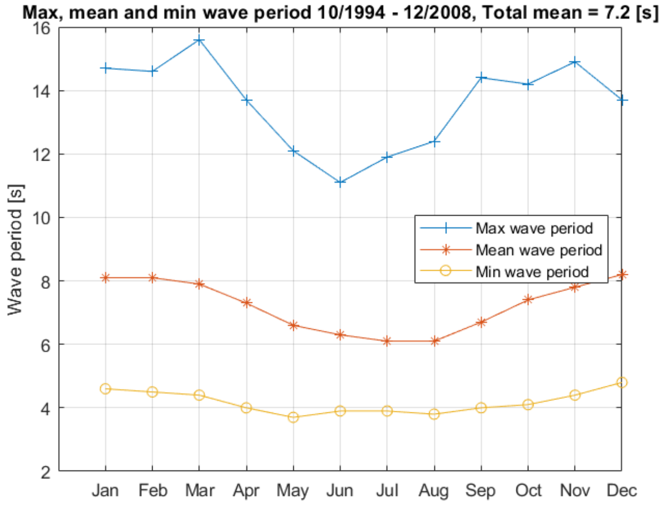

Figure 40: Wave period measured at *Station 46059*.

These metocean data were used to decide the input parameters in the other simulations in this project. The figures presented above are based on a summary file with measurements from 1994 to 2008. The fact that this file contained monthly measurements over a fourteen-year period was good. However, the measurements were between twelve and twenty-six years old, which may reduce the quality as the environment in the area could have changed.

The mean wind speed at hub height 119 m was 10.5 m/s, close to the rated wind speed of the wind turbine equal to 11.4 m/s. The total measured average significant wave height was 2.7 m, and the mean wave period was 7.2 s. This indicates that the weather conditions in the examined area are relatively calm, making mooring system design easier. Additionally, the results suggest that a wind turbine similar to the one used in this project would not experience wind conditions above its cut-out wind speed half the year. However, wind speeds under the cut-in wind speed of 4 m/s could occur and reduce the average power output.

4.2 Constant wind test on initial model

A constant wind test was performed on the initial model as described in Section 3.5.1 to understand how the wind turbine behaved when exposed to different wind speeds. The resulting thrust curve is presented in Figure 41. The maximum thrust force of 1381.1 kN was measured at a wind speed of 10 m/s.

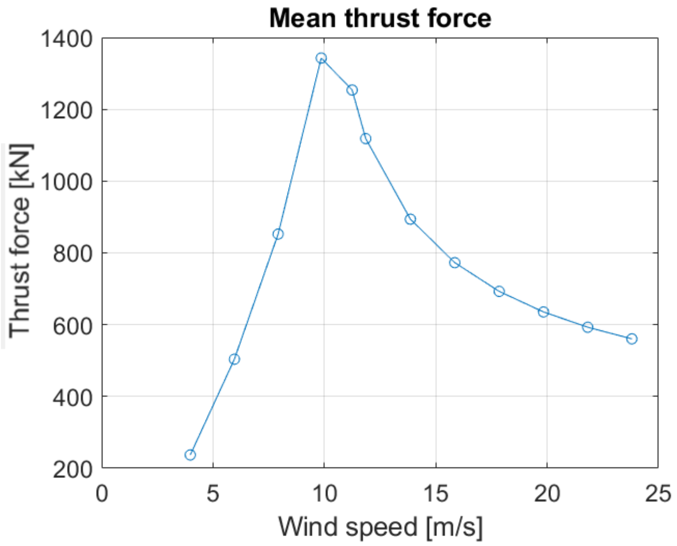

Figure 41: Thrust curve from constant wind simulation on initial model.

To demonstrate how the thrust force affected the supporting substructure, the resulting platform translations, in meters, and rotations, in degrees, are presented in Figure 42 and 43, respectively.

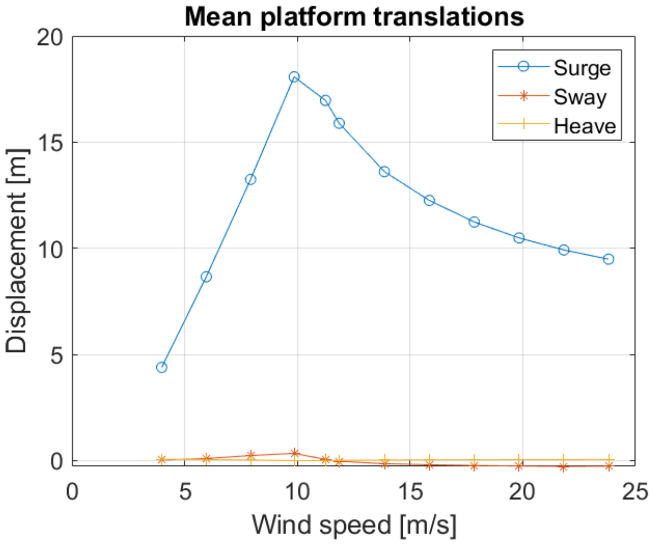

Figure 42: Platform translations from constant wind simulation on initial model.

As Figure 42 shows, the surge motion follows the thrust curve, and gets a maximum offset of approximately 17 m at wind speed 10 m/s. The offset in the two other translations, sway and heave, were minimal. This was because the environmental forces were simulated to approach the model in surge direction, and the relatively small wave height of 0.001 m was used as the simulation input.

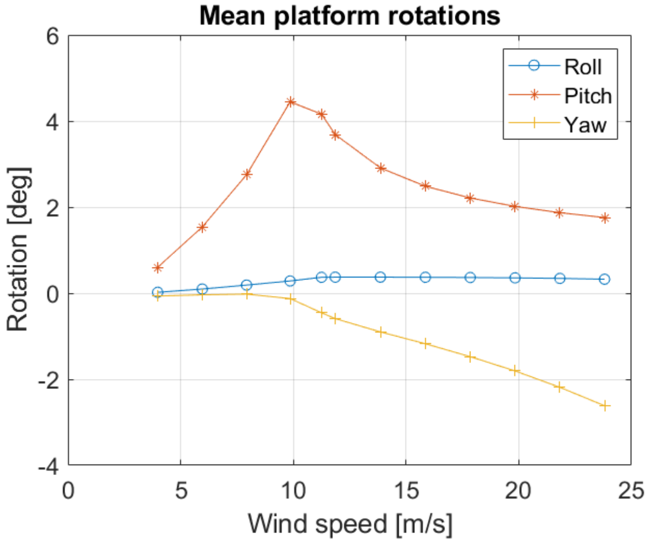

Figure 43: Platform rotations from constant wind simulation on initial model.

Figure 43 shows that the pitch rotation, likewise as the surge motion, followed the thrust curve and peaked at wind speed 10 m/s with a value of approximately 4.5 deg. The offset in roll was increasing until 10 m/s and was constant afterward, this was caused by the torque moment created by the spinning rotor. The offset in roll and the thrust force is the reason for the increasing offset in yaw.

By studying the constant wind tests, some interesting behavior of the wind turbine was observed. The thrust force determined the surge and the pitch motions because of the approach angle of the simulated wind. The thrust force was largest at wind speed 10 m/s, and larger than when the rated wind speed of the wind turbine, 11.4 m/s, was simulated. This indicates that the blades started to pitch before the rated wind speed was reached, but it can be assumed that a larger peak could be observed somewhere between 10 m/s and 11.4 m/s had more simulations been performed.

4.3 Model simplification

4.3.1 Blades replaced by quadratic wind coefficients

Based on the thrust curve resulting from the constant wind simulation, presented in Figure 41, the quadratic wind coefficient was calculated with Equation 60. The thrust forces on the wind turbine, the mean wind speeds, and the resulting quadratic wind coefficients are presented in Table 17.

U_{mean} [m/s]	Thrust force [N]	Quadratic wind coefficient, C_{wind} $[N/(m/s)^2]$
4	239600	14975
6	510660	14185
8	868928	13577
10	1381100	13811
12	1146384	7961.0
14	912537	4655.8
18	704894	2175.6
20	646240	1615.6

Table 17: Quadratic wind coefficient calculated from constant wind simulation on initial model

To verify that these quadratic wind coefficients were a valid substitute to the thrust force on the blades, the results form the turbulent wind simulations, described in Section 3.5.4, of the initial and the simplified model, were compared. The platform translations and rotations, as well as the axial force in the mooring lines, were compared.

Figure 44 shows the resulting platform translations from the turbulent wind simulation on the initial and the simplified model, as Figure 44a and Figure 44b, respectively. As can be seen, the results are similar, but the error bars showing the standard deviation of the measurements are larger on the simplified model. It can also be observed that the mean measured offset in surge was consistently slightly larger on the simplified model compared to the results from the initial model. The mean offset in surge at 10 m/s on the initial model was approximately 17 m, compared to approximately 18 m on the simplified model. However, the curves and the results are relatively equal, and the fact that the simplified model overestimates the motions is preferred to underestimation.

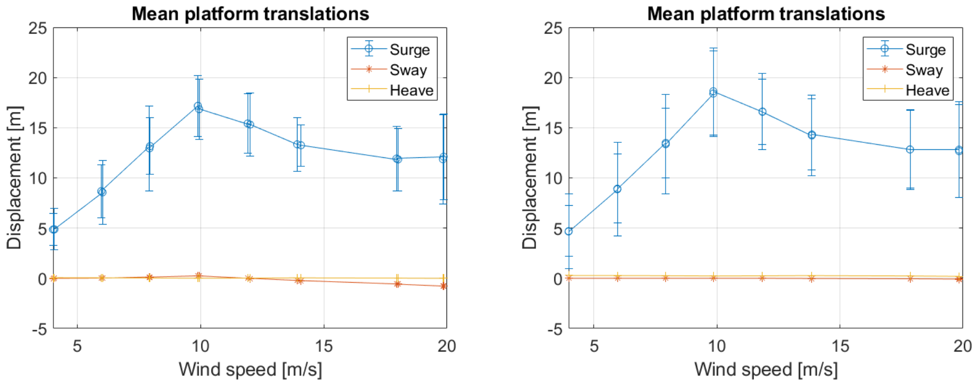

(a) Platform translations on initial model from turbulent wind test.

(b) Platform translations on simplified model from turbulent wind test.

Figure 44: Turbine translations on initial (a) and simplified (b) model from turbulent wind test.

The resulting wind turbine rotations of the initial and the simplified model is shown in Figure 45a and 45b. As was the case for surge, the offset in pitch was also slightly larger on the simplified model, but the pitch curves are similar. The maximum average pitch offset is approximately 4.1 deg on the initial model, and approximately 4.5 deg on the simplified model. The standard deviation shown in the error bars shows that the maximum of the initial model is under 5.5 deg, compared to almost 7 deg in the simplified model. The relatively small offsets in roll and yaw were not taken into consideration in the quadratic wind coefficients and, therefore, resulted in no offset on the simplified model.

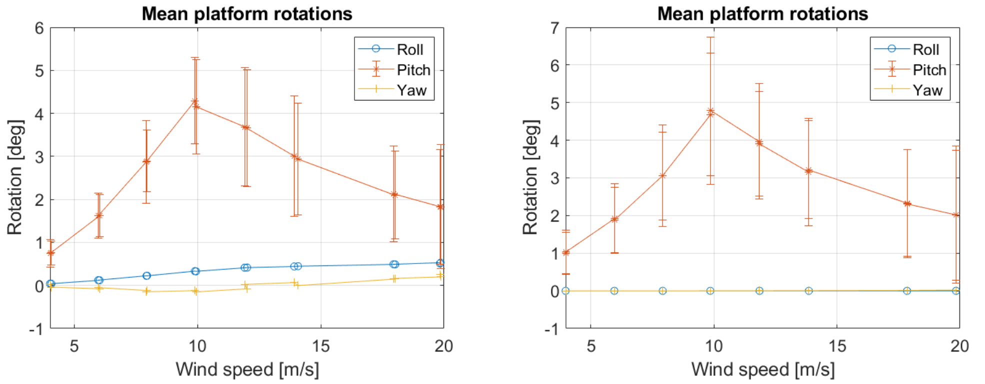

(a) Platform rotations on initial model from turbulent wind test.

(b) Platform rotations on simplified model from turbulent wind test.

Figure 45: Turbine rotations on initial (a) and simplified (b) model from turbulent wind test.

The axial tensions of the mooring lines on both models are shown in Figure 46. Due to the larger offset in surge on the simplified model, *Line 1* has a larger peak at approximately 2700 kN, compared to approximately 2500 kN on the initial model. On the initial model, a difference in the mooring line tension of *Line 2* and *Line 3* can be spotted for the largest wind speeds. This is due to the small offset in roll, shown in Figure 45a, which was not considered in the simplified model. Apart from that, the comparison of the axial mooring line tension on the models is reasonable.

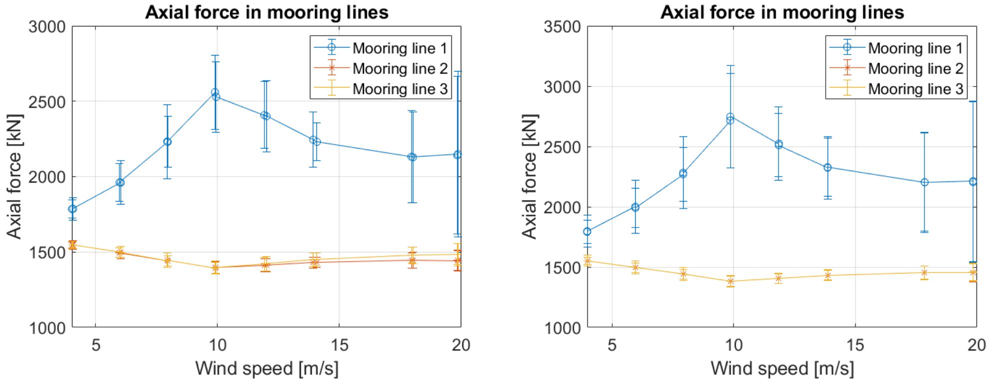

(a) Axial mooring line forces on initial model from turbulent wind test.

(b) Axial mooring line forces on simplified model from turbulent wind test.

Figure 46: Axial mooring line forces on initial (a) and simplified (b) model from turbulent wind test.

As the comparison shows, there are slight differences in the offsets and the mooring lines tension. However, the differences are small, and the simplified model always overestimates the values. Therefore, it was concluded that the quadratic wind coefficients were a valid substitute for the removal of the blades.

The results obtained from the turbulent wind test on the initial model at 130 m water depth will be discussed further in Section 4.5.2. This discussion was used as a basis for the comparison with the results from the turbulent wind test on the designed mooring systems at 700 m.

4.3.2 Reduction of simulation time on park level system

As described in Section 3.3.2, when the park-level system was studied, some modifications, presented in Table 4, were done and the simulation time was reduced by 83.1%. The time step in *SIMA* and the polyester element length were changed, resulting in reduced simulation time. A comparison of the axial tension in the shared mooring line, *Line 3*, from a 1 hour simulation with the initial and the new parameter can be seen in Figure 47. The figure shows that the changing of the parameters had little to no effect on the resulting axial force in the mooring line.

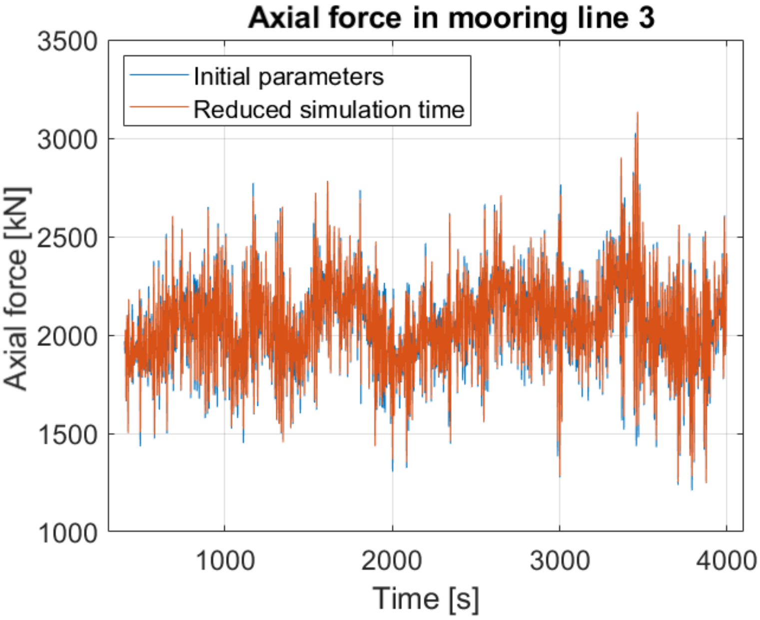

Figure 47: Comparison of long and short simulation time.

A summary of the results obtained from the two simulations and the difference between the results in % can be seen in Table 18. The mean and standard deviations of the surge offsets and the axial tension in the five mooring lines are presented.

	Initial results	New results	Difference in %
Mean surge of platform 1 [m]	15.72	15.95	+1.46
Standard deviation in surge of platform 1 [m]	3.96	4.05	+2.27
Mean surge of platform 2 [m]	58.25	58.86	+1.05
Standard deviation in surge of platform 2 [m]	11.30	11.68	+3.36
Mean tension in mooring line 1 [kN]	3716.3	3726.9	+0.29
Mean tension in mooring line 2 [kN]	2000.2	2003.9	+0.18
Mean tension in mooring line 3 [kN]	2078.6	2081.8	+0.15
Mean tension in mooring line 4 [kN]	624.12	622.70	-0.23
Mean tension in mooring line 5 [kN]	2078.0	2082.1	+0.20

Table 18: Comparison of results with long and short simulation time

The comparison of the results shows a change of less when 0.3% in the axial mooring line tension. However, for the standard deviations of the surge offset, the difference was up to 3.36%. Given the significant reduction of the simulation time and the fact that all values were overestimated, the new parameters were concluded to represent the results acceptably.

4.3.3 Quadratic wind coefficients on the rear wind turbine due to wake deficit

Equation 13 was used to calculate the wind speed experienced by the rear wind turbine, u_1. The thrust curve from the constant wind simulation was recreated in *Excel*, and a trend line was used to estimate the thrust force on the rear wind turbine created by u_1. The plot and the estimated trend line can be seen in Section A in the Appendix. The quadratic wind coefficient on the rear wind turbine, $C_{wind,rear}$, was calculated from Equation 60 with this estimated thrust and the mean wind speed, U_{mean}, for each condition. The results can be seen in Table 19.

U_{mean} [m/s]	u_1 [m/s]	Thrust force from v_1 [N]	Quadratic wind coefficient on rear wind turbine, $C_{wind,rear}$ $[N/m^2]$
4	3.26	0*	-
6	4.89	339768	9438
8	6.52	579392	9053
10	8.15	893000	8930
12	9.78	1280736	8894
14	11.4	1168552	5962
18	14.7	859896	2654
20	17.3	757200	1893

Table 19: Quadratic wind coefficients on rear turbine to account for wake deficit.

*Thrust force = 0 because the wind speed, v_1, is lower than the cut-in wind speed of 4 m/s.

For the wind speed of 3.26 m/s experienced by the rear wind turbine, a quadratic wind coefficient could be calculated to include the drag force from the wind on the parked blades but was neglected in this project as this contribution is assumed to be relatively small.

This estimation leads to the simulated wind speed of 12 m/s resulting in the largest thrust force on the rear turbine. The disturbed wake leads to a wind speed of 9.78 m/s being experienced by the rear turbine, close to the peak of the thrust curve at 10 m/s. However, the wake model used to calculate the disturbed wake was simple and should be studied further. Ideally, the simulated wind speed resulting in a wind speed of 10 m/s on the rear turbine should also be found to simulate the maximum thrust force on this wind turbine.

4.4 ULS - worst case scenario

The designed mooring systems were tested in extreme conditions by a worst case scenario simulated as described in Section 3.5.2. The resulting axial force in the mooring lines was used to calculate the maximum design tension, T_d, with Equation 58. This value was compared to the characteristic capacity of the mooring lines, S_C, calculated with Equation 57, based on the material in the mooring lines.

These tests were performed with the wind speed resulting in the maximum thrust force on the turbines. The 50-year wind speed in the relevant area could be studied and would probably result in a more significant characteristic dynamic tension in the mooring line. However, this wind speed would result in a lower characteristic mean tension because the thrust force would be reduced, and the total design tension is assumed to be lower than the values obtained from these simulations.

4.4.1 Single turbine mooring systems

In Section 3.4.3, the two single turbine mooring systems were described. The design tension, T_d, in *Line 1* of these two systems, was calculated based on the results obtained by the worst case scenario-test and can be seen in Table 20. Both systems had lower design tension than the characteristic tension of the mooring system, passing the test with some margin when both a normal and a high safety factor was used.

	γ_{mean}	γ_{dyn}	System 1	System 2
Normal safety factor	1.3	1.75	$T_d = 5968.7\,\text{kN}$	$T_d = 6486.7\,\text{kN}$
High safety factor	1.5	2.2	$T_d = 8358.8\,\text{kN}$	$T_d = 9024.0\,\text{kN}$
Characteristic capacity	$S_C = 13\,047\,\text{kN}$			

Table 20: Maximum design tension and characteristic capacity of the two single wind turbine systems

No slack line events were observed in the mooring lines during these tests in either of the two systems. However, the test could be performed with environmental forces approaching the models in the opposite direction, which may lead to slack in the single rear mooring line.

The maximum measured horizontal offsets of the mooring systems were 42.8 m and 22.6 m for *System 1* and *System 2*, respectively, way lower than the maximum allowed limits of the power cable.

4.4.2 Shared mooring system

On the park-level mooring system, the environmental forces were simulated to approach the model parallel to *Line 1* and parallel to the shared mooring line, *Line 3*, with and without considering the wake deficit. The results showed that the different angles of attack of the environmental forces did not change the fact that the largest tension was measured in *Line 1*, seen in Figure 34. When the wake deficit was considered, the simulated wind speed resulting in the most significant mooring line force was 12 m/s as this lead to a wind speed of approximately

$10\,\mathrm{m/s}$ being experience by the rear wind turbine, resulting in the largest thrust force.

The results in Table 21 shows that the design tension, T_d, was lower than the characteristic capacity, S_C, in all simulations. The largest mooring line tension was measured when the environmental forces approached the model parallel to *Line 1*. However, when a high safety factor was used, the maximum design tension was measured to 10 123 kN which is approximately 78% of the characteristic capacity of 13 047 kN.

	γ_{mean}	γ_{dyn}	Parallel with Line 1	Parallel with Line 3 Wake deficit considered	Parallel with Line 3 Wake deficit not considered
Normal safety factor	1.3	1.75	$Td = 7299.8\,\mathrm{kN}$	$Td = 6304.2\,\mathrm{kN}$	$Td = 7129.9\,\mathrm{kN}$
High safety factor	1.5	2.2	$Td = 10123\,\mathrm{kN}$	$Td = 8704.0\,\mathrm{kN}$	$Td = 9871.9\,\mathrm{kN}$
Characteristic capacity	$S_C = 13047\,\mathrm{kN}$				

Table 21: Maximum design tension and characteristic capacity of the two turbine system

By studying the resulting minimum tension in the mooring lines, no slack lines were observed in either of the simulations.

The maximum measured offsets in surge and sway were observed on *Turbine 2* when the environmental forces were simulated parallel with *Line 3*, and wake deficit was not considered. The maximum horizontal motion was 82.1 m in sway and 49.4 m in surge. This was larger than for the single turbine mooring systems, but still well within the limits of 175 m and 105 m.

4.5 Initial model at 130 m water depth

4.5.1 Decay test

On the initial model, the decay test was performed in all six rigid body modes. The results from the decay test in surge and sway can be seen in 64. The results show that the natural periods in these directions are approximately equal. The natural period was found to be 186.6 s and 186.3 s in surge and sway, respectively. However, the slight difference is assumed to be due to inaccuracy in the recreated line used to calculated the natural period. These results lead to the conclusion that a decay test was only necessary to perform in one of these two translations on the other single turbine mooring systems.

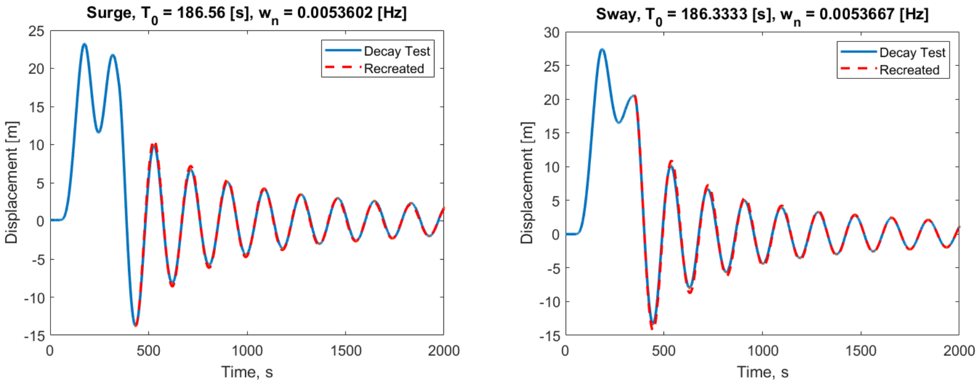

(a) Decay test in surge with recreated line.

(b) Decay test in sway with recreated line.

Figure 48: Decay test in surge (a) and sway (b) on initial model at water depth 130 m

In surge and sway, the recreated lines are reasonable, but the decay test could have been improved. The constant force could have been applied for a longer time to stabilize the model at an offset, and the simulation could have been performed over a longer time-scope. This may have resulted in a different calculated natural period.

The decay test in heave on the initial model is shown in Figure 49. The natural period was calculated to be 20.6 s, which is close to usual wave periods. However, this rigid body mode is minimally affected by the mooring system and mainly decided by the geometrical shape of the semi.

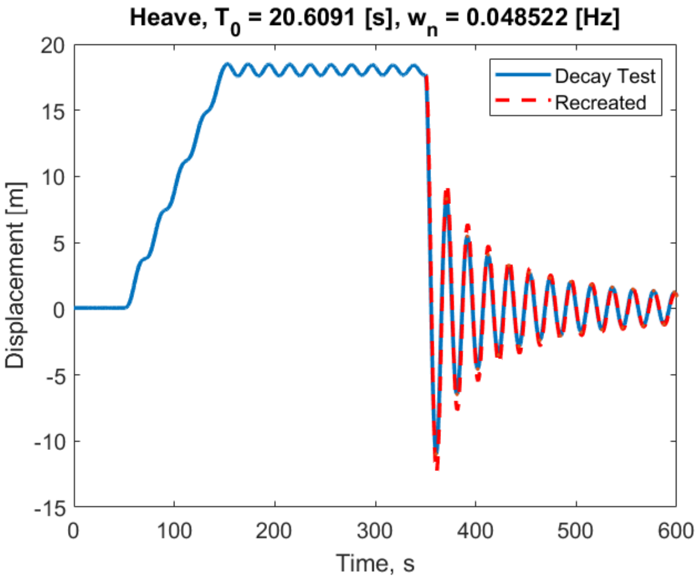

Figure 49: Decay test in heave with recreated line.

The decay test in heave gave good results, and the recreated line seems to fit the measurements right. Therefore, this calculated natural period is assumed to be accurate. There were some oscillations present while the constant force was applied, and these could have interfered with the results. The oscillations are probably due to the significant wave height of 0.001 m. Calmer wave conditions would have been preferred.

Likewise as for surge and sway, the two rotations roll and pitch are compared, seen in Figure 50. The results show that the natural periods were identical and equal to 29.3 s. Based on these results, it was concluded that only one of these rotations were necessary to study on the other systems. These natural periods are also minimally affected by the mooring system and determined by the geometry of the semi.

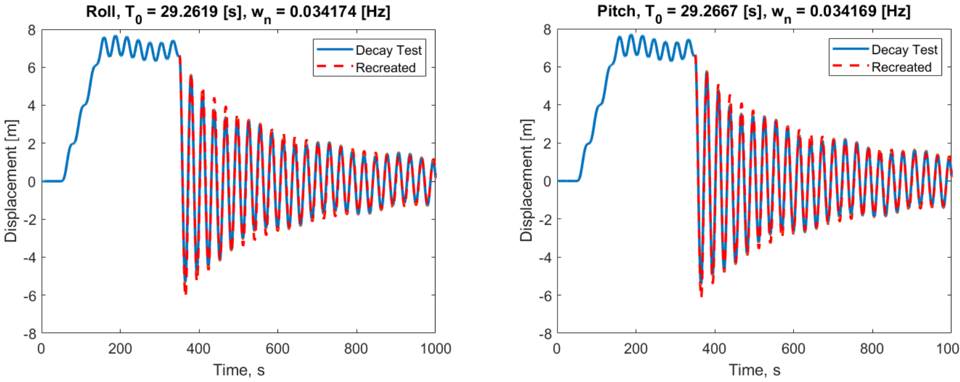

(a) Decay test in roll with recreated line.

(b) Decay test in pitch with recreated line.

Figure 50: Decay test in pitch (a) and roll (b) on initial model at water depth 130 m

In roll and pitch, the recreated line fits the simulation fairly well. There looks to be a second, larger period present in the decay. This second frequency is believed to be the natural frequency in surge, but this should be investigated by a power spectral study.

The natural period in yaw was calculated to 103.6 s, as shown in Figure 51. This rotation, and its natural period, is influenced by the mooring system and had to be carefully studied on the other systems.

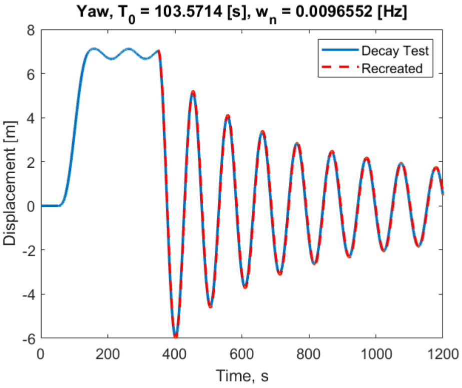

Figure 51: Decay test in yaw with recreated line.

The decay test in yaw resulted in a good fit, but some oscillations can be observed while the constant force was applied. This could have been improved by calmer wave conditions or a force with a longer duration to let the model be in equilibrium before initializing the decay.

4.5.2 Turbulent wind test

The results from the turbulent wind simulation on the initial model at 130 m water depth was presented in Section 4.3.1 and used to validate the simplified model.

The resulting platform translations were shown in Figure 44a. The environmental forces were simulated parallel with *Line 1*, resulting in surge motion being the interesting discussion output parameter. As Figure 44a shows, the surge motion increased with the wind speed, until 10 m/s, where a peak of the mean offset was measured at approximately 17 m. The mean surge offset decreased after 10 m/s, but the standard deviation, shown in the error bars, was at its largest at wind speed 20 m/s. This is believed to be due to the impact from the largest significant wave height of 12 m being the simulated in this condition, as can be seen in Table 15. The relatively large error bars can be explained by the fact that the surge motion is determined by the thrust force, which fluctuates. The lower wind speeds have a more significant turbulence percentage and are more sensitive to turbulence due to their relatively low mean wind speed.

The resulting turbine rotations on the initial model were presented in Figure 45a. The mean offset in pitch peaked at approximately 4 deg at wind speed 10 m/s. The pitch motion is comparable to the results obtained by the constant wind test. The error bars in the pitch motion can be explained by the fact that thrust is the excitation force, and had large fluctuations. The small offset in roll is, as stated in Section 4.2, due to the torque moment created the spinning rotor, and the offset in yaw is a result of the combination of roll and thrust.

The axial tension in the mooring lines can be seen in Figure 46a, and shows how surge and pitch alter the force in the mooring lines. With Figure 30, showing the orientation of the mooring lines, in mind, and the fact that the wind and waves were simulated to approach the model parallel with *Line 1*, these results are reasonable. The curve of the mean mooring line tension followed the surge and pitch motion and reached a maximum in *Line 1*, and a minimum in *Line 2* and *Line 3*, at wind speed 10 m/s. The maximum average tension was approximately 2500 kN in *Line 1*.

4.6 Simplified model at 700 m water depth - mooring system 1

In Section 3.4.3, this mooring line system was referred to as *System 1*, and the details regarding the mooring lines were described there. In this section, the results from the decay tests and the turbulent wind test, outlined in Section 3.5.3 and 3.5.4 respectively, will be presented. From the decay test, the estimated natural periods will be presented and from the turbulent wind test the platform translations and rotation, as well as the axial mooring line tension in different operational conditions, were studied.

4.6.1 Decay test

The results from the decay test with the recreated lines, likewise as for the initial model, can be seen in Section B in the Appendix. The estimated natural frequencies and periods in surge, heave, pitch, and yaw are presented in Table 22.

Rigid body motion	Natural frequency [Hz]	Natural period [s]
Surge	0.00397	252
Heave	0.04857	20.6
Pitch	0.03500	28.6
Yaw	0.00640	156

Table 22: Natural frequencies and periods of designed single turbine mooring *System 1*.

The results show that the natural periods in heave and pitch were unchanged compared to the results from the initial model, seen in Figure 49 and Figure 50b respectively. The natural period in surge and yaw, on the other hand, was different. The natural period in surge was calculated to 252 s compared to 187 s on the initial model, as can be seen in Figure 48a. This was because of the pre-tension of 815 kN in the mooring lines of this system, compared to 1670 kN in the initial system. In addition to the changed geometry and mooring line materials. This also leads to an increased natural period in yaw. On the initial model, as seen in Figure 51, the natural period in yaw was calculated to 104 s.

4.6.2 Turbulent wind test

Platform translations

The offsets in the platform translations at different wind speeds are presented in Figure 52. The mean offset in surge followed the thrust curve and had a peak of approximately 34 m at wind speed 10 m/s. The offset in sway was zero due to the fact that the environmental forces attacked in surge direction. The mean offset in heave was also constant at zero, which proves that the ballast weight, changed by the structural mass of the semi, was adjusted correctly to make the platform float.

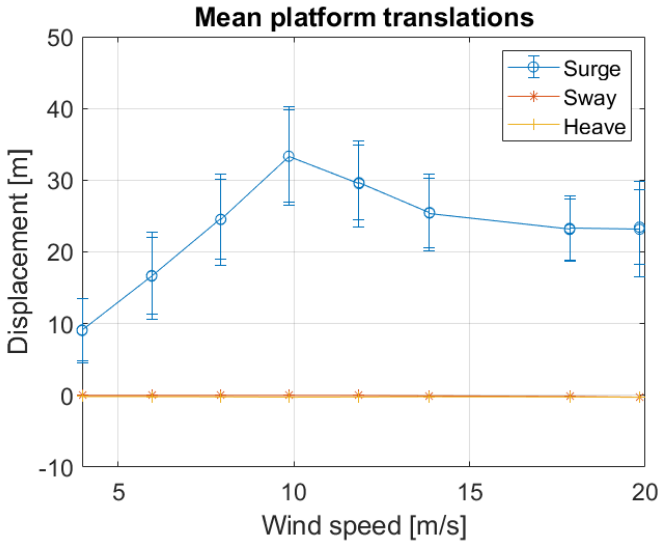

Figure 52: Platform translations of *System 1* from turbulent wind test.

The standard deviations of the surge offset were due to frequencies discovered by studying a spectrum of the surge motion for wind speeds 10 m/s and 20 m/s. At wind speed 10 m/s, the natural frequency in pitch and the wave frequency of 8 s had small contributions, but the dynamic surge offset was mainly due to the natural frequency in surge. When the mean wind speed was 20 m/s, waves with period 15 s were also simulated. This was close to the natural period in heave of 20.6 s and resulted in these two frequencies contributing to the resulting standard deviation. Additionally, wind-induced frequencies proved to have a more significant impact at this larger mean wind speed. Slowly-varying wind speed changes, and the constant quadratic wind coefficient lead to a varying thrust force, hence varying surge offset.

Platform rotations

Likewise as for surge, the mean pitch rotation followed the thrust curve and had a peak at wind speed 10 m/s, equal to approximately 5 deg, seen in Figure 53. The resulting turbine rotations look similar to the results obtained by the turbulent wind test on the simplified model with the initial mooring system, shown in Figure 45b. In addition to the unchanged natural period in pitch and roll, this proves that the mooring system has a minor impact on these rigid body modes. As was described in Section 4.3.1, the relatively small rotation in roll due to the moment created by the rotor torque, was not considered. The absence of roll results in no yaw. However, this rotation is assumed to be larger than the one seen on the initial model because of the lower pre-tension in the mooring lines, their changed geometry, and the increased natural yaw period. Therefore, the zero-value of roll and yaw must be critically reviewed.

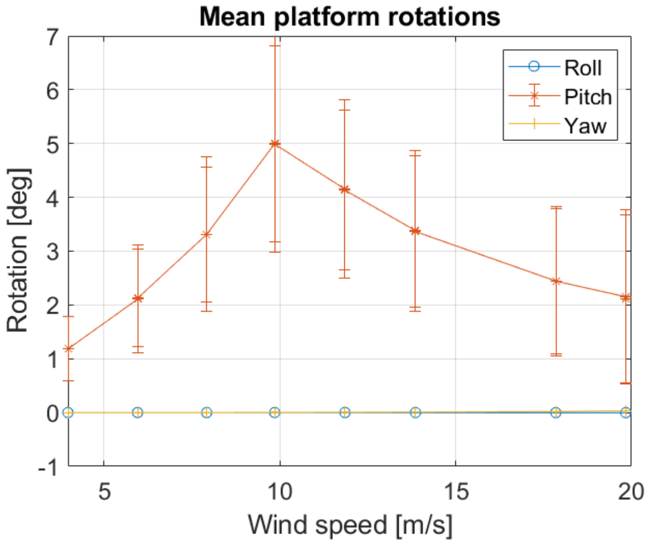

Figure 53: Platform rotations of *System 1* from turbulent wind test.

Mooring line tension

The resulting axial tension of the three mooring lines can be seen in Figure 54. *Line 1* is the most interesting mooring line as it was aligned with the surge direction, where the environmental forces were simulated. Consequently, the axial tension of this line followed the curve of the surge motion. The axial tension peaked at wind speed 10 m/s at a value of approximately 2200 kN. The axial tension in *Line 2* and *Line 3* look almost constant, but their average offsets are decreasing before, have a minimum at, and increases after wind speed 10 m/s. This is due to their orientation, with anchors located behind the initial platform location relative to the approach angle of the environmental forces. The tension in these lines has a minimum of approximately 600 kN. Through a spectral study it was observed that the large standard deviation at the rated wind speed was due to quasi-static wind-induced frequencies. At the larger mean wind speed of 20 m/s, on the other hand, the natural frequency heave, and the nearby wave frequency, were observed as the dominating frequencies.

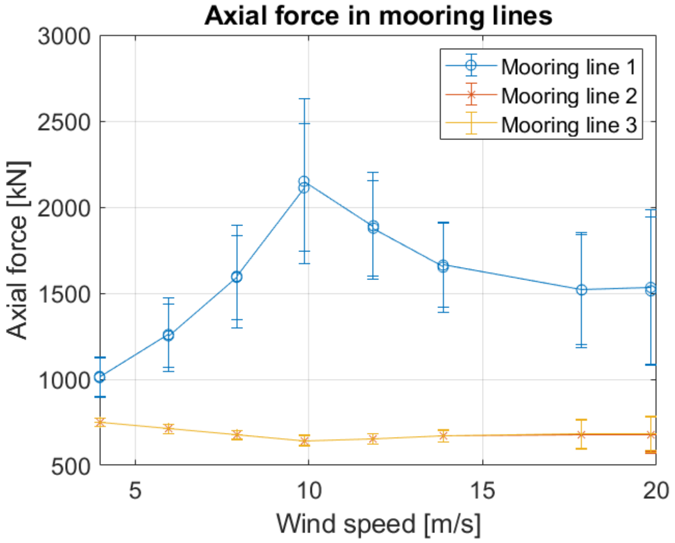

Figure 54: Mooring line tension of *System 1* from turbulent wind test.

The axial mooring lines tension in condition 7 and 15 from Table 15 in Section 3.5.4, with wind speeds 10 m/s and 20 m/s respectively, were studied and the results are presented below.

The frequencies affecting *Line 1* in conditions 7 and 15, are shown in Figure 55. As the results show, for condition 7 with wind speed 10 m/s, the almost single dominating frequency corresponds to a period close to the natural period in surge, estimated to 252 s in Section 4.6.1. There was also observed a smaller peak at a frequency corresponding to a period of 29.3 s, close to the estimated natural period in pitch. For condition 15, in Figure 55b, the power was spread over multiple frequencies. The frequency corresponding to a period of 600 s is assumed to be part of the wind-induced quasi-static frequencies shown as a peak due to the filtering of the specter. The second and third large peaks are observed at frequencies corresponding to the natural period in heave and the wave frequency of this simulation. The fact that the wave frequency affected the mooring line tension more in condition 15 is logical as a larger significant wave height of 12 m was simulated, compared to 3 m in condition 7. Additionally, the wave periods were 8 s in condition 7 and 15 s in condition 15. As the wave frequency gets closer to the natural period in heave, estimated to 20.6 s, it will contribute to larger dynamic variations.

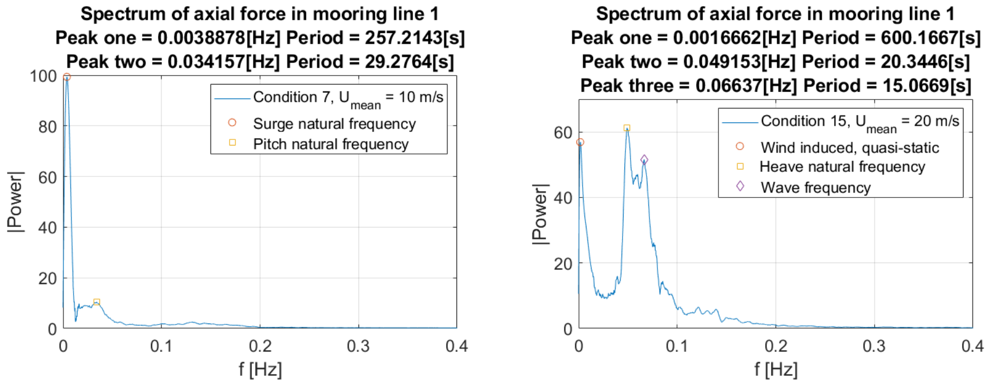

(a) Frequencies in *Line 1* in condition 7. **(b)** Frequencies in *Line 1* in condition 15.

Figure 55: Frequencies in mooring line 1 in condition 7 (a) and condition 15 (b), from turbulent wind test on *System 1*.

An equal frequency study was performed on the results in *Line 2* and *Line 3*. As seen in Figure 54, the tension in these lines were equal, and therefore, only mooring line 2 is presented below. The results from mooring line 3 can be seen in Section C in the Appendix.

The natural frequency in surge was observed for both conditions but was most dominant for condition 7, shown in Figure 56a. The figure also shows that the wave frequency, corresponding to a period of 8 s in condition 7, had a larger impact on these rear mooring lines compared to *Line 1*. An interesting observation in condition 15 was that the natural period in heave, equal to 20 s, was observed as the most dominant frequency.

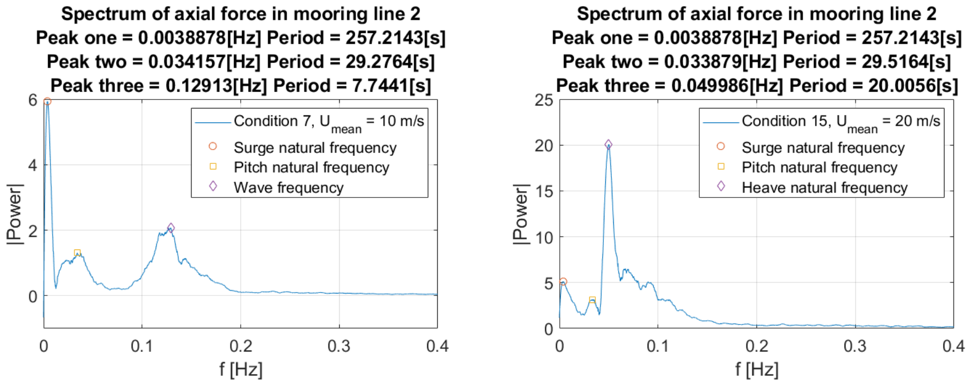

(a) Frequencies in mooring line 2 in condition 7.

(b) Frequencies in mooring line 2 in condition 15.

Figure 56: Frequencies in mooring line 2 in condition 7 (a) and condition 15 (b), from turbulent wind test on *System 1*.

As seen, the natural period in surge had a significant impact on the behavior of the surge motion and the mooring line tension at the rated wind speed in condition 7. At the larger mean wind speed of 20 m/s, the quasi-static frequencies impacted the system. Besides, the simulated wave period of 15 s, with increased significant wave height, compared to condition 7, was closer to the natural period in heave of 20.6 s. Therefore, these frequencies also contributed to the dynamic changes of the system in this condition.

4.7 Simplified model at 700 m water depth - mooring system 2

4.7.1 Decay test

The results showing the measured offsets and the recreated lines used to estimate the natural periods of this mooring system can be seen in Section D in the Appendix. The natural periods in surge, heave, pitch, and yaw are presented in Table 23.

Rigid body motion	Natural frequency [Hz]	Natural period [s]
Surge	0.00557	179
Heave	0.04862	20.6
Pitch	0.03538	28.3
Yaw	0.00918	109

Table 23: Natural frequencies and periods of designed single turbine mooring *System 2*.

The estimated natural periods in pitch and heave were as good as unchanged compared to the ones calculated for the initial model and the other designed mooring system. The natural period in surge of *System 2* was estimated to 179 s, slightly smaller than the initial model which had a natural period in surge of 187 s, seen in Figure 48a. The estimated natural surge period of *System 1* was 252 s, the reason for this difference was the larger pre-tension equal to 1197 kN in this system compared to 815 kN in *System 1*. Additionally, this system had different mooring line configurations, with more significant elastic stiffness. This also lead to the different natural period in yaw equal to 109 s in this system, compared to 156 s in *System 1*. On the initial model, the natural period in yaw was almost identical, equal to 104 s.

4.7.2 Turbulent wind test

Platform translations

The platform translations resulting from the turbulent wind test are presented in Figure 57. The maximum mean offset of approximately 17 m was observed at wind speed 10 m/s, but the maximum measured offset was larger than 20 m. These offsets are similar to the ones obtained from the initial model. This is likely due to the approximately equal natural period in surge of these mooring systems. The natural period in surge was observed to have a significant impact on the surge motion when studying the resulting spectrum at wind speeds 10 m/s and 20 m/s.

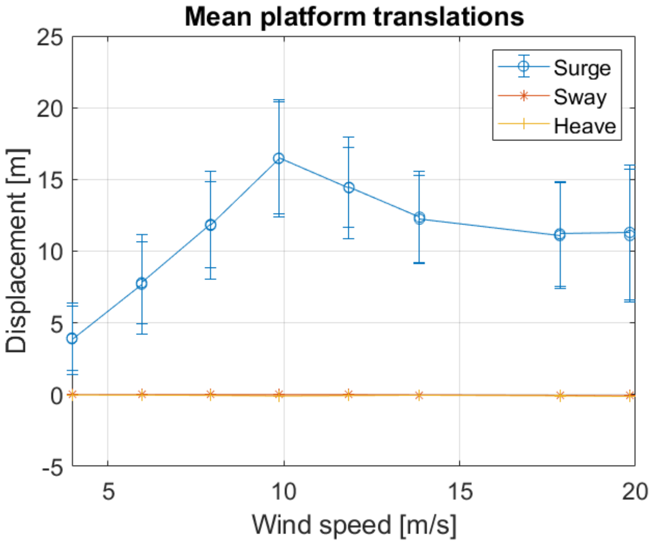

Figure 57: Platform translations of *System 2* from turbulent wind test.

Platform rotations

The resulting platform rotations can be seen in Figure 58. The average pitch offset reached a maximum of approximately 5 deg, while the measured maximum passed 7 deg. These results are similar to the ones from the initial model and *System 1* discussed above. As the natural period in yaw of this system and the initial mooring system were approximately equal, the yaw offset is assumed to be similar to the results obtained by the initial wind turbine.

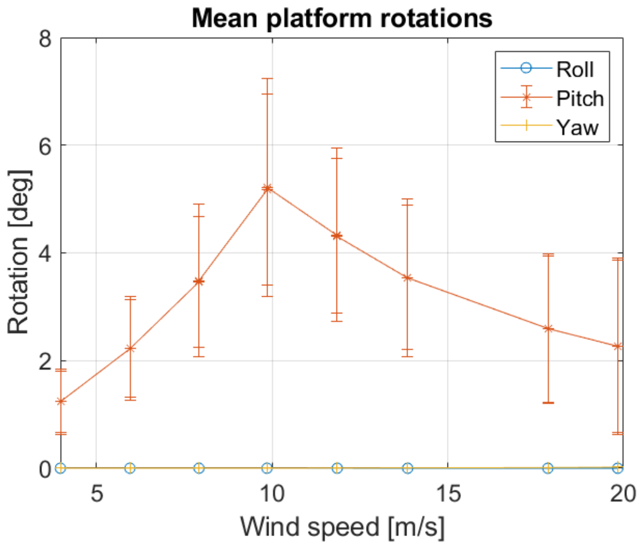

Figure 58: Platform rotations of *System 2* from turbulent wind test.

Mooring line tension

The axial mooring line tension of *System 2* is shown in Figure 59. The mean tension in *Line 1* reached a maximum of approximately 2400 kN, and the maximum measured value was approximately 2800 kN. The average tension in *Line 2* and *Line 3* were equal and nearly constant, but reached a minimum of approximately 900 kN at average wind speed 10 m/s. The minimum measured tension was approximately 850 kN at the mean wind speed of 20 m/s. The standard deviation of the mooring line tension was largest at mean wind speed 20 m/s.

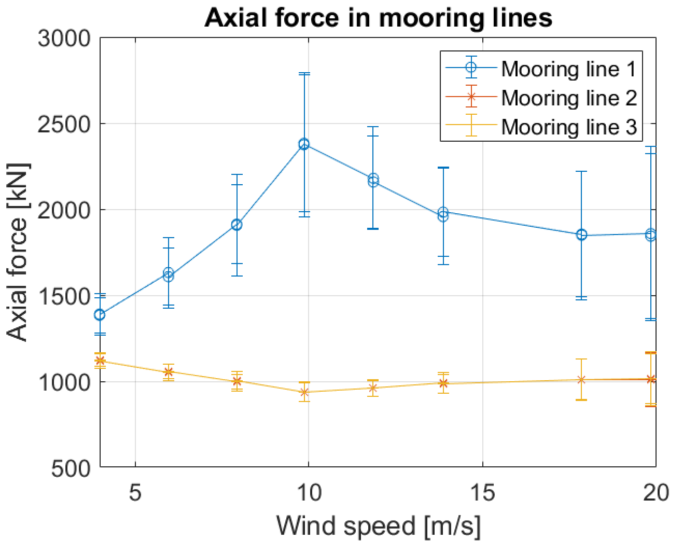

Figure 59: Mooring line tension of *System 2* from turbulent wind test.

The natural period in surge was estimated to 179 s and proved to be vital to the mooring lines tension when their spectrum were studied in condition 7 and 15 from Table 15. The frequency corresponding to this period can be observed in mooring line 1 for both conditions, as seen in Figure 60. In condition 7 with wind speed 10 m/s, significant wave height 3 m, and wave period 8 s, the natural frequency in surge was almost singularly dominating. For condition 15 with mean wind speed 20 m/s, significant wave height 12 m, and wave period 15 s, multiple frequencies contributed to the tension in mooring line 1. The natural frequency in surge, heave, and the wave frequency were identified as the most dominating frequencies. The fact that the natural periods in heave and the wave frequency are relatively close, additionally to the large significant wave height, is the reason for their impact.

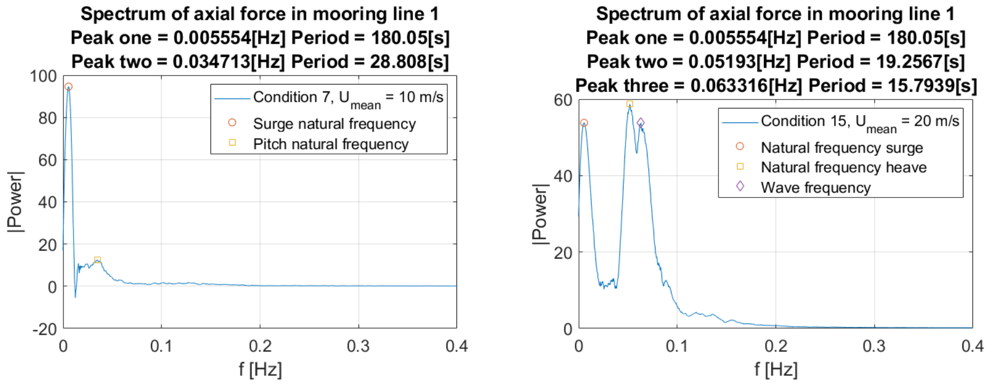

(a) Frequencies in mooring line 1 in condition 7.

(b) Frequencies in mooring line 1 in condition 15.

Figure 60: Frequencies in mooring line 1 in condition 7 (a) and condition 15 (b), from turbulent wind test on *System 2*.

As was the case for *System 1*, the tension in mooring line 2 and 3 were observed to be equal in *System 2* as seen in Figure 59. Therefore, only the results from *Line 2* are presented, and the results from *Line 3* can be seen in Section E in the Appendix. Likewise as in *Line 1*, the natural frequency in surge was the dominating frequency in *Line 2* for condition 7. However, the natural frequency in pitch, and the wave frequency had a larger impact on *Line 2* compared to *Line 1* in this condition. For condition 15, shown in Figure 61b, the natural frequency in surge was also observed, but had a smaller total contribution to the tension than what was observed for condition 7. For condition 15, the natural frequency in heave, and the wave frequency contributed to the changes in the mooring line tension.

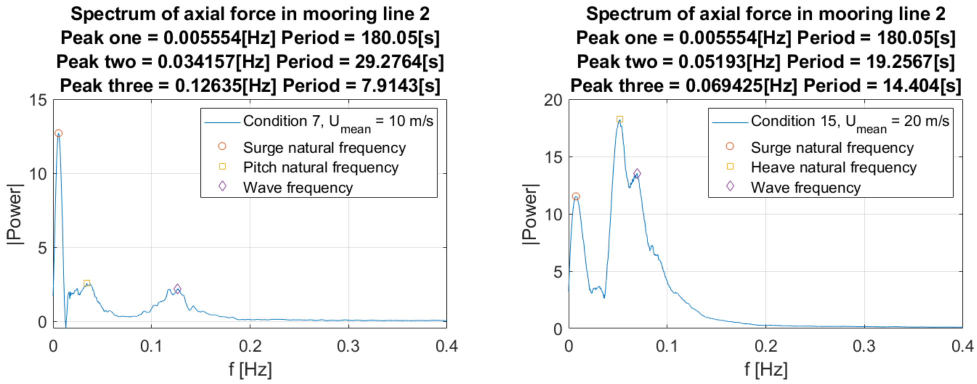

(a) Frequencies in mooring line 2 in condition 7.

(b) Frequencies in mooring line 2 in condition 15.

Figure 61: Frequencies in mooring line 2 in condition 7 (a) and condition 15 (b), from turbulent wind test on *System 2*.

Once again, the importance of the natural frequency in surge can be observed. It is interesting to see that the wind-induced frequencies look to have less impact on this system compared to *System 1*. The reason for this may be the increased pre-tension in the mooring lines with a corresponding lower natural period in surge.

4.8 Comparison of single turbine mooring systems

Some selected results from the simulations of the single turbine mooring systems are summaries in Table 24. The power specter of the mooring lines tension in condition 7 and 15 from Table 15 were studied to clarify which frequencies caused the dynamic variations. In condition 7, with mean wind speed 10 m/s, the systems' respective natural frequency in surge was dominating. In condition 15, a wave frequency close to the natural frequency in heave was simulated. This resulted in these frequencies being domination in the tension of the mooring lines. In *System 1*, the wind-induced frequencies had a larger impact on the tension of the rear mooring lines compared to what was observed in *System 2*.

	System 1	System 2
Pre-tension in mooring lines [kN]	815	1197
Natural period in surge [s]	252	179
Natural period in yaw [s]	156	109
Maximum mean surge offset [m]	34	17
Maximum mean mooring line tension [kN]	2200	2400
Minimum mean mooring line tension [kN]	600	900

Table 24: Comparison of single turbine mooring systems.

The systems had different mooring line configurations, explained in subsubsection 3.4.3, and different pre-tension. This results in the differences seen in the table above. *System 1* had a larger natural period in surge, resulting in a larger maximum average surge offset and lower maximum average mooring line tension. However, the minimum mean mooring line tension is also smaller.

4.9 Park level system with 2 turbines and a shared mooring line

The results from the decay test and turbulent wind test, described in Section 3.5.3 and 3.5.4, respectively, on the system with two turbines and a shared mooring line are described in the following sections. The four bottom-connected mooring lines, two on each turbine, in this system are equal to the ones in *System 2*, but with a larger pre-tension of 1819 kN compared to 1197 kN in *System 2*. The third and final mooring line of the two turbines is shared between them as described in Section 3.4.4 with Figure 35 and 34.

4.9.1 Decay tests

The results from the decay tests in heave, pitch, and yaw are presented in Table 25. These tests were performed equal to the ones on the single turbine systems, but with forces applied on both turbines. The displacements in the respective degree of freedom of *Turbine 1*, and corresponding power specters, used calculated the natural periods, can be seen in Section F in the Appendix. The displacements were equal on *Turbine 2*. Therefore, only the results from *Turbine 1* are presented.

The natural periods in heave and pitch were nearly unchanged from the ones in *System 2*. In heave the natural period in *System 2* was also measured to 20.6 s, while in pitch the natural period was measured to 28.3 s compared to 27.8 s in this system. The estimated natural period in yaw was 82.3 s compared to 109 s in *System 2*. This is due to the larger pre-tension in the bottom-connected lines, and the changed pre-tension, geometry, and contribution from the third shared mooring line's geometric stiffness.

Rigid body motion	Natural frequency [Hz]	Natural period [s]
Heave	0.04860	20.6
Pitch	0.03601	27.8
Yaw	0.01216	82.3

Table 25: Natural frequencies and periods in heave, pitch, and yaw of shared mooring system.

Because of the complexity of this system, and the coupled motions, the results from the decay tests in the horizontal directions are presented in detail. In Section 3.5.3 and Figure 37 these tests were explained. When the horizontal forces were applied parallel to *Line 1* and *Line 5*, the wind turbines were forced to move in the parallel direction of these lines, referred to as *Test 1* in Figure 37. The resulting time series of the surge displacement of *Turbine 1* can be seen in Figure 62a. As the figure shows, multiple decay frequencies were present when the force was released after 650 s. Therefore, a frequency study was performed, and the resulting power specter of the surge displacement can be seen in Figure 62b.

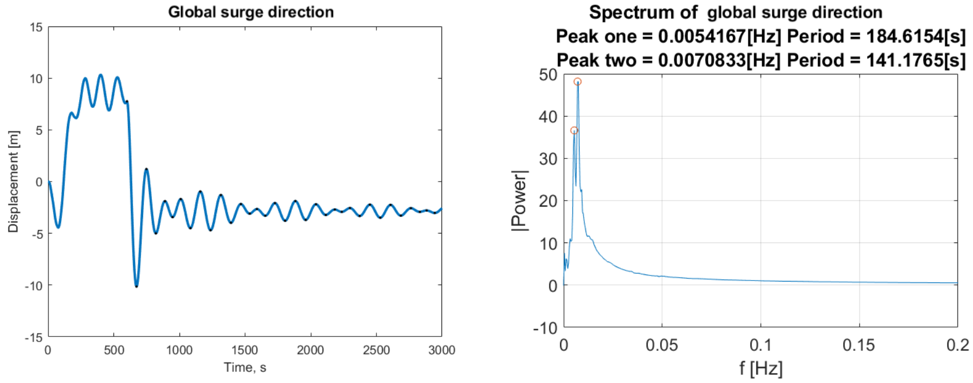

(a) Surge displacement from *Test 1*

(b) Surge decay frequency from *Test 1*

Figure 62: Surge displacement (a) and frequency identification (b) from decay *Test 1* of *Turbine 1* of park level system.

Figure 62b shows that two frequencies corresponding to periods of 184.6 s and 141.2 s contributed most to the decay of the turbine in surge direction. As the frequency corresponding to the period of 141.2 s had the largest peak, this was assumed to be due to mooring *Line 1*. This was also reasonable as the natural period in this direction of *System 2* was estimated to 179 s, and the same mooring line configuration, with a larger pre-tension, was used in this system. The larger pre-tension in the mooring line leads to a stiffer system, hence a shorter natural period. The other significant frequency present in the decay of the turbine in this global direction was due to the shared mooring line.

Test 2 of the horizontal decay tests were performed in the global sway direction on *Turbine 1* with forces were applied 90° to the ones in *Test 1*. The resulting displacement of *Turbine 1* and a power spectral analysis equal to the one above can be seen in Section F in the Appendix. The resulting significant frequencies corresponded to periods of 184.6 s and 141.2 s in this direction as well. The difference from the test presented above was the change in power distribution. The results from *Test 2* showed that the frequency corresponding to a period of 184.6 s had the largest peak.

The final two horizontal decay tests of this system were performed with forces applied parallel to the shared mooring line in *Test 3* and normal to the shared mooring line in *Test 4*. To investigate the displacement of the turbines, a local coordinate system was created, as shown in Figure 63.

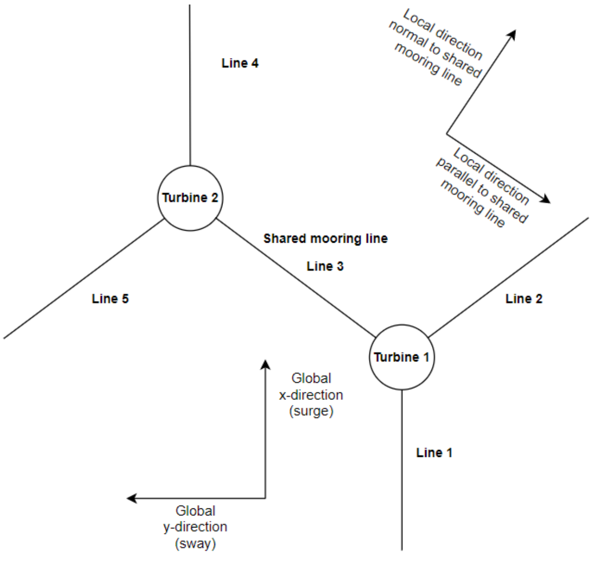

Figure 63: Global and local coordinate system in mooring system with 2 turbines.

The displacement of *Turbine 1* from *Test 3* and its power spectrum can be seen in Section F in the Appendix. The single dominant peak frequency corresponded to a period of 184.6 s, and this was identified as the natural frequency when the turbines moved parallel to the shared mooring line.

The results from *Test 4* showed that *Turbine 1* decayed with a natural period 141.2 s normal to the shared mooring line, also shown in Section F in the Appendix.

The natural frequencies and periods in the horizontal direction of this system is summarized in Table 26.

Horizontal direction	Natural frequency [Hz]	Natural period [s]
Parallel with shared mooring line	0.00542	184.6
Normal to shared mooring line	0.00708	141.2

Table 26: Natural frequencies and periods in the horizontal direction of shared mooring system.

4.9.2 Turbulent wind test

As described in Section 3.5.4, the turbulent wind test was performed three times on the shared mooring system. The first test was performed similarly as on the single turbine systems with environmental forces simulated to approach the model parallel with *Line 1*. Next, the environmental forces were simulated to approach the model parallel with the shared mooring line, *Line 3*. This test was performed both with and without considering the wake deficit. The results from the different turbulent wind simulations are presented and discussed in this section.

Environmental forces parallel with *Line 1*

The turbulent wind test was firstly performed in the global surge direction parallel with *Line 1*, with equal quadratic wind coefficients on both turbines. The disturbance in the wake was estimated, by Equation 60, to be neglectable because of the distance between the turbines and the approach angle of the wind.

Platform translations

The platform translations of the two turbines are presented in Figure 64. The maximum average displacement was approximately 55 m in surge direction experienced by *Turbine 2*, referred to as *Plat2 Surge* in the figure. The maximum surge displacement was approximately 75 m at wind speed 10 m/s. The mean offset in sway of *Turbine 2* was round 30 m, with a maximum of slightly more than 40 m, at wind speed 10 m/s. The offset in sway is assumed to be due to the larger pre-tension in *Line 5* than in the shared mooring line, resulting in a sideways pulling force on the turbine. The resulting offset in surge and sway of *Turbine 1* did not exceed 20 m. However, *Turbine 1* had an offset in the positive global sway direction, even though the pre-tension of *Line 2* was larger than in the shared mooring line. This was due to the surge and sway motion of *Turbine 2*, pulling *Turbine 1* in the positive global sway direction.

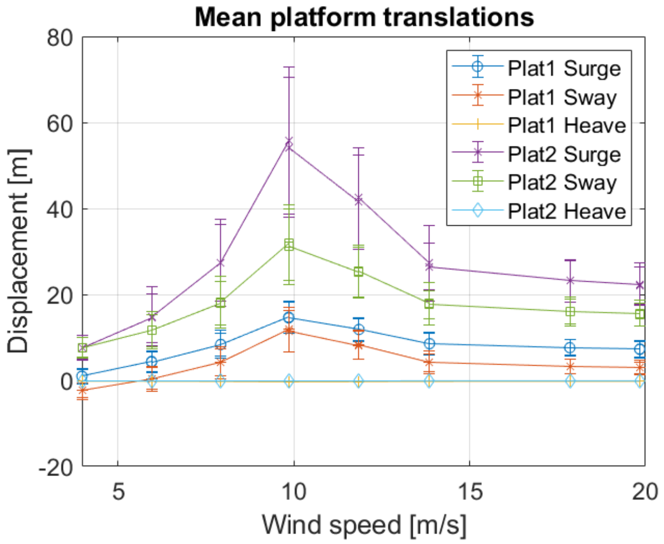

Figure 64: Platform translations of *Turbine 1* and *Turbine 2* from turbulent wind test parallel with *Line 1*.

An interesting observation when comparing these results to the ones of the single turbine mooring systems is the standard deviation of the translations shown in the error bars. For the single mooring systems, the standard deviations were often largest for the highest wind speeds with the largest significant wave height and wave period. However, when studying Figure 64, it can be observed that the standard deviation was largest for the conditions with simulated mean wind speed 10 m/s. By studying the power specter of these conditions, it was observed that this was due to quasi-static wind-induced frequencies. In the conditions with larger wind speed, the natural frequencies parallel to and normal to the shared mooring line contributed more to the motions of the turbines.

Platform rotations

The rotations of the two turbines during the first turbulent wind test are shown in Figure 65. The average rotation in pitch reached a maximum at the average wind speed of 10 m/s for both turbines at a value of approximately 5.5 deg. Pitch reached a maximum of just below 8 deg for *Turbine 2*, and approximately 7 deg on *Turbine 1*. These results are comparable to the results from the tests on the single turbine systems. However, it should be kept in mind that the simplified wind turbine neglected the offset in roll due to the torque moment resulting in no yaw. The natural period in yaw was changed compared to the initial system, and the yaw rotations should be critically reviewed.

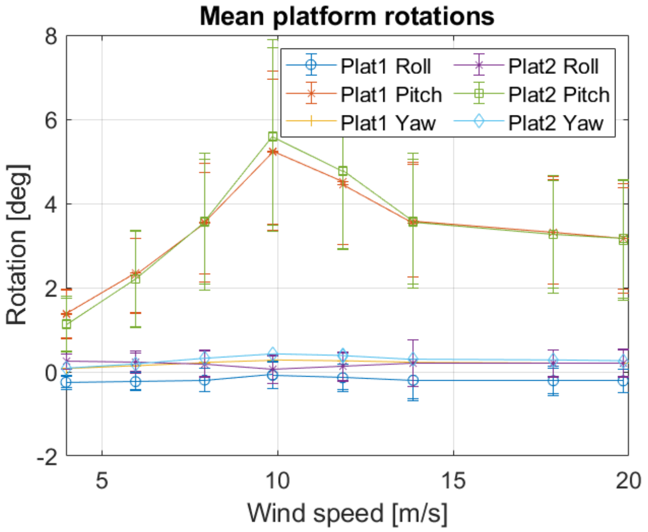

Figure 65: Platform rotations of *Turbine 1* and *Turbine 2* from turbulent wind test parallel with *Line 1*.

Mooring line tension

The resulting tension in the mooring lines can be seen in Figure 66. Even though the largest offset was observed on platform 2, the maximum tension was experienced by *Line 1*. This was due to the orientation of this line, parallel with the environmental forces. The average tension in *Line 1* reached a maximum of approximately 3700 kN. This value is almost double of what was observed for *System 2* with the same mooring line configuration even though the surge offsets are similar. The main difference when comparing with *System 2* is the offset in sway almost equal to the offset in surge on *Turbine 1* in this system, compared to almost zero on *System 2*. This is the reason for the increased mooring line tension of *Line 1*.

The largest average axial force in the shared mooring line was approximately 2100 kN, presented Figure 66. The lowest average tension of approximately 600 kN can be observed in *Line 5* because of the orientation of this mooring line being parallel with the environmental forces, but with the platform moving towards the anchor.

The standard deviation of the line tension, shown in the error bars, is interesting, as it differs from the results in the single turbine systems. The standard deviation was largest at wind speed 10 m/s. This coincides with the observations of the surge motion. On *Turbine 2*, the standard deviation is largest for wind speed 10 m/s in the shared mooring line and *Line 4*. However, in *Line 5*, the standard deviations are largest in the lower wind speed, and smallest at wind speed 10 m/s. The fact that the dynamic variations of the mooring line tension are lower at the lowest mean reduces the risk of snap loads.

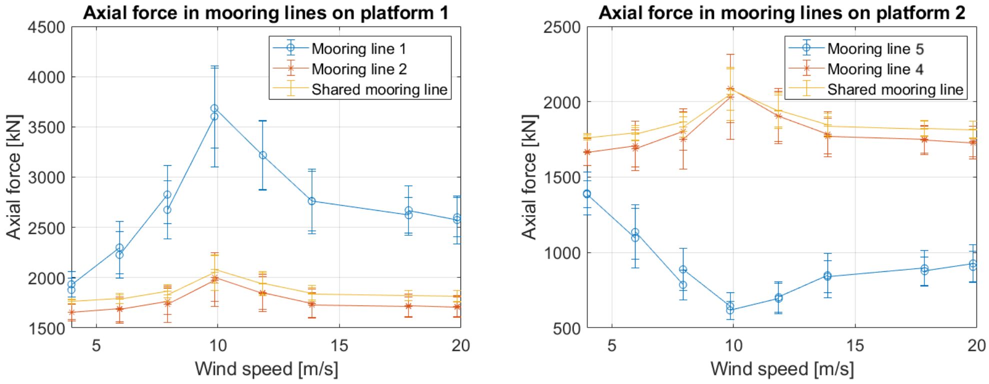

(a) Mooring lines tension on *Turbine 1*   **(b)** Mooring lines tension on *Turbine 2*.

Figure 66: Tension in mooring lines of *Turbine 1* (a) and *Turbine 2* (b) from turbulent wind test parallel with *Line 1*.

For comparison to the single turbine mooring systems, the power spectrum of the mooring lines tension in condition 7 and 15 from Table 15 are presented. Condition 7 had mean wind speed 10 m/s, significant wave height 3 m and wave period 8 s. Condition 15 was simulated with a mean wind speed of 20 m/s, significant wave height 12 m and 15 s wave period.

As can be seen in Figure 67, the quasi-static frequencies impacted the tension of mooring line 1 in these conditions. Additionally, peaks at frequencies corresponding to the natural period parallel with, and normal to, the shared mooring line can be observed in condition 7. For condition 15, the natural frequency normal to the shared mooring line, as well as the natural frequency in pitch and the wave frequency, can be observed to impact the tension of mooring line 1.

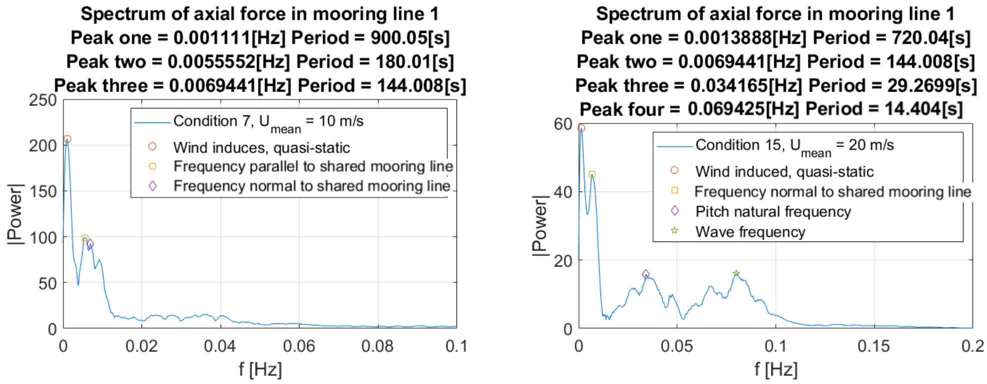

(a) Frequencies in mooring line 1 in condition 7.

(b) Frequencies in mooring line 1 in condition 7.

Figure 67: Frequencies in mooring line 1 from turbulent wind test parallel with *Line 1* in shared mooring line system.

The resulting frequency study of *Line 2* is presented in Figure 68. Condition 7 resulted in a large peak at a quasi-static wind-induced frequency and the natural frequency normal to the shared mooring line. When studying condition 15, three recognizable frequencies can be observed. The fist and highest peak can be observed at a frequency corresponding to the estimated natural period parallel with the shared mooring line. The second and third peaks, with an approximately equal contribution, correspond to periods similar to the natural period in pitch and the wave period.

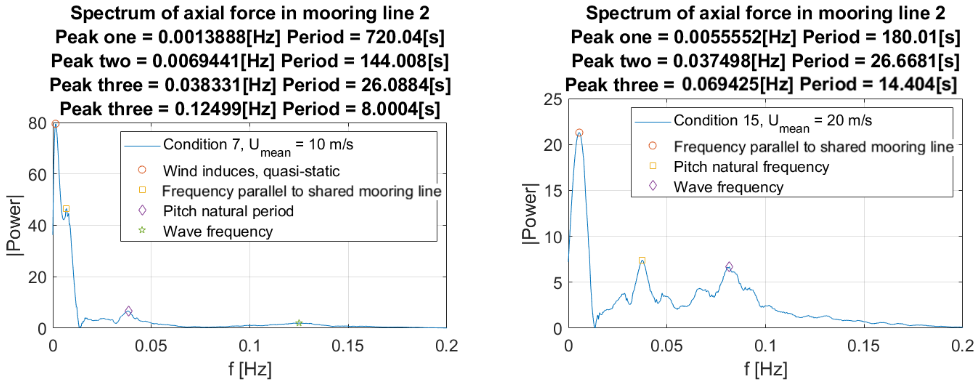

(a) Frequencies in mooring line 2 in condition 7.

(b) Frequencies in mooring line 2 in condition 15.

Figure 68: Frequencies in mooring line 2 from turbulent wind test parallel to *Line 1* in shared mooring line system.

The study of the frequencies affecting the tension of the shared mooring line resulted in Figure 69. At the mean wind speed of 10 m/s, a frequency corresponding to quasi-static wind was the almost single influencing frequency. For condition 15, on the other hand, the wave frequency was observed to have a more significant impact on the tension in the mooring line. However, also for this condition, a frequency corresponding to a large period due to quasi-static wind resulted in the highest peak.

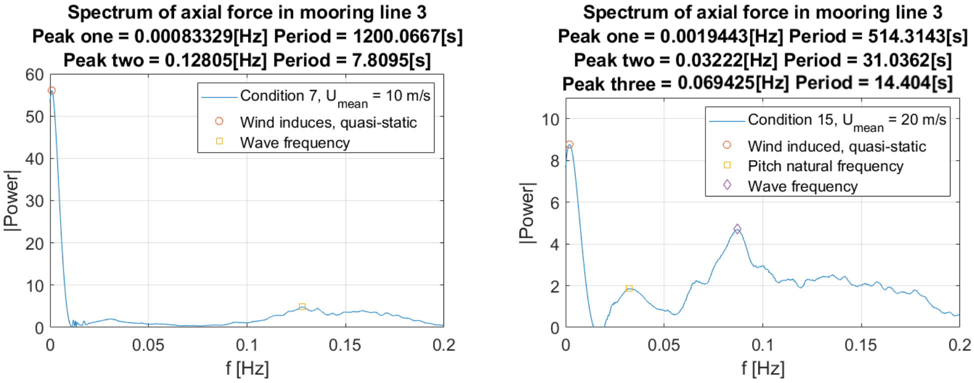

(a) Frequencies in mooring line 3 in condition 7.

(b) Frequencies in mooring line 3 in condition 15.

Figure 69: Frequencies in mooring line 3 from turbulent wind test parallel to *Line 1* in shared mooring line system.

The tension in mooring line 4 was, as seen in Figure 66, almost identical to the results in *Line 2*. Therefore, the frequency study was similar and can be seen in Section G in the Appendix.

The frequencies impacting the tension of *Line 5* are presented in Figure 70. Quasi-static wind frequencies and the natural frequency normal to the shared mooring line can be observed at wind speed 10 m/s. For condition 15, the largest peak is observed at a frequency corresponding to the natural period parallel to the shared mooring line. Peaks were also observed at the natural frequency in pitch and the wave frequency.

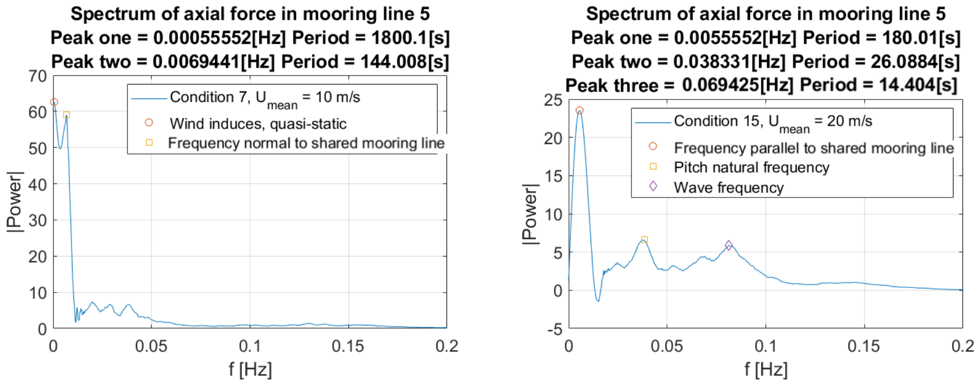

(a) Frequencies in mooring line 5 in condition 7.

(b) Frequencies in mooring line in condition 15.

Figure 70: Frequencies in mooring line 5 from turbulent wind test parallel to *Line 1* in shared mooring line system.

The dynamics of this system when the environmental forces approached parallel with *Line 1* was affected mainly by the quasi-static changes of the mean wind speed. In *System 2*, with the same mooring line configuration as the bottom-connected mooring lines of this system, the natural frequency in surge was the main reason for the dynamic changes. This coupled system, with multiple horizontal natural frequencies and different pre-tension in the mooring lines, resulted in the wind, hence the thrust force, causing the turbines to have large motions. A change of the thrust force on one or both turbines, resulted in significant changes of the horizontal motions, hence the mooring lines tension, on both turbines.

It should be noted that the coupled motions, in addition to the difference in pre-tension of the bottom-connected mooring lines and the shared mooring line, caused larger horizontal motions compared to the single turbine systems. The reason for this designed difference was observed when the large motions of the rear turbine caused *Turbine 1* to get an offset in the positive global sway direction. At the lower wind speed, with smaller offsets of *Turbine 2*, the larger pre-tension in *Line 2* compared to the shared mooring line, caused *Turbine 1* to have a negative offset in the global sway direction.

Environmental forces parallel with the shared mooring line

The turbulent wind test was also performed with environmental forces attacking parallel with the shared mooring line, *Line 3*. This simulation was performed with modified quadratic wind coefficients on the rear turbine, as described in Section

3.5.4. The quadratic wind coefficients of the rear turbine, *Turbine 2*, were changed to the values estimated in Section 4.3.3. This was done to simulated a realistic, disturbed wake approaching the rear turbine.

Platform translations

The resulting platform translations can be seen in Figure 71. As can be seen, the largest average offset occurred at wind speed 12 m/s, in sway direction, and was approximately 65 m for *Turbine 2*. This was due to the approach angle of the environmental forces and the wake deficit, resulting in a near rated wind speed experienced by *Turbine 2* when the simulated wind speed was 12 m/s. The relatively large standard deviation shows an offset of up to 75 m in sway of *Turbine 2*. In the global surge direction, the resulting maximum average offset of platform 2 was nearly 40 m. The standard deviation of the offsets are observed to be largest for wind speeds 10 m/s, 12 m/s, and 14 m/s.

Event though *Turbine 1* had initial quadratic wind coefficients, meaning the maximum thrust force occurred at simulated wind speed 10 m/s, the mean offset in surge and sway direction were larger at wind speed 12 m/s. This was due to the large offset of *Turbine 2*, resulting in a pulling force in the shared mooring line, *Line 3*, and increasing the mean offset of *Turbine 1*. The largest average offset of platform 1 was approximately 25 m, compared to approximately 15 m when the environmental forces were simulated parallel with *Line 1*.

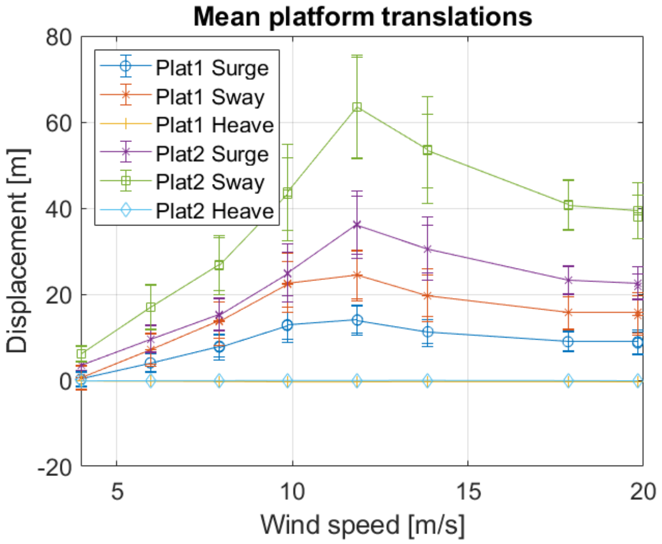

Figure 71: Platform translations of *Turbine 1* and *Turbine 2* from turbulent wind test parallel with *Line 3*.

Platform rotations

As was explained above, the wake deficit results in a maximum thrust force experienced by *Turbine 2* when the simulated wind speed was 12 m/s, this can be observed in Figure 72. The approach angle of the simulated wind results in a thrust force on the turbines parallel with *Line 3*. This is the reason for the offset in both roll and pitch on the two turbines. The maximum average pitch angle was 3 deg, and −4 deg in roll, resulting in a rotation of approximately 5 deg around the axis normal to the shared mooring line in the local coordinate system shown in Figure 63. This value is equal to the resulting pitch rotation from the test with wind simulated parallel with *Line 1*. Due to different wind coefficients on the turbines the peaks are observed at 10 m/s on *Turbine 1*, and 12 m/s on *Turbine 2*.

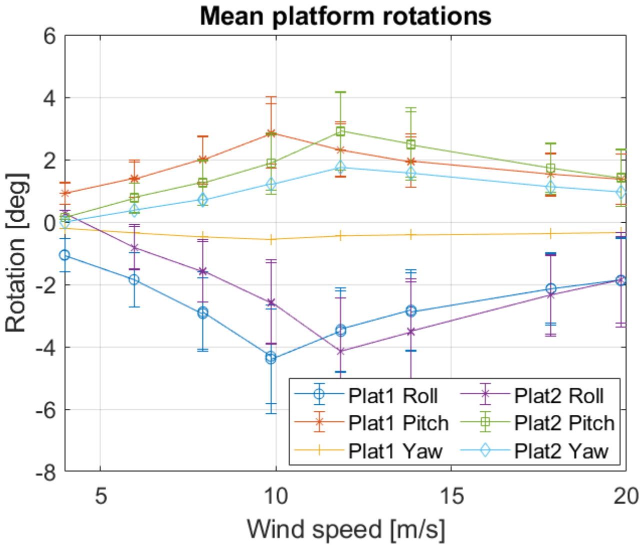

Figure 72: Platform rotations of *Turbine 1* and *Turbine 2* from turbulent wind test parallel with *Line 3*.

The standard deviations are observed to be smaller than when the wind was simulated parallel with *Line 1*. However, when studying the rotations with respect to the local coordinate system, the resulting values of the average offset and the standard deviations were equal.

Once again, it should be noted that the simplified wind turbine neglected the offset created by the torque moment, and the yaw motions should be critically reviewed.

Mooring line tension

Figure 73 shows the resulting tension in the mooring lines. As can be observed the resulting tension in *Line 1* and *Line 2* were equal, this was also the case for *Line 4* and *Line 5*. This is due to the symmetry of the system parallel with the shared mooring line where the environmental forces were simulated.

As was observed above, even though the largest thrust force on *Turbine 1* occurred at wind speed 10 m/s, its maximum surge and sway offsets were largest at wind speed 12 m/s. This is the reason for the largest mean tension of approximately 3300 kN in *Line 1* and *Line 2* at wind speed 12 m/s seen in Figure 73a. Their average tension at wind speed 10 m/s were approximately 3200 kN. The largest standard deviations are observed at wind speeds 10 m/s, 12 m/s, 14 m/s, and 20 m/s. The maximum mean tension of the shared mooring line was approximately 2300 kN at wind speed 12 m/s

The mooring lines of *Turbie 2*, had extrema when the simulated wind speed was 12 m/s as shown in Figure 73b. This was, as already stated, due to the changed coefficients on the rear turbine. The minimum average tension were observed in *Line 4* and *Line 5* equal to approximately 700 kN. As was also observed in the results from the turbulent wind test with environmental forces parallel to *Line 1*, there were small dynamic variations of the minimum measured tension. The standard deviations were larger in *Line 4* and *Line 5* at the larger wind speeds, where also the significant wave height and the wave period were larger. The standard deviations of the shared mooring line were largest at the highest simulated wind speed, as seen in both figures.

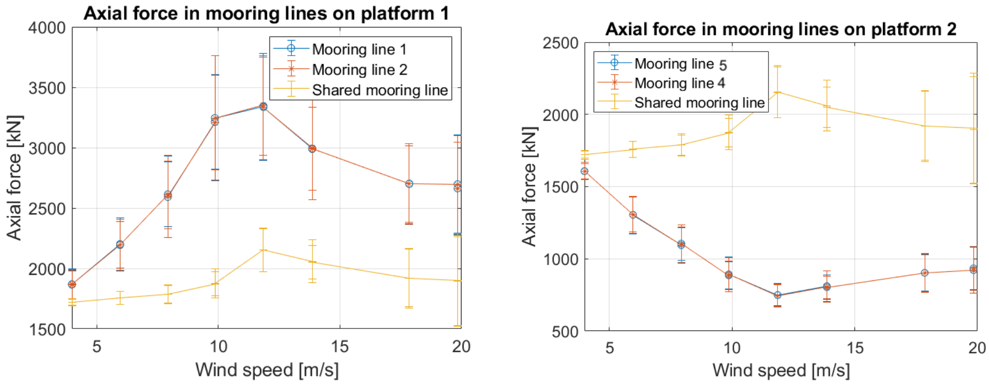

(a) Mooring lines tension on *Turbine 1*.

(b) Mooring lines tension on *Turbine 2*.

Figure 73: Tension in mooring lines of *Turbine 1* (a) and *Turbine 2* (b) from turbulent wind test parallel with *Line 3*.

The spectra of the tension in *Line 1*, *Line 4*, and the shared mooring line are presented below. For comparison with the other systems and the other turbulent with test on this system, conditions 7 and 15 from Table 15 are presented. The spectrum of the tension in *Line 2* and *Line 5* can be seen in Section G in the Appendix.

In mooring line 1, quasi-static frequencies were observed in condition 7. However, the natural frequency normal to the shared mooring line had an approximately likewise impact on the tension. For condition 15, the natural period parallel with the shared mooring line and the natural frequency in heave had the most significant impact. The wave frequency, close to the natural period in heave, also impacted the tension of this mooring line.

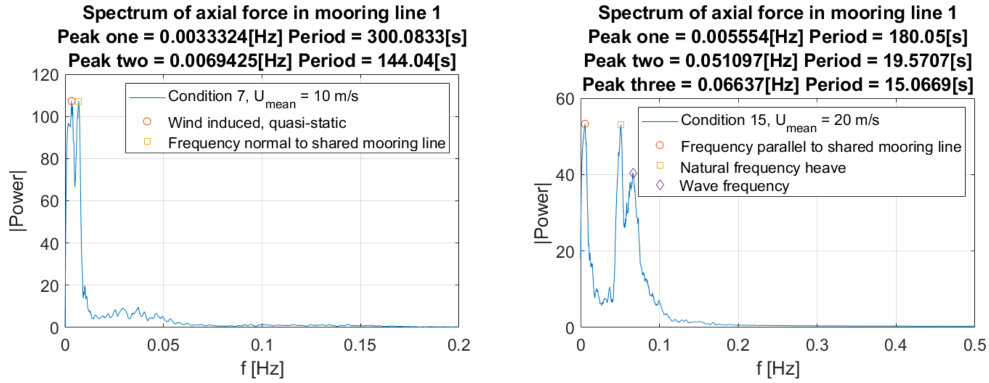

(a) Frequencies in mooring line 1 in condition 7.

(b) Frequencies in mooring line 1 in condition 15.

Figure 74: Frequencies in mooring line 1 from turbulent wind test parallel to *Line 3* in shared mooring line system, considering wake deficit.

In the shared mooring line, the wave frequency had a significant impact, especially in condition 15, as seen in Figure 75b. Besides, the nearby natural frequency in heave was domination for condition 15. For condition 7, there can be observed contributions from a wind-induced frequency and the frequency corresponding to the natural period normal to the shared mooring line.

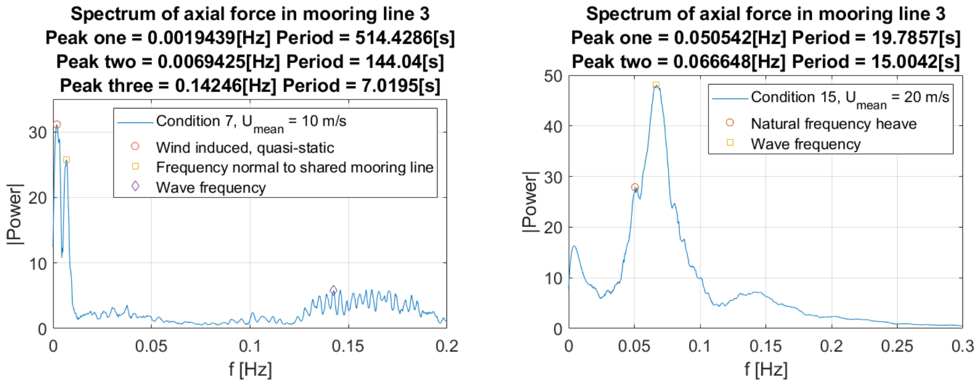

(a) Frequencies in mooring line 3 in condition 7.

(b) Frequencies in mooring line 3 in condition 15.

Figure 75: Frequencies in mooring line 3 from turbulent wind test parallel to *Line 3* in shared mooring line system, considering wake deficit.

In mooring line 4, wind-induced frequencies were dominating for condition 7 and were also important in condition 15. In condition 7 another peak at the natural frequency parallel with the shared mooring line was observed, while the natural heave and wave frequencies were critical in condition 15.

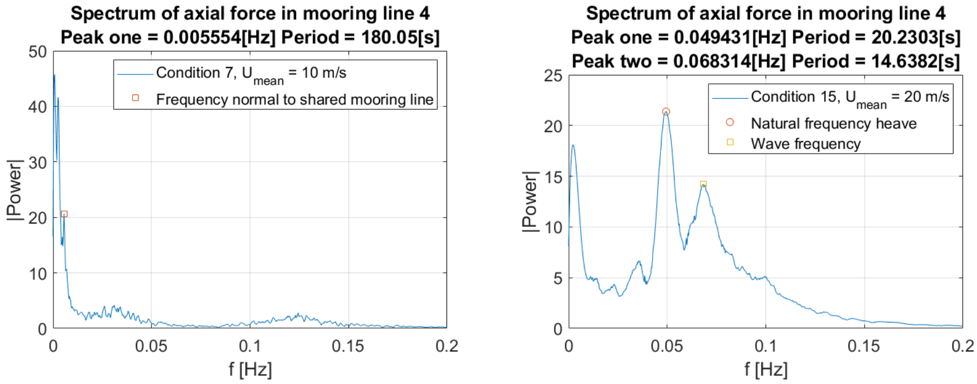

(a) Frequencies in mooring line 4 in condition 7.

(b) Frequencies in mooring line 4 in condition 15.

Figure 76: Frequencies in mooring line 4 from turbulent wind test parallel to *Line 3* in shared mooring line system, considering wake deficit.

These results are compared to the results from the turbulent wind test on this system with environmental forces simulated in the global surge direction. As can be observed, this test leads to the largest average horizontal offset of a turbine at approximately 65 m, compared to approximately 55 m in the other test. However, the maximum average mooring line tension was only around 3300 kN in this test, compared to approximately 3700 kN observed in the first test. This was due to the orientation of the mooring lines with respect to the environmental forces.

The dynamic variations of the offsets and the mooring lines tension were observed to be due to the natural frequency parallel with the shared mooring line, in addition to significant contributions from the wind-induced frequencies and the wave frequency. This was the case for both turbulent wind tests.

Environmental forces parallel with the shared mooring line, wake deficit not considered

As a comparison to the results presented above, this turbulent wind test was simulated without changing the quadratic wind coefficients on the rear turbine. These results would apply if the distance between the turbines were large enough for the wake deficit to not interfere with the wind speed experienced by the rear turbine. Therefore, these results are for comparison only and are inaccurate for the designed system. The translations, rotations and mooring line tensions in Figure 71, 72, and 73 respectively, are compared to the results below.

Turbine translations

As Figure 77 shows, the maximum average offsets in surge and sway of both turbines were experienced at the wind speed of 10 m/s. However, the quantities are relatively equal to the ones observed at wind speed 12 m/s when wake deficit was considered. The maximum mean offsets were 65 m on *Turbine 2* in sway direction.

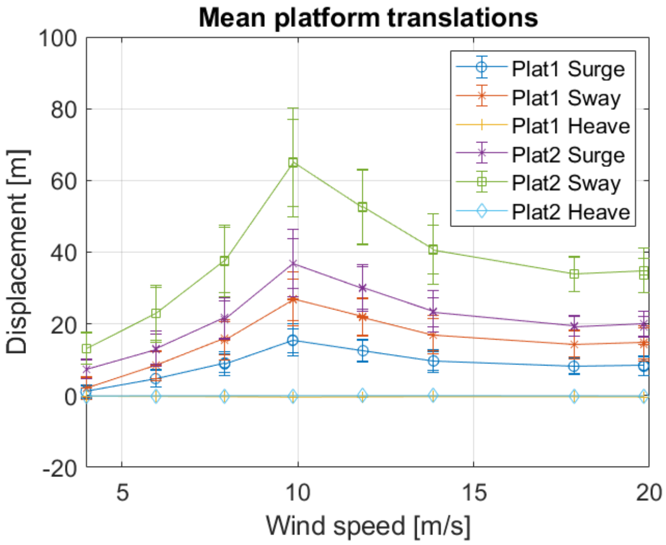

Figure 77: Platform translations of *Turbine 1* and *Turbine 2* from turbulent wind test parallel with *Line 3*, not considering wake deficit.

Turbine rotations

Likewise as for the translations, the resulting platform rotations were equal in magnitude to the ones obtained when considering wake deficit, but were observed at different simulated wind speeds. The rotations of *Turbine 1* are equal to the other test because the quadratic wind coefficients on this turbine were unchanged. The rotations of *Turbine 2* are similar in quantity, but were observed at wind speed 10 m/s in this simulation, compared to 12 m/s in the previous simulation. This was due to the different wind coefficients on the rear turbine.

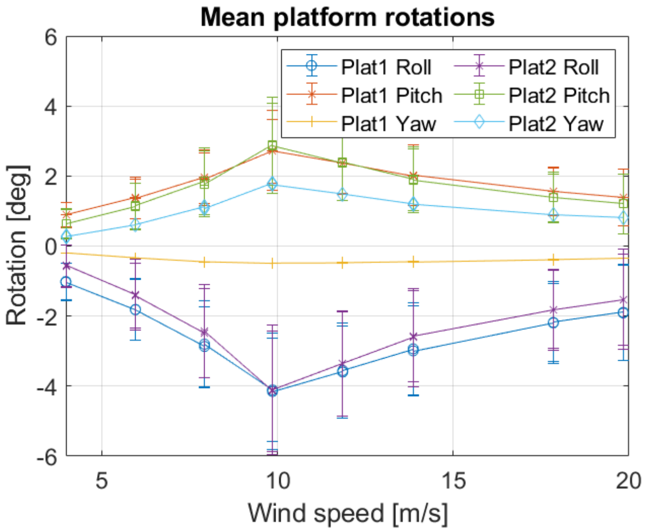

Figure 78: Platform rotations of *Turbine 1* and *Turbine 2* from turbulent wind test parallel with *Line 3*, not considering wake deficit.

Mooring line tension

The axial force in the mooring lines from this turbulent wind test is presented in Figure 79. Due to the largest mean offset in surge at wind speed 10 m/s, the largest tensions in *Line 1* and *Line 2* were also observed at this wind speed. The maximum average tensions in the lines were approximately 3500 kN, larger than 3300 kN when the wake deficit was considered. The mean tension in the shared mooring line was approximately 2200 kN at wind speed 10 m/s. At wind speed 12 m/s in the simulation considering wake deficit, the mean tension of the shared mooring line was 2300 kN because of the larger wind coefficient on the rear turbine, increasing the distance between the turbines. The minimum average tensions of approximately 700 kN were observed in *Line 4* and *Line 5* at wind speed 10 m/s. The minimum average was 700 kN in the previous simulation as well, but occurred at wind speed 12 m/s.

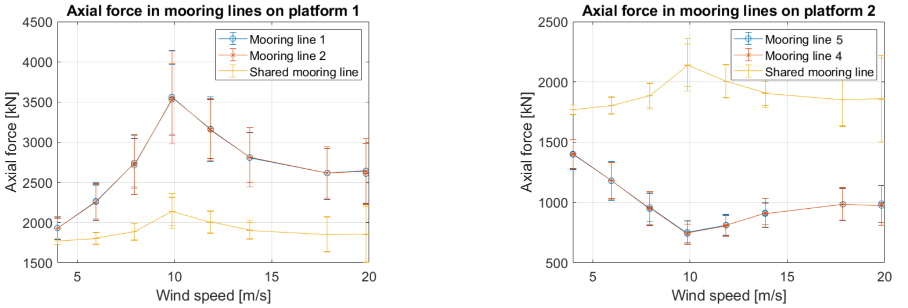

(a) Mooring line tension on *Turbine 1*.

(b) Mooring line tension on *Turbine 2*.

Figure 79: Tension in mooring lines of *Turbine 1* (a) and *Turbine 2* (b) from turbulent wind test parallel with *Line 3*, not considering wake deficit.

As can be observed, the results from the simulation with and without considering wake deficit are relatively equal in quantity but appear at different simulated wind speeds. The maximum mean offsets in the global coordinate system were approximately 65 m in both simulations. This offset was observed in the rear wind turbine and was determined by its experienced wind speed.

The difference in the maximum average mooring line tension may be because the simulated wind speed of 12 m/s resulted in an estimated wind speed of 9.78 m/s experienced by the rear wind turbine, in the previous test. From the constant wind test, it was observed that the simulated wind speed of 10 m/s resulted in the maximum thrust force. If the wind speed resulting in 10 m/s being experienced by the rear turbine had been simulated, it is reasonable to assume that the resulting mooring line tension would be equal to the one observed in this simulation. It should also be noted that when wake deficit was considered, the average mooring line tension was relatively large at wind speed 10 m/s and 12 m/s, compared to only at 10 m/s in this simulation.

5 Conclusion

Mooring systems for floating offshore wind turbines at 700 m water depth has been suggested in this thesis. The mooring systems' effect on the motions of a floating offshore wind turbine has been studied through multiple simulations within the turbines operational. The environmental conditions in these simulations were based on metocean data from an observation site outside the coast of California.

The floating substructure used in this thesis was the model *OO-Star Wind Floater* developed by *Dr.techn Olav Olsen*. A model of this floater, with the *DTU 10 MW Reference Wind Turbine*, was initially used. Simulations of this model were performed in the computer software *SIMA*. Due to computational restraints, a simplified turbine model was developed and compared to the initial one. The comparison between the turbines translations, rotations, and the mooring lines tension showed similar results, and the simplified model overestimated the slight differences.

Two mooring systems of a single wind turbine were designed and compared. Afterward, a mooring system with a shared mooring line between two wind turbines was developed. The natural periods of the designed mooring systems were identified by performing decay tests. The systems were simulated in operational conditions with turbulent winds, in addition to an ultimate limit state test in extreme conditions. The ultimate limit state test was outlined according to standards from *DNV GL* with respect to the environmental conditions in the area of interest.

Some challenges regarding deep water mooring were observed. Long mooring lines were required, and handling of these may be challenging. However, the total cost of these mooring systems was estimated to be reduces compared to the all chain mooring system of the initial model at 130 m water depth. The reason for this was the polyester used as the mooring line material. The shared mooring line also reduced the total cost per turbine, by approximately 10%. Another challenge regarding waves' impact on the tension of the mooring lines, was observed. The natural period in heave, of the model used in this project, was close to typical wave frequencies. This caused dynamic changes in the mooring line tension because of the natural frequency in heave and the wave frequency.

The mooring lines of the single turbine systems passed the ultimate limit state test with a normal and a high safety factor, and their horizontal motions were within the limitations of the power cable. Differences in the two single turbine mooring systems were observed due to different mooring line configurations and pre-tension. The system with a lower mooring line pre-tension had a longer natural period in surge. This resulted in larger horizontal motions and corresponding lower minimum mean tension of the rear mooring lines. The natural period in surge was observed to have a significant impact on the dynamic changes of the tension in the mooring lines. The maximum mean mooring line tension was observed in the system with the largest pre-tension.

For the park-level system, the pre-tension of the mooring lines was challenging to design. The pre-tension in the shared mooring line and the bottom-connected mooring lines should be equal to reduce the horizontal motions of the rear turbine. On the foremost wind turbine, on the other hand, the bottom-connected lines should have a larger pre-tension than the shared one because the rear turbine will pull the foremost turbine sideways when the thrust force causes the rear turbine to move. Still, all bottom-connected mooring lines must be equal to maintain the symmetry in the system because the environmental forces can approach from all angles. The park-level system designed in this project had larger horizontal offsets and mooring line tensions than the single turbine mooring systems. However, the system passed the ultimate limit state test with both a normal and a high safety factor, and the horizontal offsets were within the design limits. Wind-induced frequencies were observed to have a more significant impact on the tension of the mooring lines in the shared system, compared to the results of the single turbine systems.

The importance of the wake deficit when designing a wind turbine park's mooring system was observed through simulations. The park level system was simulated with environmental forces parallel to the shared mooring line, aligning the wind turbines relative to the wind. The wake deficit was estimated and accounted for by changing the wind coefficients on the rear turbine. The resulting maximum thrust force was experienced by the rear wind turbine when the simulated wind speed was $12\,\mathrm{m/s}$, compared to a maximum thrust force on the foremost turbine at simulated wind speed $10\,\mathrm{m/s}$. The consideration of the wake deficit resulted in a lower maximum mooring line tension being observed. However, a wider range of wind speeds caused large mooring line tensions.

5.1 Further work

Regarding the results obtained in this project, modifications and improvements can be made in the future. Firstly, updated metocean data from the area of interest could be studied, as there may have been changes in the environmental conditions during the latest years.

The impact of current was not studied, nor included in the simulations of this project. This would result in larger offsets and mooring line tensions of the systems and should be inspected before further simulations are performed.

The full, rather than the simplified, turbine should be simulated if sufficient computer capacity is available. This would include behavior neglected by the simplified turbine, like rotation due to torque moment resulting in larger offsets in yaw. Shorter time step and mooring line element lengths could also be simulated to improve the results.

The simulations could be performed with a longer time-scope and a wider variety of environmental inputs. Decay tests in the remaining rigid body motions could be performed to make sure these natural periods were discovered. A fatigue study could be done on the systems to identify critical conditions if more simulations with turbulent wind are preformed. Some combinations of wind speed, significant wave height, and wave period may be more damaging to the systems than others, and identification of these could reduce the risk of failure.

On the park level system, the mooring lines could be designed with similar pre-tension. This would reduce the horizontal motion of the rear wind turbine, but is expected to increase the horizontal motions of the other turbine and the maximum mooring line tension. Additionally, simulations of the power cable could be performed to examine the possibility of reducing its length. If the power cable could be designed similarly as the shared mooring line in this project, rather than laying on the seabed, both its length and cost could be reduced.

The anchor cost should also be studied to estimate how much the total cost is reduced when sharing a mooring line between the turbines. Further investigation of shared mooring line configurations between two or more wind turbines could also be studied to reduce the total cost even more.

References

Bachynski, E., 2019. Tmr4505 - marine structures, specialization course - integrated dynamic analysis of wind turbines - lecture notes.

Bak, C., Zahle, F., Bitsche, R., Kim, T., Yde, A., Henriksen, L.C., Hansen, M.H., Blasques, J.P.A.A., Gaunaa, M., Natarajan, A., 2013. The dtu 10-mw reference wind turbine, in: Danish Wind Power Research 2013.

Chakrabarti, S., 2005. Handbook of Offshore Engineering (2-volume set). Elsevier.

Chan Chow, M.N., 2019. Mooring system design for a floating wind farm in very deep water-European Wind Energy Master Thesis. Master's thesis. NTNU.

Connolly, P., Hall, M., 2019. Comparison of pilot-scale floating offshore wind farms with shared moorings. Ocean Engineering 171, 172–180.

Cruz, J., Atcheson, M., 2016. Floating offshore wind energy: the next generation of wind energy. Springer.

DNVGL, 2019. Dnv gl. URL: `https://www.dnvgl.com/services/marine-operations-and-mooring-analysis-software-sima-2324?gclid=CjwKCAiAluLvBRASEiwAAbX3GbBNhc0QxUYSjmGieH_2dAqoX04wtufx30bNwNnPgEyMy6xBQ_vV7xoCHw4QAvD_BwE`.

DNVGL-OS-E301, 2018. Dnvgl-os-e301 position mooring .

DNVGL-RP-C205, 2017. Dnvgl-rp-c205. Recommended Practice–Environmental Conditions and Environmental Loads .

DNVGL-ST-0119, 2018. Dnvgl-st-0119 floating wind turbine structures .

Equinor, 2020. Equinor web page. URL: `https://www.equinor.com/`.

Europe, W., 2020. Offshore wind in europe: Key trends and statistics 2019. Published February 2020 .

Faltinsen, O.M., 1998. Sea Loads on ships and offshore structures. Cambridge University Press.

Hall, M., Connolly, P., 2018. Coupled dynamics modelling of a floating wind farm with shared mooring lines, in: ASME 2018 37th International Conference on Ocean, Offshore and Arctic Engineering, American Society of Mechanical Engineers Digital Collection.

Hansen, M.O., 2015. Aerodynamics of wind turbines. Routledge.

Inman, D.J., 2008. Engineering vibration (3rd.).

IRENA, 2016. Innovation outlook: Offshore wind. International Renewable Energy Agency, Abu Dhabi .

Jensen, N.O., 1983. A note on wind generator interaction. Risø National Laboratory.

Jonkman, B.J., Buhl Jr, M.L., 2006. TurbSim user's guide. Technical Report. National Renewable Energy Lab.(NREL), Golden, CO (United States).

Landbø, T., 2013. Oo star wind floater: A robust and flexible concept for floating wind. Norway: Dr. techn. Olav Olsen .

Larsen, K., 2020. Tmr4225 marine operations - lecture notes.

Van der Male, P., Lourens, E., 2015. Operational vibration-based response estimation for offshore wind lattice structures, in: Structural Health Monitoring and Damage Detection, Volume 7. Springer, pp. 83–96.

Müller, K., Lemmer, F., Yu, W., 2018. Public definition of the two lifes50+ 10mw floater concepts. Public report D 4.

Musial, W., Beiter, P., Tegen, S., Smith, A., 2016. Potential Offshore Wind Energy Areas in California: An Assessment of Locations, Technology, and Costs. Technical Report. National Renewable Energy Lab.(NREL), Golden, CO (United States).

Naess, A., Moan, T., 2013. Stochastic dynamics of marine structures. Cambridge University Press.

NDBC, 2020. National data buoy center. URL: `https://www.ndbc.noaa.gov/station_history.php?station=46059`.

Olsen, O., 2020. Olav olsen web page. URL: `https://www.olavolsen.no/en/aktuelt/post-SdQPQ-gjennombrudd-for-oo-star-wind-floater`.

Pettersen, B., 2007. Marin teknikk 3-hydrodynamikk. Dept. of Marin Techn. NTNU, Trondheim, Norway .

SINTEF, 2019. Sintef ocean. URL: `https://www.sintef.no/en/software/sima/`.

Vryhof, 2005. Anchor manual. Krimpen ad Yssel, The Netherlands .

Xu, Kun, L.K.S.Y.Z.M.G.Z.M.T., 2020. Design and comparative analysis of alternative mooring systems for floating wind turbines in shallow water with emphasis on ultimate limit state design .

Appendix

A Thrust curve recreated in *Excel* with estimated trend lines

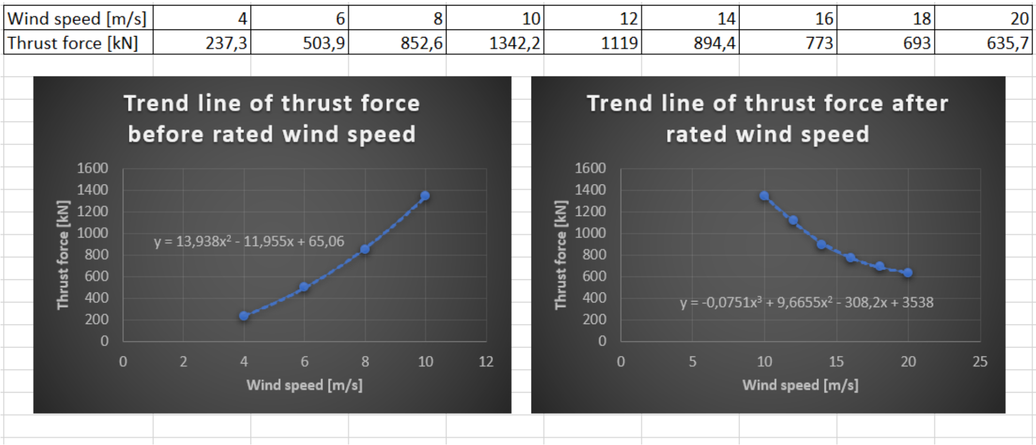

Wind speed [m/s]	4	6	8	10	12	14	16	18	20
Thrust force [kN]	237,3	503,9	852,6	1342,2	1119	894,4	773	693	635,7

Figure 80: Thrust curve recreated in *Excel* with estimated trend lines

B Decay test on single turbine mooring *System 1*

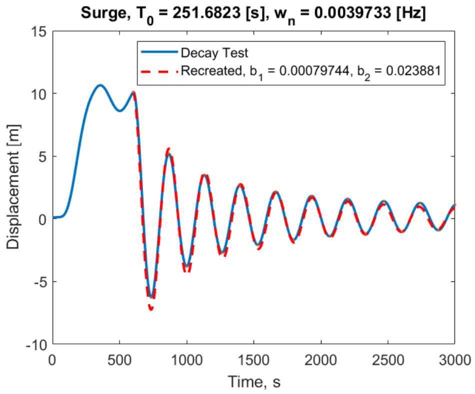

Figure 81: System 1, Surge.

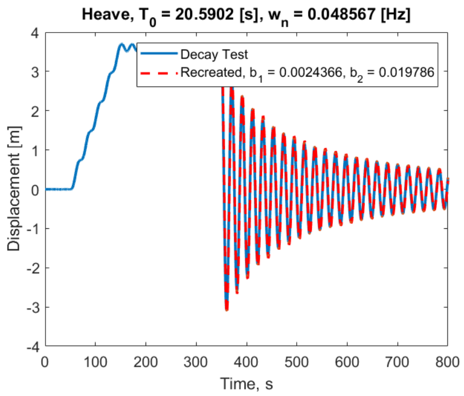

Figure 82: System 1, Heave.

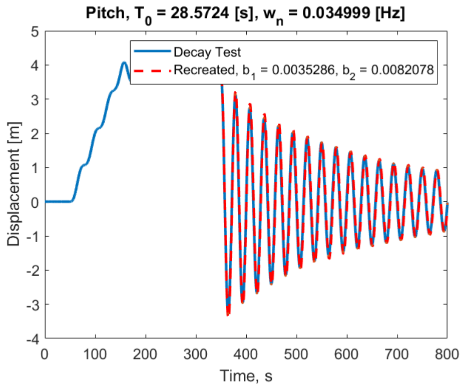

Figure 83: System 1, Pitch.

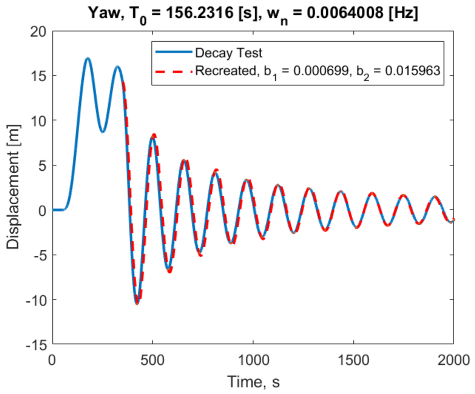

Figure 84: System 1, Yaw.

C Frequency in mooring line 3 from turbulent wind test on *System 1*

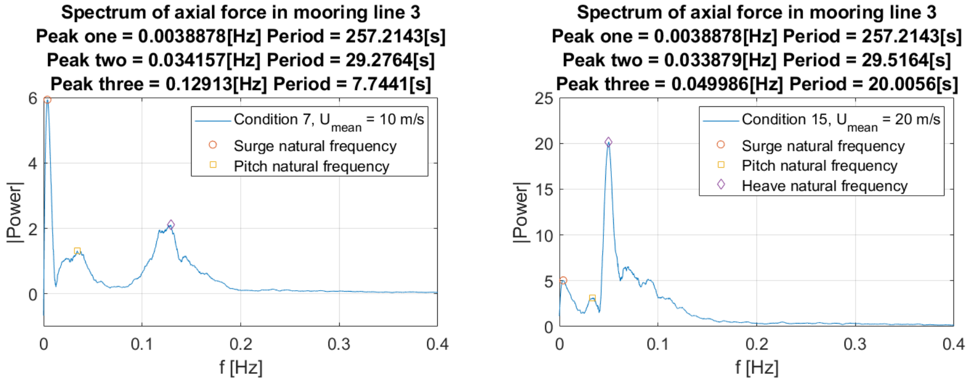

(a) Frequencies in mooring line 3 in condition 7.

(b) Frequencies in mooring line 3 in condition 15.

Figure 85: Frequencies in mooring line 3 in condition 7 (a) and condition 15 (b), from turbulent wind test on *System 1*.

D Decay test on single turbine mooring *System 2*

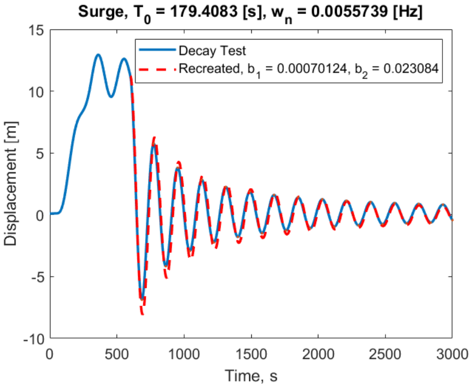

Figure 86: System 2, Surge.

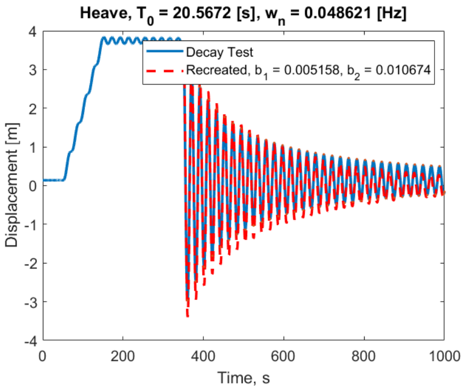

Figure 87: System 2, Heave.

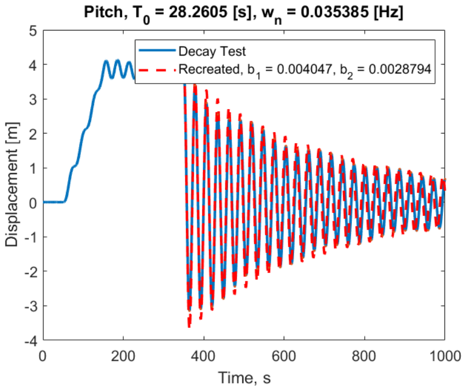

Figure 88: System 2, Pitch.

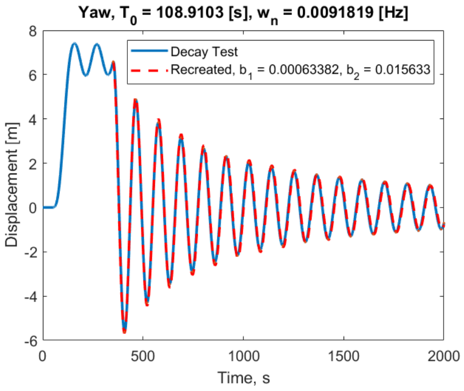

Figure 89: System 2, Yaw.

E Frequency in mooring line 3 from turbulent wind test on *System 2*

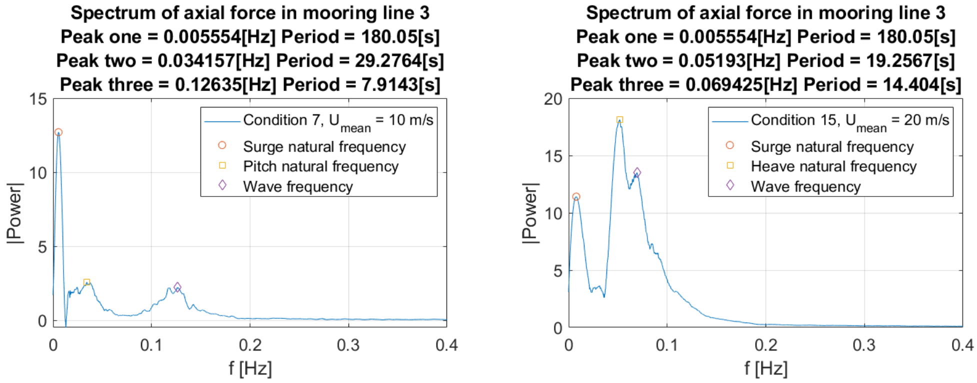

(a) Frequencies in mooring line 3 in condition 7.

(b) Frequencies in mooring line 3 in condition 15.

Figure 90: Frequencies in mooring line 3 in condition 7 (a) and condition 15 (b), from turbulent wind test on *System 2*.

F Decay test on shared mooring system

Heave

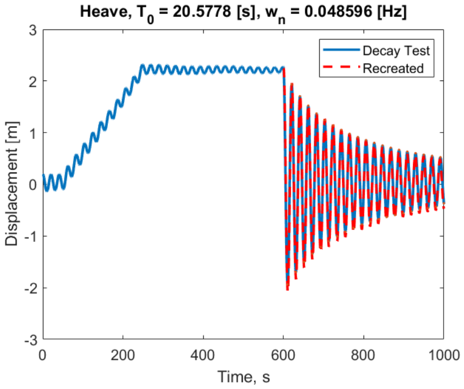

Figure 91: Decay Heave

Pitch

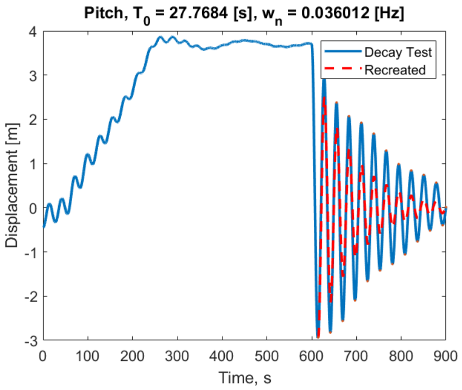

Figure 92: Decay Pitch

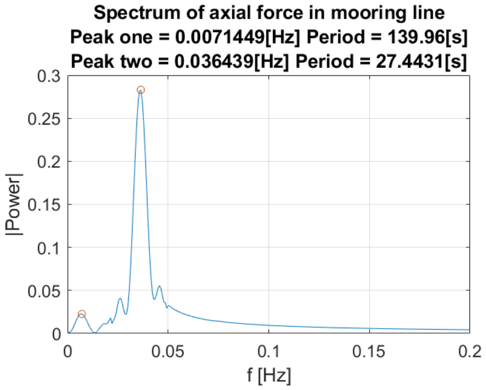

Figure 93: FFT Pitch

Yaw

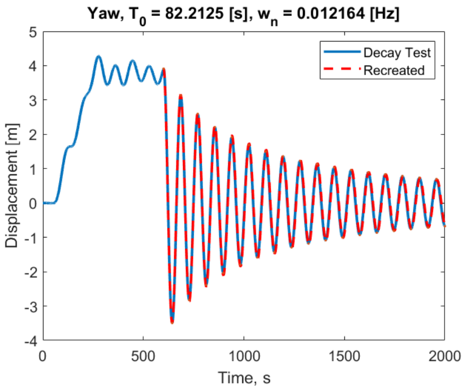

Figure 94: Decay Yaw

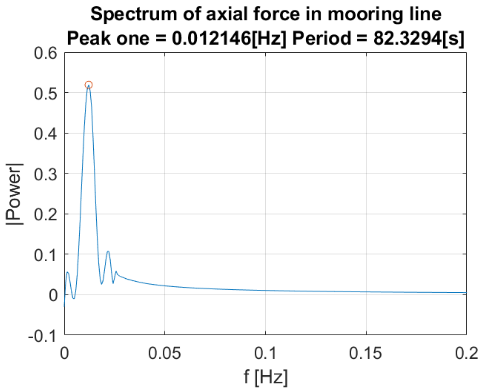

Figure 95: FFT Yaw

Test 2

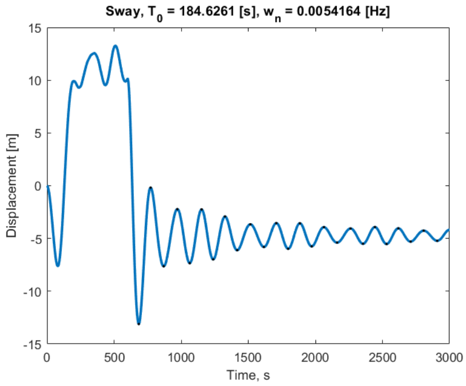

Figure 96: Decay *Test 2*

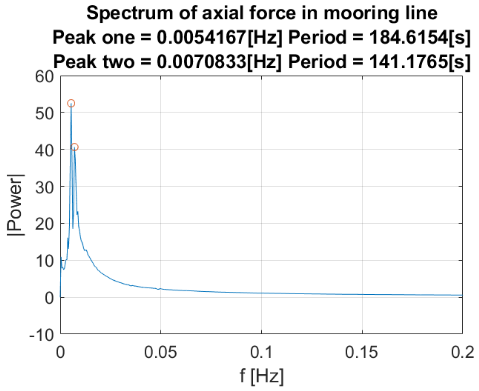

Figure 97: FFT *Test 2*

Test 3

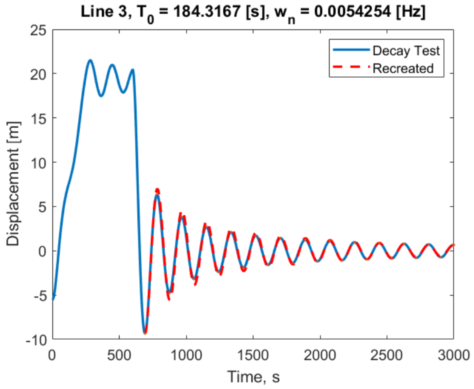

Figure 98: Decay *Test 3*

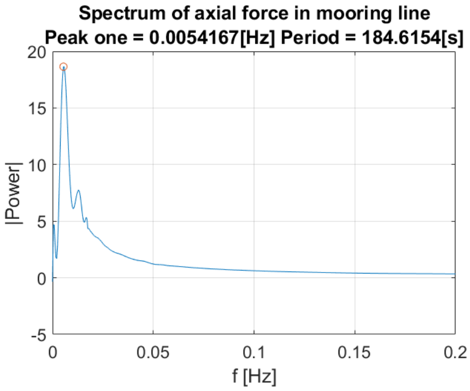

Figure 99: FFT *Test 3*

Test 4

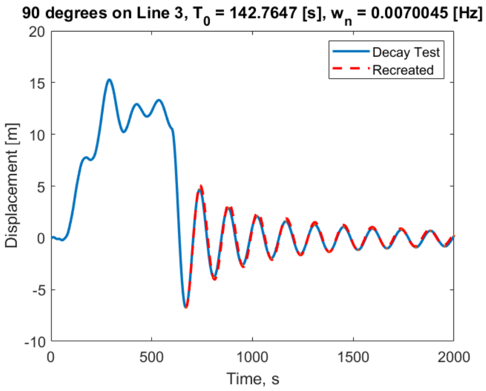

Figure 100: Decay Line 3 90

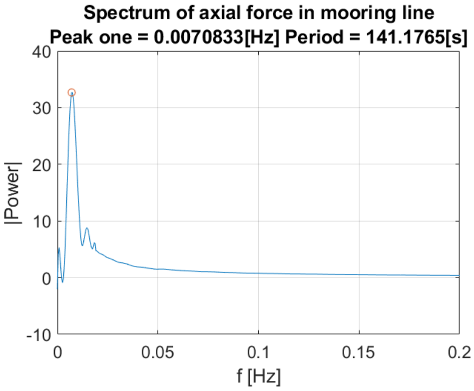

Figure 101: FFT Line 3 90

G Turbulent wind test on shared mooring system

Environmental forces parallel with *Line 1*, frequencies in mooring line 4

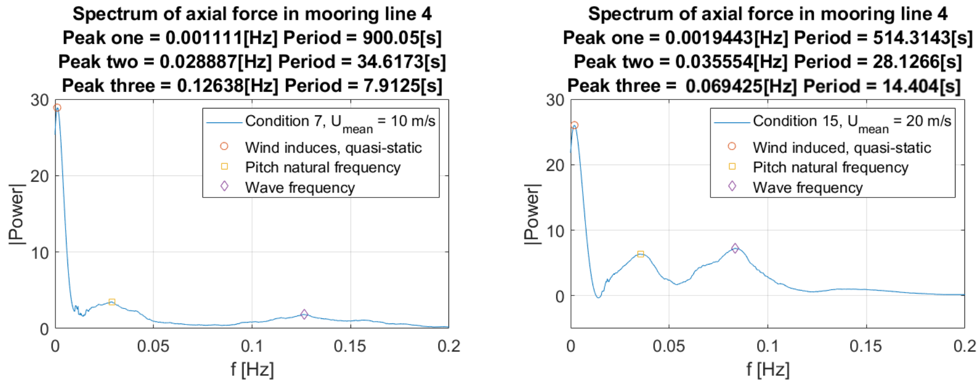

(a) Tension in mooring *Line 4* in condition 7. **(b)** Tension in mooring *Line 4* in condition 15.

Figure 102: Frequencies in mooring line 4 from turbulent wind test parallel to *Line 1* in shared mooring line system.

Environmental forces parallel with *Line 3*, wake deficit considered.

Frequencies in mooring line 2

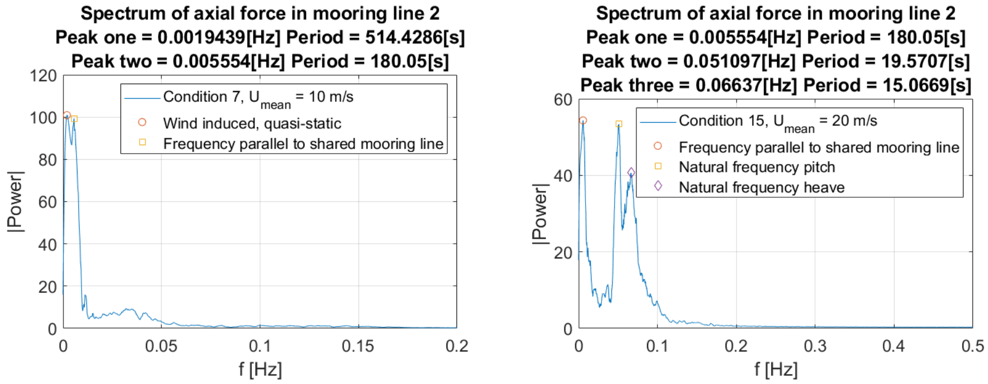

(a) Tension in mooring *Line 2* in condition 7. **(b)** Tension in mooring *Line 2* in condition 15.

Figure 103: Frequencies in mooring line 4 from turbulent wind test parallel to *Line 3* in shared mooring line system.

Frequencies in mooring line 5

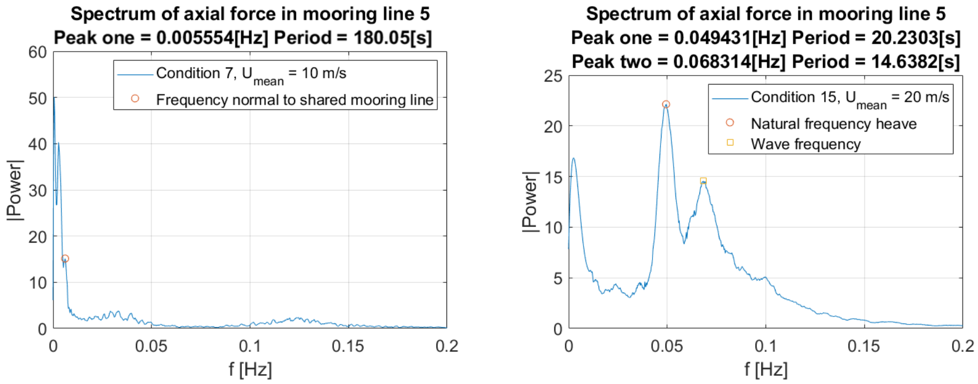

(a) Tension in mooring *Line 5* in condition 7. **(b)** Tension in mooring *Line 5* in condition 15.

Figure 104: Frequencies in mooring line 5 from turbulent wind test parallel to *Line 3* in shared mooring line system.

Jan Ove Kvamen

NTNU
Kunnskap for en bedre verden